Highly Transparent Passivating and Carrier-Selective Contact Schemes for c-Si Solar Cells

Ah Sen, M.T.S.K.

DOI
10.4233/uuid:c385f752-d9bb-4f39-9254-a0fccaf9d5d3

Publication date
2024

Document Version
Final published version

Citation (APA)
Ah Sen, M. T. S. K. (2024). *Highly Transparent Passivating and Carrier-Selective Contact Schemes for c-Si Solar Cells*. [Dissertation (TU Delft), Delft University of Technology]. https://doi.org/10.4233/uuid:c385f752-d9bb-4f39-9254-a0fccaf9d5d3

Important note
To cite this publication, please use the final published version (if applicable).
Please check the document version above.

HIGHLY TRANSPARENT PASSIVATING AND CARRIER-SELECTIVE CONTACT SCHEMES FOR C-SI SOLAR CELLS

HIGHLY TRANSPARENT PASSIVATING AND CARRIER-SELECTIVE CONTACT SCHEMES FOR C-SI SOLAR CELLS

Proefschrift

ter verkrijging van de graad van doctor
aan de Technische Universiteit Delft,
op gezag van de Rector Magnificus Prof. d.r ,
voorzitter van het College voor Promoties,
in het openbaar te verdedigen op
Donderdag 12 September om 15:00 uur

door

Mike Tang Soo Kiong AH SEN

Master of science in Sustainable Energy Techology, Technische Universiteit Delft, Nederland
geboren te Réduit, Mauritius

Dit proefschrift is goedgeheurd door de promtoren.

Samenstelling promotiecommissie bestaat uit:

Rector Magnificus,	voorzitter
Prof. dr. A. W. Weeber,	Technische Universiteit Delft, *promotor*
Prof. dr. M. Zeman	Technische Universiteit Delft, *promotor*
Onafhankelijke leden:	
Prof. dr. M. Morales Masis	Universiteit Twente, Twente
dr. J. Beijersbergen,	Levitech B.V., Almere
em. Prof. dr. W. Sinke,	Universiteit van Amsterdam, Amsterdam
dr. T. J. Savenije,	Technische Universiteit Delft
Prof. dr. I. Gordon,	Technische Universiteit Delft / imec, Belgium
Prof. dr. M. Popov	Technische Universiteit Delft, reservelid

Keywords: passativing contacts, c-Si solar cells, metal oxides, transparent contacts

Printed by: Johannes Gutenberg

Cover by: Beautiful cover art that captures the entire content of this thesis in a single illustration.

ISBN 000-00-0000-000-0

An electronic copy of this dissertation is available at
https://repository.tudelft.nl/.

CONTENTS

SUMMARY

Photovoltaics will play a pivotal role in achieving a low-carbon-emission society. Remarkable advancements in the efficiency of crystalline Si (c-Si) solar cells, combined with standardized processes along the whole value chain, have enabled cost-competitive solar electricity production. In order to further decrease the cost of photovoltaic, significant efforts must be dedicated to further enhancing the efficiency of solar cells.

The implementation passivating and carrier-selective contacts in recent years has led to a remarkable increase in the conversion efficiency of c-Si solar cells. Solar cells, such as silicon heterojunction (SHJ) and poly-Si/SiO_x-based technologies are prime examples of the efficacy of these contacts, as cell efficiencies above 26% have been demonstrated. These achievements can be attributed to the excellent surface passivation properties of the intrinsic amorphous hydrogenated silicon (a-Si:H(i)) and the ultra-thin SiO_x interlayers, coupled with the high carrier-selectivity exhibited by the doped Si-based layers. However, a significant limitation associated with these passivating and carrier-selective contacts is related to their optical parasitic absorption losses within the layers. These losses stem from the free-carrier absorption in a-Si:H layers of SHJ solar cells and poly-Si layers, which possess relatively narrow bandgaps, making them prone to absorbing the ultraviolet (UV) portion of sunlight. Consequently, these parasitic absorption losses diminish the amount of light reaching the c-Si absorber, ultimately restricting the short-circuit current (J_{sc}) output of the solar cell.

To mitigate these losses, wide-bandgap metal oxide layers, such as MoO_x and TiO_x, have been proposed as promising alternatives to replace these highly doped Si-based contacts. These metal oxides possess distinct carrier-selective characteristics, primarily due to their differences in work function (WF) with respect to the c-Si, leading to induced band bending within the absorber. Despite significant progress in recent years, several challenges still exist, as metal oxide contacts often suffer from carrier-selectivity issues due to material instability and interface reactions with adjacent layers.

This thesis explores several possible strategies to minimize the parasitic absorption losses in passivating and carrier-selective contacts. A considerable portion of the research is devoted to understanding and enhancing the contact properties of the MoO_x layer. The focus on MoO_x is driven by the challenges it faces with carrier-selectivity, stemming from its low thermal stability and its susceptibility to band alignment issues when combined with various passivating interlayers. An innovative MoO_x contact is introduced, incorporating ultra-thin surface passivating interlayers based on Al_2O_3 films. These ultra-thin interlayers offer substantial advantages, including enhanced surface passivation, minimal parasitic absorption,

and improved transport of majority carriers. Additionally, MoO_x and TiO_x contacts, deposited by pulsed laser deposition (PLD) are also explored for c-Si solar cells. PLD offers several advantages over conventional deposition techniques, including excellent layer tunability and gentle deposition properties suitable for sensitive functional layers. This thesis also investigates the merits of PLD's soft deposition properties by depositing transparent conductive oxide (TCO) layers on ultra-thin poly-Si (<20 nm) contacts. In the case of thin poly-Si layers, it becomes necessary to incorporate a TCO layer to ensure adequate lateral conductivity for majority carriers to reach the metal grid electrode. One approach to improve the transparency of poly-Si contacts is to reduce the layer thickness. However, the subsequent deposition of a TCO layer on ultra-thin poly-Si (<20 nm) often worsen the surface passivation of the contact since the high energetic species formed during sputtering are able to create dangling bonds at the Si surface. In contrast, PLD's gentle deposition properties result in reduced surface passivation degradation, even for 10 nm thick layers. The key findings of these investigations are concisely summarized below:

Firstly, the benefits of utilizing an ultra-thin Al_2O_3/SiO_y interlayer to improve the surface passivation and the hole carrier-selectivity of the MoO_x contact are shown. Commonly, hole-selective MoO_x contacts have been combined with an a-Si:H(i) interlayer due to its excellent surface passivation. However, MoO_x/a-Si:H(i) contacts often result in observable hole selectivity issues, thereby resulting in an S-shaped current-voltage (IV) curve - especially after a thermal treatment. Alternatively, an ultra-thin as-deposited Al_2O_3/SiO_y interlayer, deposited by spatial atomic layer deposition (sALD), improves the surface passivation of the MoO_x contact while exhibiting good carrier selectivity properties. The $MoO_x/Al_2O_3/SiO_y$ contact, fabricated on a 6-inch commercial Si substrate with a screen-printed Ag grid, shows good thermal stability, thereby resulting in a cell efficiency of 18.2 % and open circuit voltage (V_{oc}) of 650 mV, after an annealing treatment at 210 °C. Furthermore, the solar cell shows an improved short-circuit current density (J_{sc}) by replacing a-Si:H(i) by the Al_2O_3/SiO_y interlayer. However, the remaining bottleneck of this contact can be ascribed to the limited surface passivation provided by the interlayer. Although a post-deposition anneal (PDA) treatment on the Al_2O_3/SiO_y interlayer can improve the surface passivation, it also results in a higher carrier selectivity loss. This is ascribed to the formation of Si-O bonds which in turns thickens the SiO_y interlayer and results in more stoichiometric layers.

Secondly, the influence of different passivating interlayers, notably a-Si:H(i), thermally grown ultra-thin SiO_2, and Al_2O_3/SiO_y on the carrier-selectivity properties of MoO_x contacts are analyzed and compared. Significant differences in carrier-selectivity and thermal behavior can be noted for the different contacts. By using computer simulation (ATLAS) these differences are explained. Carrier selectivity and thermal behavior are determined by the interaction between the WF of the contact, surface passivation, and the majority carrier transport across the interlayer – which is represented by hole mobility. In order to achieve good hole carrier selectivity, we highlight the importance of a sufficiently high induced band bending provided by the high WF of the contact, and the requirement for sufficient hole mobility through the interlayer. Although high surface passivation can be obtained with a

MoO_x/a-Si:H(i) contact, the a-Si:H(i) interlayer reduces the induced band bending inside the Si substrate resulting in a less effective hole transport. The Al_2O_3/SiO_y interlayer shows good transport for majority carriers but requires further surface passivation improvement.

To improve surface passivation of an ultra-thin oxide interlayer, a hydrogenation process is required. Different hydrogenation strategies to improve the passivating quality of the MoO_x contact are explored. Conventional hydrogenation methods typically used for poly-Si contacts are not suitable because of the interaction of the oxygen, contained in the MoO_x layer, with the diffused hydrogen and the lack of thermal stability of the MoO_x at temperatures required for effective hydrogenation. Alternatively, we explored the application of an ultra-thin hydrogenated SiO_y interlayer (SiO_y:H) which is naturally formed at the Si surface after Al_2O_3 deposition. A PDA treatment was performed after Al_2O_3 deposition to improve the surface passivation. Subsequently, the Al_2O_3 layer was selectively etched off in a 1% diluted TMAH (tetramethyl-ammonium-hydroxide) solution for 1 min at 60 °C without severely damaging the chemical surface passivation properties provided by the remaining SiO_y:H interlayer. After subsequent MoO_x deposition, high surface passivation up to 710 mV was obtained on symmetric textured n-type Cz Si samples. At the time of writing, this is the highest iV_{oc} value achieved with a MoO_x contact on an ultra-thin oxide interlayer. Nevertheless, the MoO_x/SiO_y:H contact resistivity is too high (~1000 mOhm.cm^2) and requires further charge carrier transport optimization.

Ultra-thin poly-Si contacts require TCO layers to allow for lateral transport of majority carriers to the metal electrodes. Conventionally, TCO layers are sputtered which induce significant damage on the ultra-thin poly-Si contacts. Although the surface passivation damage can be partially repaired after annealing at elevated temperatures (~350 °C), this also results in an increase contact resistance because of the formation of a parasitic oxide at the ITO/poly-Si interface. In addition, the induced sputtering damage is even more prominent for a thinner poly-Si layer which is essential to mitigate the parasitic absorption losses. ITO layers deposited by PLD show reduced surface passivation damage on poly-Si contacts, compared to sputtering, and this damage does not dependent on the thickness of the poly-Si layer which allows for the utilization of thinner poly-Si contacts. Further damage reduction can be obtained by increasing the ITO deposition pressure while a low contact resistivity (~45 mOhm.cm^2) and good thermal stability up to 350 °C were achieved. In addition, excellent ITO opto-electrical properties with a layer resistivity of 4.9 x 10^{-4} Ohm.cm and a mobility of 42.1 cm^2/Vs were acquired even at higher repetition rate and laser fluence which is needed to obtain higher deposition rate.

Lastly, the application of MoO_x and TiO_x contacts deposited by PLD and intergrated in a completed c-Si solar cells is explored. PLD displays several advantages due to its wide range of deposition parameters and its soft deposition properties which could be beneficial for underlying sensitive layers. The carrier selectivity of MoO_x contact can be improved by increasing the deposition pressure which is the result of a more stoichiometry layer. Nevertheless, a selective loss (defined as ΔV_{oc}=$iV_{oc} - V_{oc}$) of about 50 mV exists thereby resulting in an S-shaped IV curve. One possible reason for the observed selectivity loss can be attributed to the formation of a parasitic

oxide at the MoO_x/a-Si:H(i) interface. However, further parameters variation suggest that the origin of the selectivity loss is caused by a lack in layer WF. On the other hand, the TiO_x contact shows good iV_{oc} of about 700 and 730 mV on SiO_y:H and a-Si:H(i) interlayers, respectively. By utilizing the PLD hole MoO_x and electron TiO_x contacts in a solar cell, an iV_{oc} of 742 mV is obtained showing the soft deposition properties of PLD. Further contact optimization is required to reduce the series resistance present on the a-Si:H(i) interlayer and to optimize the final efficiency of the solar cells.

In conclusion, this thesis demonstrates that outstanding carrier selectivity properties can be attained using MoO_x contact paired with an ultra-thin Al_2O_3 interlayer. To enhance the surface passivation of the oxide interlayer, dedicated hydrogenation strategies are necessary due to the thermal instability of the MoO_x layer. The research illustrates that by selectively etching the Al_2O_3, a highly passivated oxide interlayer, formed after a PDA treatment, can be obtained and employed in MoO_x contacts. Additionally, the development and implementation of ultra-thin poly-Si contacts (<20 nm) to reduce parasitic absorption losses can be accomplished by depositing PLD TCO layers. This is because PLD exhibits a soft deposition property that mitigates the deposition-induced damage to the surface passivation of poly-Si contacts.

SAMENVATTING

In dit proefschrift zijn verschillende aspecten van passivatie en ladingsdragerselectieve contacteigenschappen voor c-Si-zonnecellen onderzocht en ontwikkeld. De belangrijkste conclusies zijn als volgt samen te vatten:

Ten eerste zijn de voordelen aangetoond van het gebruik van een ultradunne Al_2O_3/SiO_y-tussenlaag om de oppervlaktepassivatie van het MoO_x-contact te verbeteren. Gewoonlijk worden gat-selectieve MoO_x-contacten gecombineerd met een intrinsiek gehydrogeneerde amorfe Si (a-Si:H(i)) tussenlaag vanwege de uitstekende oppervlaktepassivatie. MoO_x/a-Si:H(i)-contacten resulteren echter vaak in waarneembare gatenselectiviteitsproblemen, wat resulteert in een S-vormige stroom-spanning (IV)-kromme - vooral na een post-depositie warmtebehandeling. Als alternatief verbetert een ultradunne gedeponeerde Al_2O_3/SiO_y-tussenlaag, gedeponeerd door ruimtelijke atoomlaagdepositie (sALD), de oppervlaktepassivatie van het MoO_x-contact terwijl het goede ladingsdragerselectiviteitseigenschappen vertoont. Het $MoO_x/Al_2O_3/SiO_y$-contact vertoont een goede thermische stabiliteit, wat resulteert in een celrendement van 18,2 % en een openklemspanning (V_{oc}) van 650 mV, na verwarmen bij 210 °C. Bovendien vertoont de zonnecel een verbeterde kortsluitstroomdichtheid (J_{sc}) door a-Si:H(i) te vervangen door de Al_2O_3/SiO_y-tussenlaag. Het resterende knelpunt van dit contact kan echter worden toegeschreven aan de beperkte oppervlaktepassivatie door de tussenlaag. Hoewel een post-depositie warmtebehandeling op de Al_2O_3/SiO_y-tussenlaag de passivatie van het oppervlak kan verbeteren, resulteert dit ook in een toename van het verlies aan ladingsdragerselectiviteit. Dit wordt toegeschreven aan de vorming van Si-O-bindingen die op hun beurt de SiO_y-tussenlaag dikker maken en de stoichiometrie van de laag verhogen.

In het volgende hoofdstuk wordt de invloed geanalyseerd en vergeleken van verschillende passiverende tussenlagen, met name a-Si:H(i), thermisch gegroeid ultradun SiO_2 en Al_2O_3/SiO_y op de ladingsdragerselectiviteitseigenschappen van MoO_x-contacten. Er kunnen significante verschillen in ladingsdragerselectiviteit en thermisch gedrag worden opgemerkt voor de verschillende tussenlagen. Door gebruik te maken van computersimulaties (ATLAS) kunnen deze verschillen verklaard worden. Ladingsdragerselectiviteit en thermisch gedrag worden bepaald door de interactie tussen de werkfunctie (WF) van het contact, oppervlaktepassivatie en het transport van de meerderheids ladingsdragers over de tussenlaag - wat wordt gedefinieerd als gatenmobiliteit. Om een goede gatenselectiviteit te bereiken, benadrukken we het belang van een voldoende hoge geïnduceerde bandbuiging door de hoge WF van het contact en de vereiste van een voldoende gatenmobiliteit in de tussenlaag. Hoewel hoge oppervlaktepassivatie kan worden verkregen met een MoO_x/a-Si:H(i) contact, vermindert de a-Si:H(i) tussenlaag de geïnduceerde bandbuiging in het Si-substraat,

terwijl een geschikte banduitlijning vereist is voor effectief gatentransport. De Al_2O_3/SiO_y-tussenlaag laat een goed meerderheidsladingsdragertransport zien, maar vereist verdere verbetering van de passivatie van het oppervlak. In hoofdstuk 5 verkennen we verschillende hydrogeneringsstrategieën om de passivatiekwaliteit van het MoO_x-contact te verbeteren. Conventionele hydrogeneringsmethoden die doorgaans worden gebruikt voor poly-Si-contacten zijn niet geschikt vanwege de interactie van de zuurstof in de MoO_x-laag met de gediffundeerde waterstof en het gebrek aan thermische stabiliteit die nodig is voor effectieve hydrogenering. Als alternatief onderzoeken we de toepassing van een ultradunne gehydrogeneerde SiO_y-tussenlaag (SiO_y:H) die wordt gevormd aan het Si-oppervlak, na Al_2O_3 depositie en een daaropvolgende post-depositie warmtebehandeling. Dit kan worden bereikt door selectief de Al_2O_3-laag te etsen in een 1% verdunde TMAH-oplossing (tetramethyl-ammonium-hydroxide oplossing) gedurende 1 minuut bij 60 °C zonder de chemische passivatie-eigenschappen van de resterende SiO_y:H-tussenlaag ernstig te beschadigen. Na daaropvolgende MoO_x-depositie werd hoge oppervlaktepassivatie tot impliciete-openklemspanning iV_{oc} waarden van 710 mV verkregen op symmetrische getextureerde n-type Cz Si-monsters. Op basis van de huidige kennis van de auteur is dit de hoogste iV_{oc}-waarde die is bereikt met een MoO_x-contact op een ultradunne oxide-tussenlaag. Desalniettemin is de MoO_x/SiO_y:H-contactweerstand te hoog (~1000 mOhm.cm^2) en vereist verdere laagoptimalisatie.

Hoofdstuk 6 is gericht op de toepassing van gepulste laserdepositie (PLD) om transparante geleidende oxide (TCO, transparent conductive oxide) lagen af te zetten op ultradunne poly-Si contacten (<20 nm). Gesputterde indiumtinoxide (ITO) lagen veroorzaken daarentegen aanzienlijke schade aan de ultradunne poly-Si-contacten die gedeeltelijk kunnen worden gerepareerd na verwarming bij verhoogde temperatuur (~350 °C). Dit verhoogt echter op zijn beurt de contactweerstand vanwege de vorming van een parasitair oxide op het ITO/poly-Si-grensvlak. Bovendien is de geïnduceerde sputterschade zelfs nog prominenter voor een dunnere poly-Si-laag, wat essentieel is om de parasitaire absorptieverliezen daarin te verminderen. ITO-lagen die door PLD zijn gedeponeerd, vertonen daarentegen verminderde oppervlaktepassivatieschade op poly-Si-contacten en zijn niet afhankelijk van de dikte (tussen 10 en 20 nm), wat het gebruik van dunnere poly-Si-contacten mogelijk maakt. Verdere schadevermindering kan worden verkregen door dedruk bij de ITO-depositie te verhogen terwijl een lage contactweerstand (~45 mOhm.cm^2) en thermische stabiliteit (tot 350 °C) werden bereikt. Bovendien werden uitstekende ITO opto-elektrische eigenschappen verkregen met laagweerstand van 4,9 x 10^{-4} Ohm.cm en mobiliteit van 42,1 cm^2/Vs, zelfs bij een hogere herhalingssnelheid en laserfluentie die nodig is om een hogere depositiesnelheid te verkrijgen.

In hoofdstuk 7 worden gaten MoO_x- en elektron TiO_x-contacten, gedeponeerd door PLD en aangebracht op c-Si-zonnecellen, onderzocht. PLD vertoont verschillende voordelen vanwege het brede scala aan depositieparameters en de zachte depositie-eigenschappen die gunstig kunnen zijn voor onderliggende gevoelige lagen. De ladingsdragerselectiviteit van MoO_x-contact kan worden verbeterd door de depositiedruk te verhogen, wat resulteert in een meer stoichiometrische laag.

Desalniettemin bestaat er een verschil in iV_{oc} en V_{oc} (ΔV_{oc}) van ongeveer 50 mV, wat resulteert in een S-vormige IV-kromme. Hoewel dit selectiviteitsverlies zou kunnen worden toegeschreven aan de vorming van een parasitair oxide op het MoO_x/a-Si:H(i)-grensvlak – vanwege de toenemende O_2-depositiedruk, suggereren verdere parametervariaties dat de oorsprong van het selectiviteitsverlies wordt veroorzaakt door een gebrek aan een lage WF. Aan de andere kant vertoont het TiO_x-contact een goede oppervlaktepassivatie met iV_{oc} waarden van respectievelijk ongeveer 700 en 730 mV op SiO_y:H- en a-Si:H(i)-tussenlagen. Verdere contactoptimalisatie is vereist om de serieweerstand op een a-Si:H(i)-tussenlaag te verminderen.

NOMENCLATURE

Abbreviation

PV	photovoltaic
c-Si	crystalline silicon
TCO	transparent conductive oxide
ITO	indium tin oxide
PDA	Post-deposition anneal
PECVD	plasma enhanced chemical vapor deposition
PVD	plasma vapor deposition
LPCVD	low pressure chemical vapor deposition
PLD	pulsed laser deposition
sALD	spatial atomic layer deposition
SRH	shockley-read-Hall
LCoE	leverized cost of energy
ARC	anti-reflection coating
Al-BSF	aluminum back surface field
PERC	passivated emitter and rear cell
SHJ	silicon heterojunction
IBC	interdigitated back contact
TOPCon	tunnel oxide passivated contact
UV	ultra-violet
NIR	near infra-red
TMAH	tetramethylammonium hydroxide
Cz	Czochralski

RCA	Radio corporation of America
NAOS	Nitride acid oxidation of Si
ETL	Electron transport layer
HTL	Hole transport layer
SE	Spectroscopic ellipsometry
STC	Standard test conditions
SR	Spectral response
IQE	Internal quantum efficiency
EQE	External quantum efficiency
TMO	Transition metal oxide
SPV	Surface photovoltage
UPS	Ultra-Violet Photoelectron Spectroscopy
VBO	Valence band offset

Symbols

IV	current-voltage
J_{sc}	short-circuit current density, mA/cm^2
FF	fill factor, %
η	efficiency, %
V_{oc}	open-circuit voltage, V
iV_{oc}	implied open-circuit voltage, V
R_{sheet}	sheet resistance, $\Omega/\square$
WF	work function, eV
ρ	resistivity, Ωcm
μ	mobility, cm^{2}V^{-1}s^{-1}
μ_h	hole mobility, cm^{2}V^{-1}s^{-1}
μ_e	electron mobility, cm^{2}V^{-1}s^{-1}
S_{eff}	effective surface recombination velocity, cm/s
μ_h	hole mobility, cm^{2}V^{-1}s^{-1}

T	temperature, °C
T_{PDA}	post-anneal deposition temperature, °C
T_{PDA}	post-anneal deposition temperature, °C
T_{dep}	deposition temperature, °C
τ_{eff}	effective lifetime, μs
R_{total}	total contact resistivity, mωcm^2
R_{contact}	contact resistivity, mωcm^2
N_{e}	carrier concentration, cm^{-3}
n	refractive index
k	absorption coefficient
d	thickness, nm
P_{chamber}	chamber pressure, mbar

1

INTRODUCTION

1

1.1. CURRENT STATUS OF PHOTOVOLTAICS

THE photovoltaic (PV) industry has shown an impressive growth rate over the past 50 years, leading to a reduction in the cost of PV panels by more than two orders of magnitude [1]. The main reasons behind this drastic reduction in production cost can be associated with remarkable technology improvements, increase in economies of scale, and manufacturing chain standardization [2]. At the end of 2022, 240 GW of PV systems were installed and commissioned worldwide, bringing the world's cumulative PV capacity to a total of 1.19 TW [3], as shown in Figure 1.1. This shows the remarkable resilience of the PV market, despite the turmoil caused by the COVID-19 pandemic. During the writing of this thesis, the levelized cost of energy (LCoE) of utility scale PV (0.029 – 0.042 USD/kWh, depending on the location/climate) is lower than conventional gas combined cycle (0.044 – 0.073 USD/kWh) for unsubsidized energy plants [4]. So far, a lowest energy cost of 0.0104 USD/kWh was announced in form of bids [5]. Although the PV sector has made significant progress in the recent decades, various studies indicate that several terawatts of annual PV production capacity will be required in order to achieve our climate goals [6–8].

This chapter offers a comprehensive overview on various reasons for this impressive PV price reduction and discuss the future developments required as we strive towards reducing our CO_2 emissions.

1.2. HISTORY OF SI PHOTOVOLTAIC

Like any other manufacturing industry, the cost of PV panels production follows a learning curve model which can be used to predict a decrease in future cost with

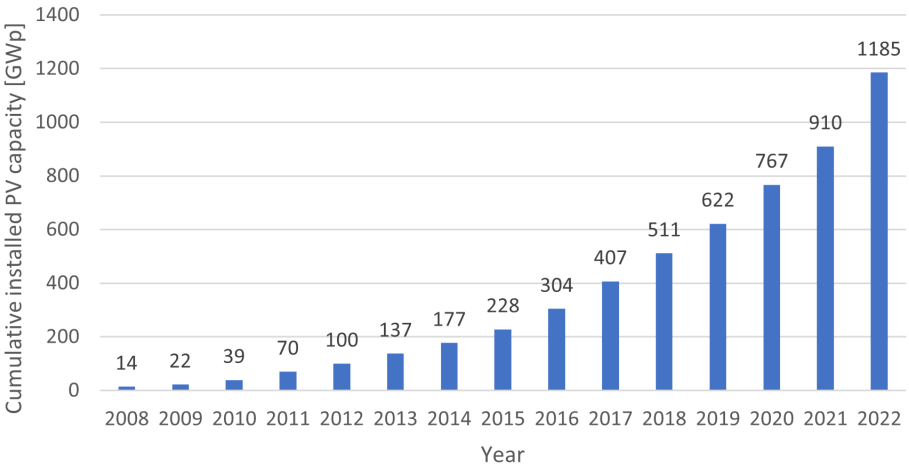

Figure 1.1.: Cumulative installed PV capacity between 2008 to 2022 worldwide. Data retrieved from IEA [3].

increase in cumulative production. The equation is described as follows:

$$C_t = C_0\left(\frac{q_t}{q_0}\right)^{-b} \tag{1.1}$$

where C_t and C_0 (USD/W_p) are manufacturing cost, and q_t and q_0 (units produced) represent the time dependent cumulative production at reference time 0 and t, respectively. The learning coefficient is defined by parameter b which represent the slope of a straight line when the production cost is plotted against cumulative production, in a log-log scale. However, a commonly used indicator is the learning rate ($(LR) = 1 - 2^{-b}$); it defines the reduction in cost for every doubling in cumulative production. The crystalline silicon (c-Si) PV industry has shown a LR of about 22% since 1970. However, over the last decade, the LR of PV panels has accelerated to about 25 - 40% [7].

The rapid reduction in the price of c-Si PV can be attributed to several factors. Firstly, there has been a significant increase in the throughput of production tools and standardization along the entire supply chain [9], reduction in material costs, an increase in Si wafer size and quality, a decrease in Si wafer cost and thickness, and reduced silver consumption [10]. Moreover, the surging increase in solar cell efficiency over the last few decades - while applying low-cost processing technologies - has played a predominant role in achieving a competitive LCoE price, as it directly impacts the LCoE of every other component of the PV system. In 2021, the percentage of the total cost attributed to modules, in comparison to the balance of system components, for PV rooftop systems in Germany amounted to 39% [11]. In contrast, this percentage was 74% in 2008. The combined effect of these factors has led to the impressive decrease in the price and cost of c-Si PV, thus making it a more economically viable option for renewable energy generation. In order to maintain the continuous reduction in price of PV, improving solar cell (and module) efficiency is paramount. The following sections offer a concise understanding on the working principles of a solar cell and a review on the evolution of several c-Si technologies and future trends.

1.3. BASIC OPERATION OF A SOLAR CELL

The basic operation of a solar cell consists of separating and extracting the photogenerated electrons and holes within the semiconductor absorber to their respective terminals. This process entails asymmetric flows of charge carriers towards their respective contacts; strong electron and weak hole current towards the electron electrode and vice versa towards the hole electrode. The ability to create an asymmetric flow of currents at each contact is crucial to be able to extract the internal electrochemical potential energy, and thereby achieving contact selectivity; in the case where high charge carrier selectivity is achieved, the internal electrochemical potential (implied open-circuit voltage, iV_{oc}) will match the external potential (external open-circuit voltage, V_{oc}). Additionally, the iV_{oc} of a solar cell is mainly dependent (assuming a high-quality Si absorber is used) on the surface passivation properties.

1

Excess holes and electrons are generated in the Si absorber by absorption of light with energy larger than the Si bandgap, and rapidly thermalize to the temperature of the Si lattice. This process induces the splitting of the quasi-Fermi levels by which the distribution of holes and electrons can be described by their own quasi-Fermi energies, E_{Fp} and E_{Fn}, respectively, and the difference between E_{Fn} and E_{Fp} is related to the iV_{oc} of the cell. However, photogenerated charge carriers tend to recombine to restore thermodynamic equilibrium. Recombination mechanisms i.e. radiative, Auger, and Shockley-read-Hall (SRH) recombinations exist in the Si bulk which prevent the extraction of the charge carriers to the terminals. Radiative recombination is negligible in Si bulk since it is an indirect band-gap semiconductor. On the other hand, Auger recombination is prevalent especially at high carrier concentration (>1 x 10^{16} cm^{-3}). To a certain extend radiative and Auger recombination are intrinsically unavoidable. SRH recombination occurs due to extrinsic lattice defects, which are found in the silicon bulk as well as at the terminating surface of the silicon lattice. This issue can be alleviated through defect passivation, particularly focusing on addressing the defects located at the silicon surface.

To mitigate the SRH recombination at the Si surface, passivation layers are often deposited on the Si surface, allowing for higher cell iV_{oc}. Dielectric layers, such as silicon nitride (SiN_x), silicon oxide (SiO_x), aluminum oxide (Al_2O_3) are typically used to passivate the Si surface. Atoms in these dielectric layers bind with the Si dangling bonds and consequently reduce the defect density present at the surface. This process is known as chemical passivation. Additionally, hydrogen, often present in the passivating films, is allowed to diffuse to the interface to further passivate the remaining dangling bonds. Another strategy to reduce surface recombination is commonly known as field-effect passivation. Field-effect passivation involves the suppression of one type of carrier near the interface, resulting in a reduction of electron-hole recombination. This can be achieved by depositing dielectric layers on the Si surface which repel one type of charge carrier, depending on the layer's fixed charge density (Q_f). Figure 1.2 shows an overview of the density of interface traps

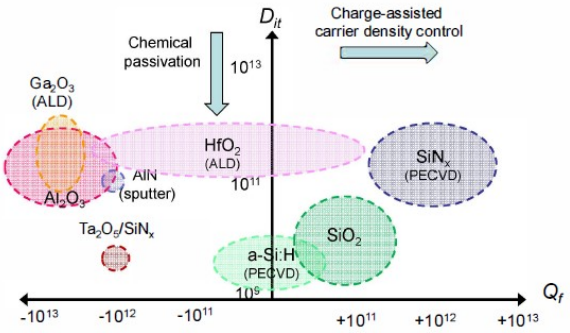

Figure 1.2.: Overview of passivating layers properties on Si in terms of Q_f and D_{it}. Figure was taken from [12].

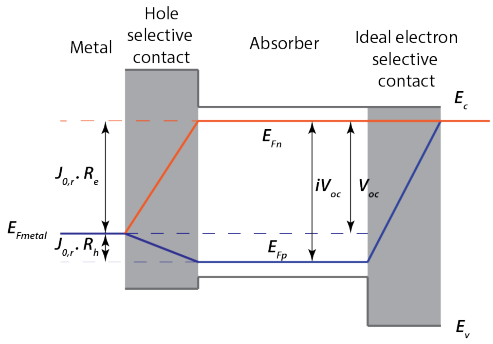

Figure 1.3.: Band diagram showing the quasi-Fermi levels for an ideal electron contact and a non-ideal hole contact. Note that the band bending near the Si surface is not depicted.

(D_{it}) and the Q_f of different surface passivating layers.

Carrier selectivity, on the other hand, is based on a large difference in resistance over the contact for holes and electrons, respectively [13]. The resistance of holes and electrons is governed by concentrations of the charge carriers and their mobilities ($\mu_{e,h}$). The schematic in Figure 1.3 shows the main concepts of carrier selectivity of a solar cell. At the metal contact these quasi-Fermi levels come together. The difference between E_{Fn}, and E_{Fp}, respectively, and metal Fermi level E_{Fmetal} drives an electron resp. hole current towards the contact. At open circuit condition, these currents are equal and the respective differences of the quasi-Fermi level to E_{Fmetal} can be written in terms of this recombination current ($J_{0,r}$) and the effective hole and electron resistances (R_h and R_e), respectively. An optimal hole contact requires a large iV_{oc} and E_{Fp}=$E_{F,metal}$ i.e. R_e»R_h. Several strategies exist to create an asymmetric flow of current to the terminal. For homojunctions, high concentrations of dopants are introduced near the surfaces of the Si absorber which create asymmetric conductivities between the majority and minority carriers. Conversely, passivating and selective contacts, such as SHJ and doped poly-Si contacts utilize a stack of passivating and carrier-selective layers; the doped-Si contact alters the conductivity of charge carrier near the Si surface due to the difference in work function (WF) between the doped selective contact and the Si absorber. As a result, high concentration of majority carrier is maintained near the interface and hence allows for a selective contact. The following section will elaborate on the cell operation, manufacturing, and limitations of several cell architectures.

1.4. C-SI SOLAR CELLS TECHNOLOGIES

1.4.1. AL-BSF & PERC SOLAR CELLS

The manufacturing of solar cells at higher volumes commenced with the production of aluminum back surface field (Al-BSF) solar cells. An Al-BSF solar cell consists of an alloyed rear Al contact and a phosphorus (n+) diffusion region at the front side.

Initially developed in the late 70s, the Al-BSF solar cell typically uses a p-type c-Si absorber mainly because of historical and technological reasons [14].

The process flow of this architecture can be described by four main fabrication steps: saw damage removal combined with wafer texturing, front phosphorus diffusion, front hydrogenated amorphous silicon nitride (a-SiN_x:H) deposition, and screen-printing and firing of metal electrodes. The electron-selective contact is formed by adding high concentration of phosphorus near the front Si surface which creates an asymmetric conductivities between the majority and minority carriers. This process also serves as lateral conduction for electrons transport to the metal grid. While increasing the doping concentration might seem favorable to improve contact selectivity, this also causes bandgap narrowing, and Auger and SRH recombination [15, 16]. SiN_x, typically deposited by plasma enhanced chemical vapor deposition (PECVD), is both used to passivate the front Si surface and the bulk of multi-crystalline Si bulk, while also acting as an anti-reflection coating (ARC). At the rear side, Al is alloyed by firing at temperature between 700 – 900 °C which creates p^+- Al-BSF thereby enabling hole collection and certain level of surface passivation. Additionally, the firing step is crucial to form good contact between the front screen-printed Ag grid and Si absorber.

The main limitation of the Al-BSF structure is the high recombination losses at the rear side of the cell. Modelling analysis performed by Battaglia et al.[14] shows that recombination losses occurring at the back contact, accounts for about half of the total recombination losses of the cell. Additionally, Al is a poor back reflector since it only reflects a fraction of infrared light back into the Si absorber.

To alleviate the strong recombination losses of Al-BSF cells, Passivated Emitter and Rear Cell (PERC) cells were developed by applying a di-electric layer stack and locally forming Al contacts. The fabrication of the cell only requires few more steps in comparison to the Al-BSF structure, as shown in Figure 1.4. Current PERC cells commonly utilizes a selective emitter where heavy doping is added and aligned underneath the front metal grid. As a result, a lighter doping can be used outside of the contact region which reduces the Auger recombination and free carrier absorption. Additionally, contact openings at the rear side are made – typically by laser ablation – through a passivating dielectric layer and subsequently Al is screen-printed and fired, allowing for localized $p+$ regions formation. This approach also improves the internal reflection inside the Si absorber due to the low refractive index of the dielectric layer. Typically, dielectric stacks, such as Al_2O_3 and SiN_x:H films are used because of their excellent chemical passivation properties and the negative fixed charge provided by the Al_2O_3 layer creates an accumulation of holes near the Si surface. Table 1.1 shows the electrical characteristics of typical Al-BSF and PERC cells. By reducing the rear recombination losses, the V_{oc} of the cell and thereby a higher fill factor (FF) can be achieved [17]. However, the efficiency of PERC cells are still limited by the recombination at the metal contact.

1.4.2. SHJ CONTACTS

The main feature of Silicon Heterojunction (SHJ) solar cell is its high attainable cell V_{oc}. This originates from the excellent chemical surface passivation properties of

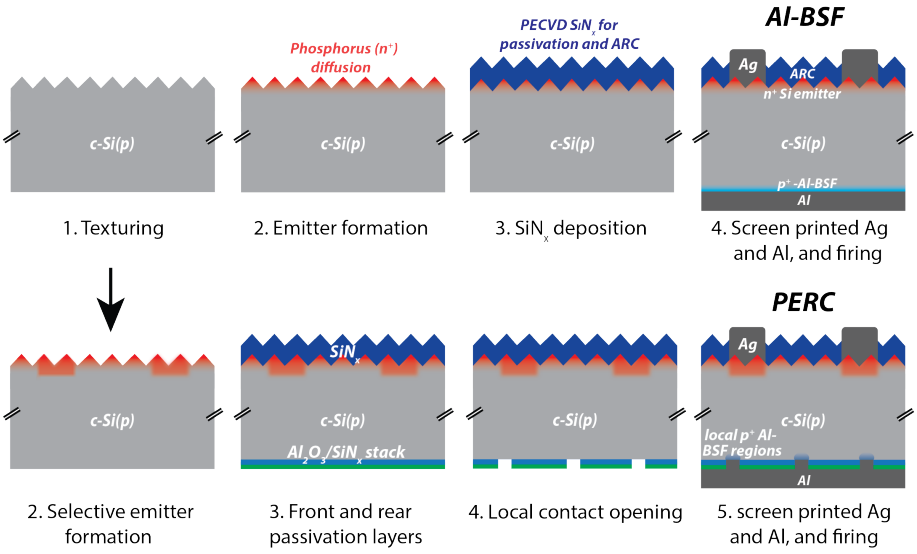

Figure 1.4.: Main fabrication steps of Al-BSF and PERC solar cell.

Table 1.1.: Comparison of electrical characteristics for large area Al-BSF and PERC cells.

Solar cells	V_{oc} [mV]	J_{sc} [mA/cm^2]	FF [%]	η [%]
Al-BSF [18]	645	38.9	80.7	20.3
PERC [19]	691	41.2	82.8	23.6

the intrinsic hydrogenated amorphous Si (a-Si:H(i)) interlayer. Carrier-selectivity is achieved by depositing doped a-Si:H layers on top of the interlayer. Band bending is induced near the Si surfaces because of the difference in WF between the doped a-Si:H layer and the Si absorber, as shown in Figure 1.5. Note that a-Si:H layer have a wider band-gap (~1.6 eV) in comparison to c-Si (1.12 eV) which results in a band offsets at the interfaces. To overcome these energy barriers, majority carriers' transport depends on thermionic or/and tunneling transport mechanisms. Because of the low lateral conductivity of the a-Si:H layers, a transparent conductive oxide (TCO), typically indium tin oxide (ITO), is required to allow lateral transport of carriers to the metal electrodes. Note that the TCO film also acts as an anti-reflection coating.

One of the efficiency limitation of SHJ cells is the parasitic absorption induced by a-Si layers. Although only a few nanometer thick is required to provide excellent surface passivation and carrier-selectivity, a-Si films have a direct bandgap of ~1.6 eV and results in significant short-circuit current (J_{sc}) losses. Figure 1.6 shows the combined J_{sc} loss caused by the thickness a-Si:H(i) and a-Si:H(p) films. Several materials, based on nanocrystalline Si and/or alloying with carbon or oxygen, are being developed to mitigate the optical losses of SHJ solar cells [20, 21]. However,

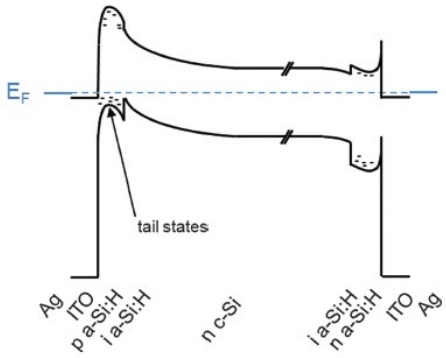

Figure 1.5.: Energy band diagram of a SHJ solar cell in equilibrium, taken from [14].

the optical gain of these wider bandgap materials often results in the deterioration of the electrical properties due to carriers transport hindrance [22].

The fabrication process of SHJ mainly consists of surface texturing and sequential cleaning steps, instrinsic and doped a-Si:H layers deposition (typically by PECVD), front and rear TCO layers deposition, low temperature screen-printed Ag grid, and a low temperature annealing, also called curing. The latter is typically performed at ~ 200 °C and is required to recover the surface passivation damage introduced by sputtered TCO deposition, TCO crystallization, and is an essential back end treatment during metallization and TCO post-crystallization. Figure 1.7 shows the process flow of SHJ solar cell. Despite the high efficiency of the SHJ, further development is required for the technology to improve its cost competitiveness. The main bottleneck of this technology is that no processing at temperatures higher than 200 °C is possible after the a-Si films deposition and thus excluding well-established fired industrial screen-printed metal contacts. Moreover, it's worth noting that low-temperature Ag pastes generally exhibit lower performance compared to high-temperature pastes. Nonetheless, recent advancements, such as enhanced bulk conductivity, improved finger spreading techniques, and innovations like Smartwire technology, have played a pivotal role in narrowing this performance gap [24].

1.4.3. POLY-SI CONTACTS

Doped poly-Si passivating contacts utilize an ultra-thin tunneling SiO_x interlayer (1-3 nm) to passivate the Si surface while allowing good transport of carriers. Transport of majority carriers through the SiO_x interlayer is achieved either by tunneling for thinner interlayers (<1.3 nm) or by pinholes for thicker interlayers, or a combination of both [25]. Poly-Si contacts are heavily doped with boron or phosphorus which induces a band bending near the Si interface, and therefore forming a selective contact. SiO_x typically pose a higher tunneling transport barrier to holes than to electrons due to the differences in energy band level, as shown in Figure 1.8. Consequently, direct band to band tunneling transport of holes across the

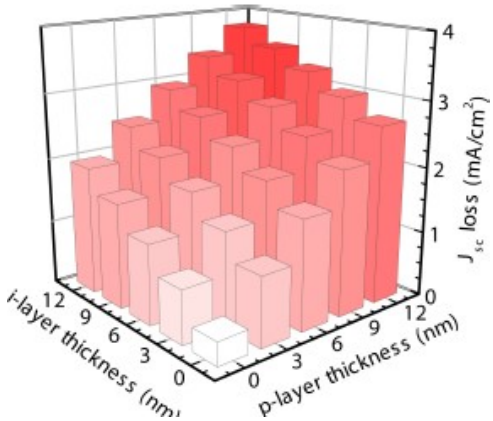

Figure 1.6.: J_{sc} losses in terms of a-Si:H(i) and a-Si:H(p) layer thicknesses, taken from [23].

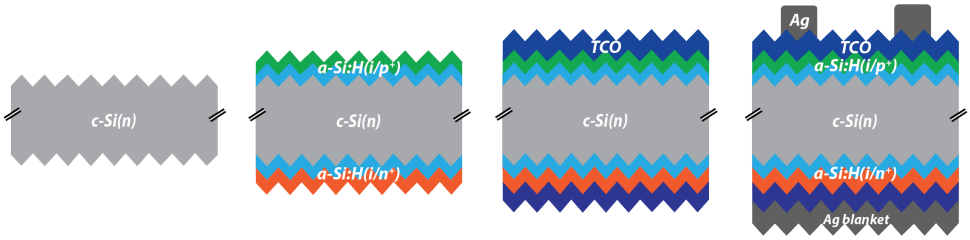

Figure 1.7.: Schematic showing the main manufacturing steps of SHJ cell.

interlayer is less probable in a poly-Si(p+) contact. To achieve hole carrier transport, the SiO_x interlayer requires certain level of structural modifications which can be resolved by either creating pinholes or local thickness reduction. This is attained by annealing the contact at temperature higher than 900 °C which causes in-diffusion of dopants into the Si absorber [25]. Poly-Si contacts are more compatible with the current industry standard processing while offering various fabrication routes. The manufacturing of the contact can be manufactured in four main steps: formation of SiO_x interlayer (by thermally [25, 26], plasma oxidation [27], HNO_3 oxidation [28], O_3, or UV/O_3 oxidation [29]), deposition of poly-Si (or a-Si), anneal at high temperature (700- 1050 °C), and a hydrogenation step to improve the surface passivation. Poly-Si contacts can be integrated at as a rear contact with a front boron diffusion contact, also known as tunnel oxide passivated contacts (TOPCon) structure, or by employing a dual scheme of poly-Si contacts on both the front and rear sides. The latter configuration prevents front metal recombination; however, the advantages gained in passivation are counteracted by a decline in optical performance due to free carrier absorption losses in poly-Si contacts.

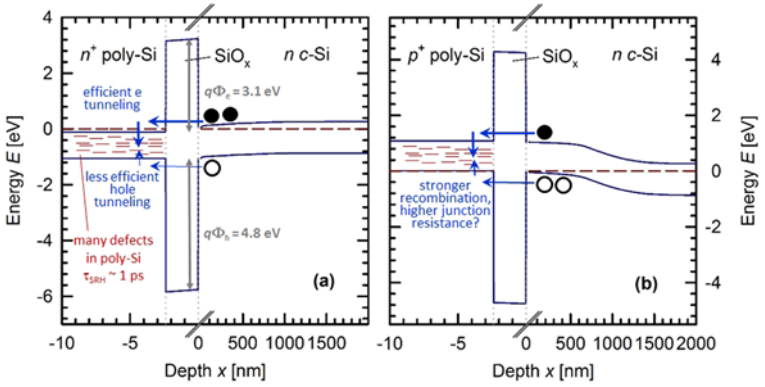

Figure 1.8.: Energy band diagrams of poly-Si(n+) (left) and poly-Si(p+) (right), taken from [25].

1.4.4. METAL OXIDE CONTACTS

All of the above contacts use extrinsic doping in order to achieve carrier selectivity. However, as mentioned above, doping has several drawbacks, such as increase in Auger recombination and significant parasitic absorption especially when placed on the front side of a solar cell. In contrast, metal oxides, such as MoO_x and TiO_x exhibit much wider bandgaps and WF ranges. Figure 1.9 compares absorption coefficient of these metal oxides and doped Si-based contacts under a AM 1.5g solar spectrum, and the maximum attainable J_{sc} of these contacts. Additionally, these metal oxide layers are typically thinner in comparison to doped Si contacts when used in a Si solar cell, thereby enabling a higher J_{sc}.

Similar to Si-based passivating contacts, metal oxide contacts utilize their differing WFs in relation to c-Si absorber to induce band bending near the Si interface when

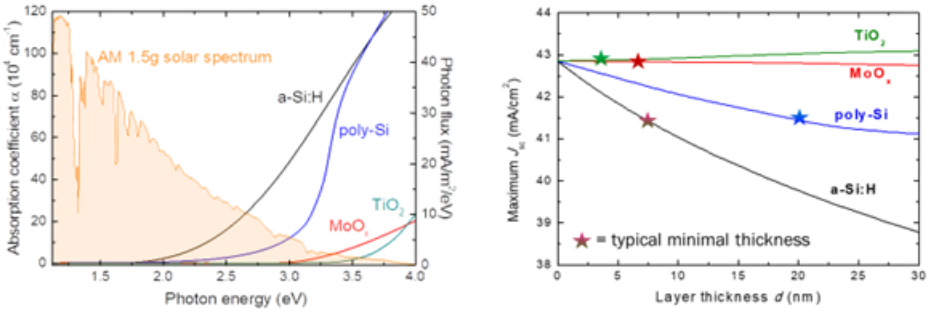

Figure 1.9.: (left) Absorption coefficient curve of different passivating contacts, (right) maximum achievable J_{sc} and the typical thickness of these contacts, taken from [30].

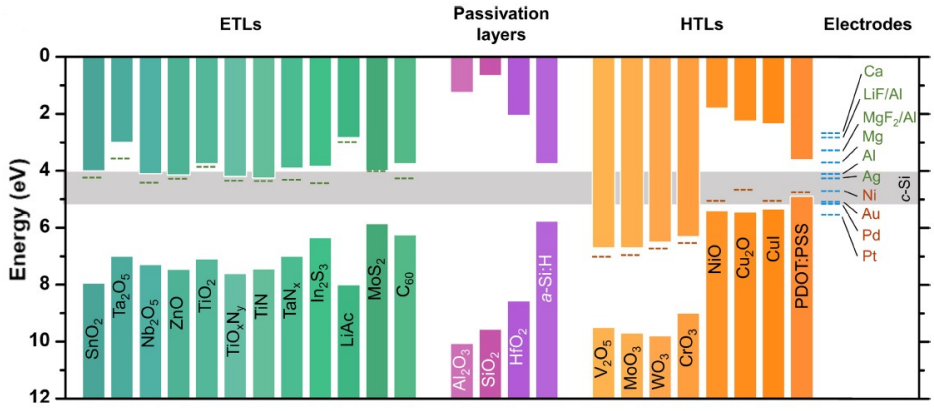

Figure 1.10.: Band gaps and WF of several electron and hole transport layers (ETLs and HTLs) with respect to c-Si band gap edges, taken from [31].

contacted with Si. However, the energy bands have to be well aligned with Si bands. Figure 1.10 shows the band gap of various materials, including metal oxides, with respect to the conduction and valence bands of c-Si absorber. For instance, *n*-type materials, such as TiO_x[32, 33], NbO_x[34], TaO_x[35], GaO_x[36], ZnO_x[37] have been explored as electron contacts due to their good conduction band alignment and a high energy barrier to holes. As a result, electrons perceive little resistance to the contact while high resistance exists for holes. Among the above, TiO_x has shown to be the most prominent electron contact. Efficiency above 23% has been achieved by the insertion of TiO_x/LiF_x stack between the Si absorber and the Al contact in a PERC-like structure [38]. Note that LiF_x has shown to be beneficial when combined with TiO_x due to its low WF property. At the hole contact, *p*-type NiO_x has favorable valence band alignment with Si while hindering electron transport. Alternatively, *n*-type metal oxides, such as MoO_x, VO_x, WO_x have been prominently used as hole selective contacts mainly because of their high WF properties. In such cases, effective hole transport is possible through band to band transport. In particular, high conversion efficiency of 23.8% has been achieved by replacing an a-Si:H(*p*) by MoO_x in a SHJ structure with significant J_{sc} gain [39]. However, this structure has shown to degrade after an anneal at temperature higher than 130 °C which is a bottleneck in terms of SHJ processing using screen-printed contacts.

1.5. C-SI SOLAR CELLS EVOLUTION & FUTURE TRENDS

Figure 1.11 shows the efficiency evolution of various c-Si solar cell technologies in recent years. The mass industrialization of solar cells commenced by the introduction of Al-BSF technology. This simplicity approach allowed for a robust processing sequence and a stable device, and has encompassed of the majority of the market share over the last decades. However, the conversion efficiency of industrial Al-BSF cells has plateaued to around 20% mainly because of the

recombination losses perceived at the rear contact. In the pursue of further cell efficiency improvement, the development of PERC solar cells with local rear contacts (See Figure 1.12(b)) has enabled for better electrical and optical properties. While the concept (known as passivated emitter with rear locally diffused, PERL) was initially developed in 1980's [40] and has demonstrated an efficiency of 25% more than 20 years ago [9], the transfer from laboratory to industry has proven to be problematic due to the cost effectiveness of the technology. Nevertheless, with the introduction of cost effective processes and high throughput equipment, such as PECVD surface passivating layers, and laser ablation [41], PERC technology is currently the main technology within the PV industry with a low cost and large-volume production. In 2020, the typical efficiency of industrial PERC solar cells were between 21.5 to 23% while achieving a record efficiency of 24.5% on industrial size wafers [42]. While the PERC structure mitigate the losses between the metal electrode and the Si absorber, power loss is still dominated by the recombination at the localized contact.

Alternative solar cell concepts, based on passivating contacts, were developed to avoid the recombination losses occurring at the Si/metal interface. SHJ solar cells, also known as HIT (heterojunction with intrinsic thin layer) cells, were initially developed by Sanyo in the 1980s and utilize a stack intrinsic and doped hydrogenated amorphous layers to passivate the surface of the Si base, as shown in Figure 1.12(c). The excellent passivation properties of the a-Si:H(i) interlayer enable for high attainable V_{oc} up to 750 mV with achieved efficiency of above 25% [49]. Nevertheless, SHJ solar cells are incompatible with well established fired screen-printing methods because of its low temperature tolerance. More recently, doped polysilicon-based passivating contacts (TOPCon) have shown to be an alternative to SHJ due manufacturing processes that are more adequate for conventional silicon solar cell processing. This solar cell architecture consists of a front side diffused emitter (similar to the PERC structure) and makes use of an ultra-thin passivating SiO_x film in between the Si and the poly-Si(n+) contact at the rear side to reduce the charge carriers recombination. The schematic of the cell architecture is show in Figure 1.12(d). Accordingly, a record conversion efficiency of 26.9% was achieved with a doped poly-Si passivating contact structure on industrial size wafers [64].As a result, the industry is transitioning from PERC to TOPCon technology.

One of the main disadvantages of Si-based passivating contacts is the absorption losses when placed on the sunny side of a solar cell. This can be overcome by using an interdigitated back contact (IBC) structure in which both p- and n-contacts are placed at the rear side of the cell. As a result, a record efficiency for c-Si solar cell of 26.7% was achieved using a cell structure based on a-Si:H films, as shown in Figure 1.12(e). However, IBC cells often require additional manufacturing steps which makes the development of double sided contacts solar cells still the preferable choice in industry. Alternatively, passivating and carrier-selective contacts based on metal oxides are being explored due to their high transparency to visible light and their simplistic fabrication processes. Passivating contacts, such as MoO_x and TiO_x have shown to be able to act as hole and electron selective contacts, respectively. A full metal oxide solar cell has been developed by Bullock et al.[65] with conversion

efficiency above 20% by using a cell architecture shown in Figure 1.12(f).

Figure 1.13 illustrates the current and projected future market shares of various cell technologies. As per the ITRPV 2023 results [66], the Al-BSF solar cell is anticipated to be phased out in the coming year. Presently, the majority of the market is comprised of PERC solar cells; however, it is expected that their production will decline in the near future, giving way to the adoption of TOPCon technology. Furthermore, the market share of SHJ solar cells is also projected to grow steadily, increasing from approximately 9% to over 25% within the next decade. It is important to note that double-sided contacts will dominate the market during this period. In summary, the future trend in solar cell technology is transitioning towards higher efficiency solar cells, driven by the replacement of outdated technologies and

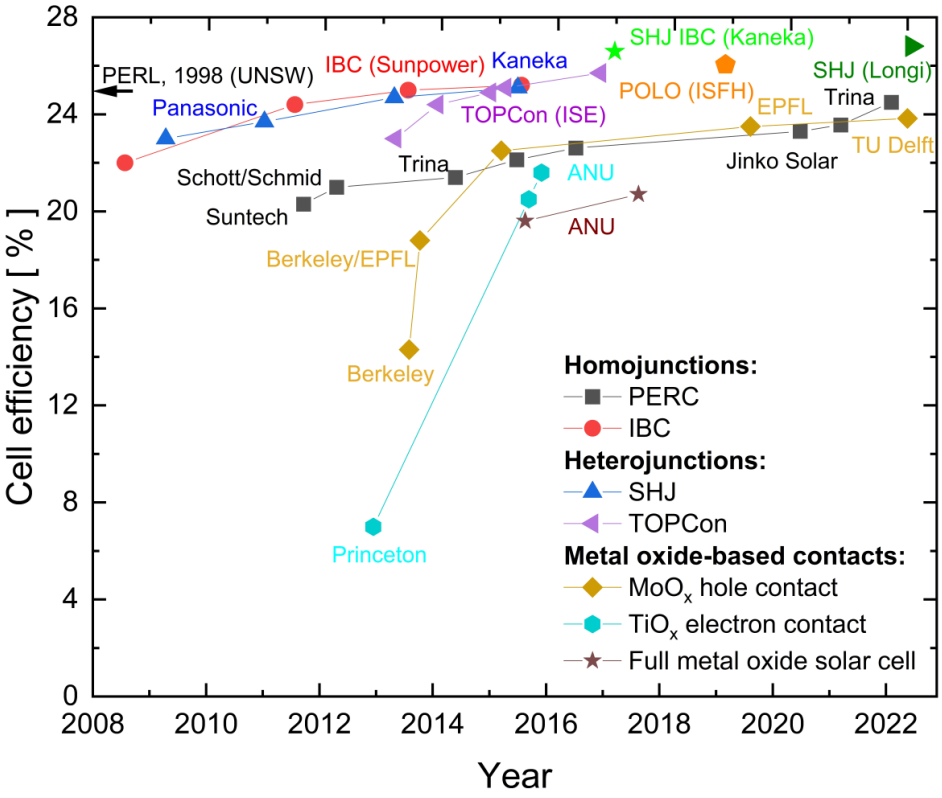

Figure 1.11.: Record efficiencies chart of a selection of c-Si solar architectures: PERL (passivated emitter, rear locally diffused) by reported UNSW [43], PERC cells reported by [42, 44–48], IBC by reported Sunpower [14], SHJ reported by Panasonic, Sanyo, and Kaneka [49–52], TOPCon reported by ISE [28, 29, 53, 54], SHJ IBC reported by Sanyo [55], SHJ reported by Longi [56], POLO reported by ISFH [57], MoO_x-based contacts reported by Berkeley, EPFL, TU Delft [39, 58–61], TiO_x-based contacts reported by Princeton and ANU [32, 62, 63].

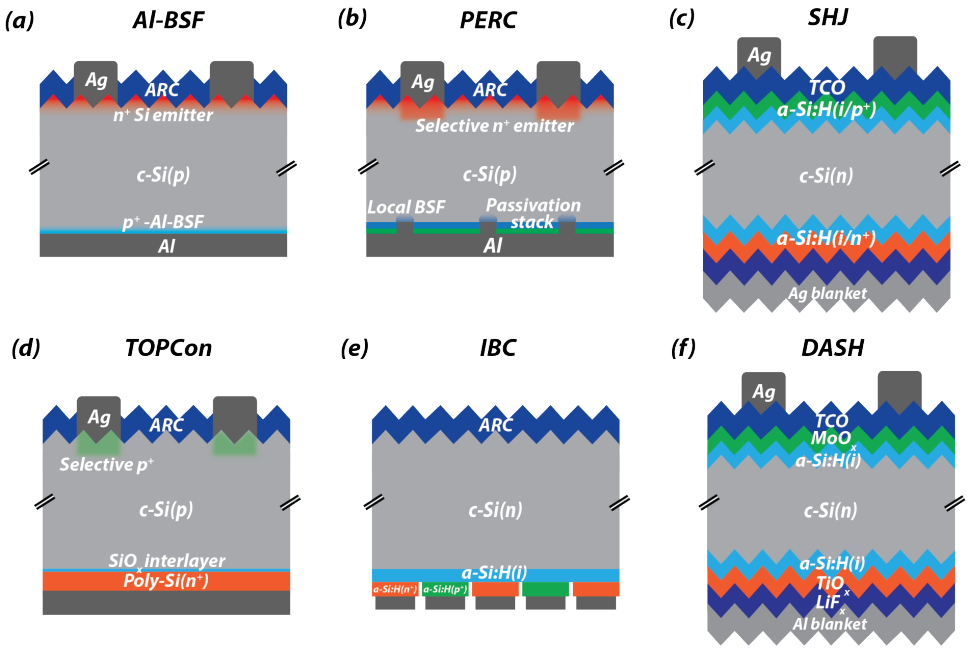

Figure 1.12.: Schematic of different cell designs. (a) Al-BSF cell made on p-type Si wafers with a front ARC and passivating SiN_x layer, and a rear Al-BSF contact. (b) PERC cell made on p-type Si wafers with a front selective $n+$ emitter and a Al_2O_3/SiN_x passivating stack. Local opening are formed, and subsequently Al is screen-printed and fired to form contact. (c) SHJ cell with an a-Si:H(i) interlayer on both sides. Selectivity is achieved by p- and n- doped a-Si layers and capped with TCOs. Low temperature Ag paste is screen-printed on the front and anneal to form a good contact. (d) TOPCon structure using a selective $p+$ on the front and a rear poly-Si contact. (e) IBC cell passivated with a-Si:H(i) while selectivity is achived by a-Si:H($p+$) and a-Si:H($n+$) layers. (f) Dopant-free asymmetric heterocontact (DASH) cell is passivated by a-Si:H(i) while hole and electron selectivity is achieved by MoO_x and TiO_x/LiF_x stack, respectively.

the increasing prominence of advanced cell designs.

1.6. FRAMEWORK OF THIS THESIS

This thesis provides scientific insights on the application of metal oxide contacts for c-Si solar cells, and several possible fabrication routes aimed towards the industrial implementation of these contacts. The efficiency of c-Si solar cells has annually increased by 0.5-0.6%abs, enabling in a decrease in LCoE [67]. In order to maintain this improvement rate, new technologies have to be developed and integrated towards the industrialization of these solar cells. With the transition towards high-efficiency solar cells, passivating contacts have become a prominent solution to improve the practical efficiency limit of single junction Si solar cells.

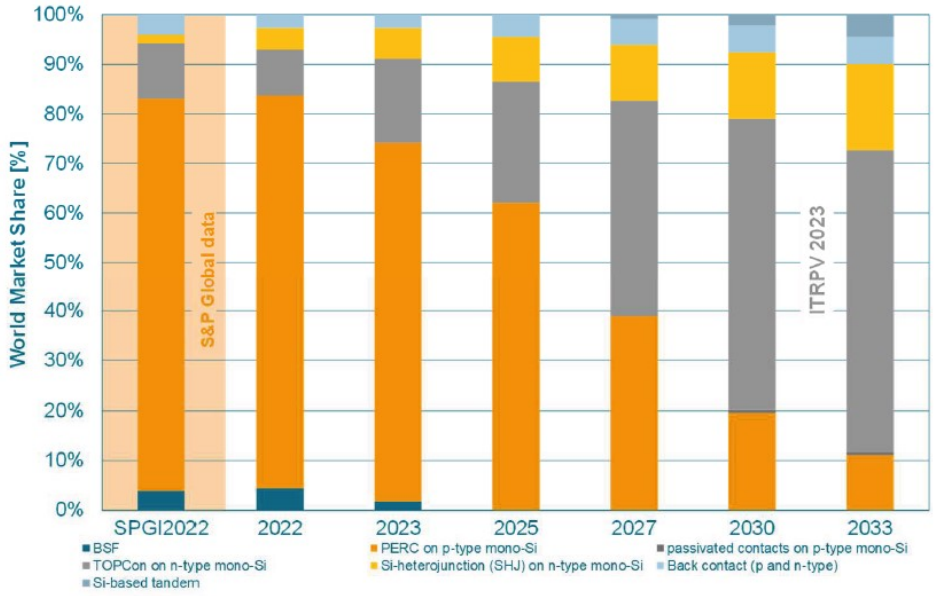

Figure 1.13.: Current and future market shares of various cell technologies. Figure taken from [66].

Currently, state of the art Si-based passivating contacts are still limited by their parasitic absorption losses which in turn limit the achievable efficiency. For this reason, metal oxides contacts are still a good alternative to reduce these losses. Furthermore, additional advancements in metal oxide contacts can greatly benefit the development of thin-film solar cells, including perovskite and tandem devices that also rely on the application of metal oxide contacts.

The application of metal oxide contacts have shown to provide significant J_{sc} gain by replacing an a-Si:H(p+) layer with MoO_x layer, in a SHJ structure. However, the development of this contact has been hampered by its lack of thermal stability which causes significant carrier-selectivity losses. The reason of this selectivity loss is partially caused by the impediment of hole transport by the a-Si:H(i) interlayer. As a result, we investigate alternative passivating interlayers, such as ultra-thin Al_2O_3 and SiO_y interlayer that can promote the extraction of holes while improving the thermal stability of a MoO_x-based Si solar cell. This thesis highlights the important interlayer parameters that is required to promote the collection of majority carriers, and hence improving the carrier-selectivity of MoO_x contacts. Additionally, a novel hydrogenation method is developed and can be adapted for several low temperature contacts. The reason is that conventional hydrogenation strategies - generally used for poly-Si contacts – degrades the properties of several metal oxides under high thermal exposure. Consequently, we have developed a hydrogenation method based on selective etching of an atomic layer deposited (ALD) Al_2O_3 film. By selectively

etching the Al_2O_3 layer, the highly passivated ultra-thin SiO_y, that is naturally formed during ALD Al_2O_3 deposition at the Si interface and is the origin of the excellent surface passivation properties of Al_2O_3 films, can be utilized for MoO_x contact. To the best of our knowledge, this approach yielded to the highest surface passivation (with an average iV_{oc} ~ 710 mV on 6 inch textured Si) for a MoO_x contact on an oxide interlayer.

This thesis also explores the applicability of the pulsed laser deposition (PLD) technique for the growth of metal oxide and TCO layers for c-Si solar cells. PLD provides several advantages in comparison to conventional techniques, such as sputtering. This is because PLD offers a broader range of tunable parameters and possesses a "soft" deposition characteristic. Moreover, its flexibility allows for the deposition of various materials, enabling in-situ deposition of metal oxide and TCO films. This capability is particularly crucial considering the WF degradation of MoO_x when exposed to air. Moreover, PLD shows to mitigate the damage typically induced during TCO sputtering on poly-Si contacts; the sputter-induced damage on poly-Si contacts is much more difficult to repair, and requires higher annealing temperature (~350 °C) to mitigate the surface passivation damage [22]. However, this impedes charge carrier transport across the poly-Si/TCO interface possibly due to the formation of a SiO_x interfacial layer [68–70]. Additionally, thinner poly-Si layers suffer from more severe sputter-induced damage since they cannot properly shield the c-Si/SiO_y interface from UV radiation and particle bombardment. Therefore, minimizing the poly-Si thickness – to further improve the photogenerated current of the cell, is compromised by the aggravating sputter-induced passivation loss of the contact.

The following chapters of this thesis are described as follows:

Chapter 2 elaborates on the various fabrication techniques utilized for the manufacturing and charactization of solar cells. Further details on these fabrication techniques used for c-Si solar cells are thoroughly explained.

In chapter 3, we developed a MoO_x contact with an ultra-thin ALD Al_2O_3/SiO_y interlayer, showing good contact selectivity, cell thermal stability, and transparency. Ultra-thin oxide interlayers offer several advantages in comparison to an a-Si:H(i) interlayer such as, minimal parasitic absorption and improved induced band bending [71]. It is presented that the hole carrier-selectivity of the MoO_x contact is highly dependent on Al_2O_3 interlayer properties. While a post-deposition anneal (PDA) treatment is often required to activate the passivation of Al_2O_3 layer on c-Si, it is shown that this treatment hampers the transport of hole carriers due to an inefficient tunneling transport. Hence, the best MoO_x cell was obtained with an as-deposited Al_2O_3 interlayer. However, the surface passivation is limited by the quality of the interlayer.

In Chapter 4, we delve into fundamental insights to comprehensively understand the impact of the properties of various interlayers on carrier selectivity of MoO_x contact. Through a series of 2D simulations, we define critical parameters that significantly influence contact selectivity.

In chapter 5, different hydrogenation strategies are explored to improve the surface passivation of the MoO_x/Al_2O_3 contact. The interaction of atomic H with

MoO_x can degrade the performance of the stack. As a result, an alternative hydrogenation approach is developed by using a selective etching method based on a tetramethylammonium hydroxide (TMAH) solution. Al_2O_3 deposited on Si results in the natural formation of an ultrathin SiO_y interlayer at the Si interface and is the origin of the chemical passivation. By etching off the Al_2O_3 film, an ultrathin passivating SiO_y interlayer can be obtained and used as a tunneling interlayer.

In chapter 6, a PLD ITO layer is developed for ultra-thin doped poly-Si contacts. The optical and electrical properties of ITO films deposited via PLD and sputtering are explored and evaluated against each other. The optimum resistivity values obtained with PLD ITO during the deposition is similar to the value obtained from the sputtered ITO layers. However, the induced damage upon ITO deposition is considerably lower with the PLD technique in comparison to sputtering.

In chapter 7, the contact selectivity of MoO_x and TiO_x layers deposited by PLD, are explored. The effects of various parameters, such as laser energy, repetition rate, oxygen and argon gas ratio and chamber pressure are investigated on surface passivation and contact selectivity. These parameters play an important role in determining the electronic and optical properties of the layers, and hence the carrier selectivity of the contacts.

Finally, chapter 8 reports on the conclusions of this thesis. An outlook on the possible future works on transparent passivating and carrier-selective contacts for c-Si solar cells is also presented.

1.7. CONTRIBUTION OF THIS THESIS TO THE RESEARCH FIELD

The contributions of the thesis project are highlighted as shown below:

1. A highly carrier-selective MoO_x contact was developed by utilizing an ultra-thin tunneling Al_2O_3/SiO_y interlayer. The passivating contact was fabricated with pilot industrial tools and demonstrated cell efficiency of 18.2 % on 6” full area Si substrate. In addition, the $MoO_x/Al_2O_3/SiO_y$ contact shows good thermal stability up to 210 °C, as published in [72]. Nevertheless, further development is required to improve the surface passivation properties of the interlayer.

2. To further improve the surface passivation of our MoO_x contact, an ultra-thin oxide interlayer was developed by selectively etching an ALD Al_2O_3 film in a TMAH solution. This is possible because of the low etching rate of SiO_y in a TMAH solution. The oxide – which is originally formed during the initial ALD cycles - shows excellent surface passivation properties and when combined with a MoO_x layer results in iV_{oc} of 710 mV. This is the highest iV_{oc} value reported for a MoO_x contact with an oxide interlayer, according to the author’s knowledge. Nevertheless, further etching optimizations are still required to reduce the contact resistivity of the MoO_x contact. The highly passivated oxide interlayer allows for further exploration and adaptation on various metal oxides, or low temperature contacts.

3. Low induced surface passivation damage and excellent contact resistivity was achieved by PLD ITO deposition on ultra-thin poly-Si(n+) contacts (<20 nm),

as published in [73]. This is because PLD enables a softer landing of species on the surface of the stack in comparison to PVD technique. Further improvement can be achieved by increasing the chamber deposition pressure > 0.1 mbar. The low contact resistivity at high annealing temperature is likely caused by the suppression of a parasitic interfacial oxide at the poly-Si/ITO interface. This enables for the development of thinner poly-Si (~ 10 nm) layers which allows for reduced parasitic absorption in the contact.

4. Metal oxide contacts deposited by PLD, notably MoO_x and TiO_x were explored for c-Si solar cells. A PLD MoO_x -based solar cell with efficiency of 16.1 % was initially obtained and was limited by an S-shaped IV curve. However, the MoO_x layer optical properties and carrier-selectivity can be improved by increasing the deposition pressure. TiO_x contact shows excellent passivation properties on both a-Si:H(i) and SiO_y interlayer with iV_{oc} of 730 mV and 702 mV, respectively.

REFERENCES

[1] N. M. Haegel, R. Margolis, T. Buonassisi, D. Feldman, A. Froitzheim, R. Garabedian, M. Green, S. Glunz, H.-M. Henning, B. Holder, *et al.* "Terawatt-scale photovoltaics: Trajectories and challenges". In: *@inproceedingsscire2020analysis, title=Analysis of Transition Metal Oxides based Heterojunction Solar Cells with S-shaped JV curves, author=Scirè, Daniele and Bonadonna, Marco and Zhao, Yifeng and Procel, Paul and Isabella, Olindo and Zeman, Miro and Macaluso, Roberto and Mosca, Mauro and Crupi, Isodiana, booktitle=2020 AEIT International Annual Conference (AEIT), pages=1–6, year=2020, organization=IEEE Science* 356.6334 (2017), pp. 141–143.

[2] C. Ballif, F.-J. Haug, M. Boccard, P. J. Verlinden, and G. Hahn. "Status and perspectives of crystalline silicon photovoltaics in research and industry". In: *Nature Reviews Materials* 7.8 (2022), pp. 597–616.

[3] IEA-PVPS. "Snapshot of Global PV Markets 2023". In: *International Energy Agency (IEA): Paris, France* (2023).

[4] D. Ray. "Lazard's Levelized Cost of Energy Analysis—Version 13.0". In: *Lazard: New York, NY, USA* 20 (2019).

[5] E. Bellini. *Saudi Arabia's second PV tender draws world record low bid of $ 0.0104/kWh*. 2021. URL: https://www.pv-magazine.com/2021/04/08/saudi-arabias-second-pv-tender-draws-world-record-low-bid-of-0104-kwh/ (visited on 02/22/2022).

[6] N. M. Haegel, H. Atwater Jr, T. Barnes, C. Breyer, A. Burrell, Y.-M. Chiang, S. De Wolf, B. Dimmler, D. Feldman, S. Glunz, *et al.* "Terawatt-scale photovoltaics: Transform global energy". In: *Science* 364.6443 (2019), pp. 836–838.

[7] P. Verlinden. "Future challenges for photovoltaic manufacturing at the terawatt level". In: *Journal of Renewable and Sustainable Energy* 12.5 (2020), p. 053505.

[8] C. Breyer, D. Bogdanov, A. Gulagi, A. Aghahosseini, L. S. Barbosa, O. Koskinen, M. Barasa, U. Caldera, S. Afanasyeva, M. Child, *et al.* "On the role of solar photovoltaics in global energy transition scenarios". In: *Progress in Photovoltaics: Research and Applications* 25.8 (2017), pp. 727–745.

[9] Y. Chen, P. P. Altermatt, D. Chen, X. Zhang, G. Xu, Y. Yang, Y. Wang, Z. Feng, H. Shen, and P. J. Verlinden. "From laboratory to production: learning models of efficiency and manufacturing cost of industrial crystalline silicon and thin-film photovoltaic technologies". In: *IEEE Journal of photovoltaics* 8.6 (2018), pp. 1531–1538.

[10] M. Victoria, N. Haegel, I. M. Peters, R. Sinton, A. Jäger-Waldau, C. del Cañizo, C. Breyer, M. Stocks, A. Blakers, I. Kaizuka, *et al.* "Solar photovoltaics is ready to power a sustainable future". In: *Joule* 5.5 (2021), pp. 1041–1056.

[11] Fraunhofer ISE. *Photovoltaics report*. 2023. URL: https://www.ise.fraunhofer.de/en/publications/studies/photovoltaics-report.html (visited on 02/22/2022).

[12] A. Cuevas, T. Allen, J. Bullock, Y. Wan, D. Yan, and X. Zhang. "Skin care for healthy silicon solar cells". In: *2015 IEEE 42nd Photovoltaic Specialist Conference (PVSC)*. IEEE. 2015, pp. 1–6.

[13] U. Würfel, A. Cuevas, and P. Würfel. "Charge carrier separation in solar cells". In: *IEEE Journal of Photovoltaics* 5.1 (2014), pp. 461–469.

[14] C. Battaglia, A. Cuevas, and S. De Wolf. "High-efficiency crystalline silicon solar cells: status and perspectives". In: *Energy & Environmental Science* 9.5 (2016), pp. 1552–1576.

[15] P. P. Altermatt, J. O. Schumacher, A. Cuevas, M. J. Kerr, S. W. Glunz, R. R. King, G. Heiser, and A. Schenk. "Numerical modeling of highly doped Si: P emitters based on Fermi–Dirac statistics and self-consistent material parameters". In: *Journal of Applied Physics* 92.6 (2002), pp. 3187–3197.

[16] R. King, R. Sinton, and R. Swanson. "Studies of diffused phosphorus emitters: saturation current, surface recombination velocity, and quantum efficiency". In: *IEEE Transactions on electron devices* 37.2 (1990), pp. 365–371.

[17] A. Polman, M. Knight, E. C. Garnett, B. Ehrler, and W. C. Sinke. "Photovoltaic materials: Present efficiencies and future challenges". In: *Science* 352.6283 (2016), aad4424.

[18] K. H. Kim, C. S. Park, J. D. Lee, J. Y. Lim, J. M. Yeon, I. H. Kim, E. J. Lee, and Y. H. Cho. "Record high efficiency of screen-printed silicon aluminum back surface field solar cell: 20.29%". In: *Japanese Journal of Applied Physics* 56.8S2 (2017), 08MB25.

[19] Aleina. *Talesun Solar Announces 23.56% PERC Solar Cell Conversion Efficiency*. 2020. URL: https://www.pvtime.org/talesun-solar-announces-23-56-perc-solar-cell-conversion-efficiency/ (visited on 02/24/2022).

[20] D. Pysch, M. Bivour, M. Hermle, and S. W. Glunz. "Amorphous silicon carbide heterojunction solar cells on p-type substrates". In: *Thin Solid Films* 519.8 (2011), pp. 2550–2554.

[21] K. Ding, U. Aeberhard, F. Finger, and U. Rau. "Optimized amorphous silicon oxide buffer layers for silicon heterojunction solar cells with microcrystalline silicon oxide contact layers". In: *Journal of Applied Physics* 113.13 (2013), p. 134501.

[22] J. P. Seif, D. Menda, A. Descoeudres, L. Barraud, O. Özdemir, C. Ballif, and S. De Wolf. "Asymmetric band offsets in silicon heterojunction solar cells: Impact on device performance". In: *Journal of Applied Physics* 120.5 (2016), p. 054501.

[23] Z. C. Holman, A. Descoeudres, L. Barraud, F. Z. Fernandez, J. P. Seif, S. De Wolf, and C. Ballif. “Current losses at the front of silicon heterojunction solar cells”. In: *IEEE Journal of Photovoltaics* 2.1 (2012), pp. 7–15.

[24] Y. Liu, Y. Li, Y. Wu, G. Yang, L. Mazzarella, P. Procel-Moya, A. C. Tamboli, K. Weber, M. Boccard, O. Isabella, *et al.* “High-efficiency silicon heterojunction solar cells: materials, devices and applications”. In: *Materials Science and Engineering: R: Reports* 142 (2020), p. 100579.

[25] R. Peibst, U. Römer, Y. Larionova, M. Rienäcker, A. Merkle, N. Folchert, S. Reiter, M. Turcu, B. Min, J. Krügener, *et al.* “Working principle of carrier selective poly-Si/c-Si junctions: Is tunnelling the whole story?” In: *Solar Energy Materials and Solar Cells* 158 (2016), pp. 60–67.

[26] M. Stodolny, J. Anker, C. Tool, M. Koppes, A. Mewe, P. Manshanden, M. Lenes, and I. Romijn. “Novel schemes of p+ poly-Si hydrogenation implemented in industrial 6 bifacial front-and-rear passivating contacts solar cells”. In: *35th European Photovoltaic Solar Energy Conference and Exhibition*. International Conference EU PVSEC for Photovoltaic Research. 2018, pp. 414–417.

[27] F. Feldmann, J. Schoen, J. Niess, W. Lerch, and M. Hermle. “Studying dopant diffusion from Poly-Si passivating contacts”. In: *Solar Energy Materials and Solar Cells* 200 (2019), p. 109978.

[28] F. Feldmann, M. Bivour, C. Reichel, M. Hermle, and S. W. Glunz. “Passivated rear contacts for high-efficiency n-type Si solar cells providing high interface passivation quality and excellent transport characteristics”. In: *Solar energy materials and solar cells* 120 (2014), pp. 270–274.

[29] A. Moldovan, F. Feldmann, K. Kaufmann, S. Richter, M. Werner, C. Hagendorf, M. Zimmer, J. Rentsch, and M. Hermle. “Tunnel oxide passivated carrier-selective contacts based on ultra-thin SiO2 layers grown by photo-oxidation or wet-chemical oxidation in ozonized water”. In: *2015 IEEE 42nd Photovoltaic Specialist Conference (PVSC)*. IEEE. 2015, pp. 1–6.

[30] B. Macco, B. W. van de Loo, and W. M. Kessels. “Atomic Layer Deposition for High-Efficiency Crystalline Silicon Solar Cells”. In: *Atomic Layer Deposition in Energy Conversion Applications* (2017), pp. 41–99.

[31] Y. Wang, S.-T. Zhang, L. Li, X. Yang, L. Lu, and D. Li. “Dopant-free passivating contacts for crystalline silicon solar cells: Progress and prospects”. In: *EcoMat* (2023), e12292.

[32] X. Yang, P. Zheng, Q. Bi, and K. Weber. “Silicon heterojunction solar cells with electron selective TiOx contact”. In: *Solar Energy Materials and Solar Cells* 150 (2016), pp. 32–38.

[33] X. Yang, K. Weber, Z. Hameiri, and S. De Wolf. “Industrially feasible, dopant-free, carrier-selective contacts for high-efficiency silicon solar cells”. In: *Progress in photovoltaics: Research and Applications* 25.11 (2017), pp. 896–904.

[34] B. Macco, L. E. Black, J. Melskens, B. W. van de Loo, W.-J. H. Berghuis, M. A. Verheijen, and W. M. Kessels. "Atomic-layer deposited Nb2O5 as transparent passivating electron contact for c-Si solar cells". In: *Solar Energy Materials and Solar Cells* 184 (2018), pp. 98–104.

[35] Y. Wan, S. K. Karuturi, C. Samundsett, J. Bullock, M. Hettick, D. Yan, J. Peng, P. R. Narangari, S. Mokkapati, H. H. Tan, *et al.* "Tantalum oxide electron-selective heterocontacts for silicon photovoltaics and photoelectrochemical water reduction". In: *ACS Energy Letters* 3.1 (2017), pp. 125–131.

[36] T. Allen and A. Cuevas. "Electronic passivation of silicon surfaces by thin films of atomic layer deposited gallium oxide". In: *Applied Physics Letters* 105.3 (2014).

[37] J. Ding, Y. Zhou, G. Dong, M. Liu, D. Yu, and F. Liu. "Solution-processed ZnO as the efficient passivation and electron selective layer of silicon solar cells". In: *Progress in Photovoltaics: Research and Applications* 26.12 (2018), pp. 974–980.

[38] J. Bullock, Y. Wan, M. Hettick, X. Zhaoran, S. P. Phang, D. Yan, H. Wang, W. Ji, C. Samundsett, Z. Hameiri, *et al.* "Dopant-free partial rear contacts enabling 23% silicon solar cells". In: *Advanced Energy Materials* 9.9 (2019), p. 1803367.

[39] L. Cao, P. Procel, A. Alcañiz, J. Yan, F. Tichelaar, E. Özkol, Y. Zhao, C. Han, G. Yang, Z. Yao, *et al.* "Achieving 23.83% conversion efficiency in silicon heterojunction solar cell with ultra-thin MoOx hole collector layer via tailoring (i) a-Si: H/MoOx interface". In: *Progress in Photovoltaics: research and applications* (2022).

[40] A. W. Blakers, A. Wang, A. M. Milne, J. Zhao, and M. A. Green. "22.8% efficient silicon solar cell". In: *Applied Physics Letters* 55.13 (1989), pp. 1363–1365.

[41] G. M. Wilson, M. Al-Jassim, W. K. Metzger, S. W. Glunz, P. Verlinden, G. Xiong, L. M. Mansfield, B. J. Stanbery, K. Zhu, Y. Yan, *et al.* "The 2020 photovoltaic technologies roadmap". In: *Journal of Physics D: Applied Physics* 53.49 (2020), p. 493001.

[42] N. T. Prasad. *Trina Solar Achieves 23.39 % Efficiency in PERC Cells*. 2020. URL: https://www.mercomindia.com/trina-solar-achieves-23-39-percent-efficiency-perc-cells (visited on 01/23/2022).

[43] J. Zhao, A. Wang, M. A. Green, and F. Ferrazza. "19.8% efficient "honeycomb" textured multicrystalline and 24.4% monocrystalline silicon solar cells". In: *Applied physics letters* 73.14 (1998), pp. 1991–1993.

[44] Z. Wang, P. Han, H. Lu, H. Qian, L. Chen, Q. Meng, N. Tang, F. Gao, Y. Jiang, J. Wu, *et al.* "Advanced PERC and PERL production cells with 20.3% record efficiency for standard commercial p-type silicon wafers". In: *Progress in Photovoltaics: Research and Applications* 20.3 (2012), pp. 260–268.

[45] D. Chen, W. Deng, J. Dong, F. Ye, H. Zhu, H. Li, Y. Jiang, B. Gao, M. Zhong, Y. Cui, *et al.* "21.40% efficient large area screen printed industrial PERC solar cell". In: *CELL* 37 (2015), pp. 80–34.

[46] F. Ye, W. Deng, W. Guo, R. Liu, D. Chen, Y. Chen, Y. Yang, N. Yuan, J. Ding, Z. Feng, *et al.* "22.13% efficient industrial p-type mono PERC solar cell". In: *2016 IEEE 43rd Photovoltaic Specialists Conference (PVSC)*. IEEE. 2016, pp. 3360–3365.

[47] W. Deng, F. Ye, R. Liu, Y. Li, H. Chen, Z. Xiong, Y. Yang, Y. Chen, Y. Wang, P. P. Altermatt, *et al.* "22.61% efficient fully screen printed PERC solar cell". In: *2017 IEEE 44th Photovoltaic Specialist Conference (PVSC)*. IEEE. 2017, pp. 2220–2226.

[48] S. Enkjardt. *Trina Solar achieves 24.5 % efficiency for 210 mm p-type PERC solar cell*. 2022. URL: https://www.pv-magazine.com/2022/07/13/trina-solar-achieves-24-5-efficiency-for-210-mm-p-type-perc-solar-cell/ (visited on 02/01/2023).

[49] M. Taguchi, A. Yano, S. Tohoda, K. Matsuyama, Y. Nakamura, T. Nishiwaki, K. Fujita, and E. Maruyama. "24.7% record efficiency HIT solar cell on thin silicon wafer". In: *IEEE Journal of photovoltaics* 4.1 (2013), pp. 96–99.

[50] T. Mishima, M. Taguchi, H. Sakata, and E. Maruyama. "Development status of high-efficiency HIT solar cells". In: *Solar Energy Materials and Solar Cells* 95.1 (2011), pp. 18–21.

[51] K. Yamamoto, K. Yoshikawa, H. Uzu, and D. Adachi. "High-efficiency heterojunction crystalline Si solar cells". In: *Japanese Journal of Applied Physics* 57.8S3 (2018), 08RB20.

[52] D. Adachi, J. L. Hernández, and K. Yamamoto. "Impact of carrier recombination on fill factor for large area heterojunction crystalline silicon solar cell with 25.1% efficiency". In: *Applied Physics Letters* 107.23 (2015), p. 233506.

[53] S. W. Glunz, F. Feldmann, A. Richter, M. Bivour, C. Reichel, H. Steinkemper, J. Benick, and M. Hermle. "The irresistible charm of a simple current flow pattern–25% with a solar cell featuring a full-area back contact". In: *Proceedings of the 31st European Photovoltaic Solar Energy Conference and Exhibition*. München WIP. 2015, pp. 259–263.

[54] A. Richter, J. Benick, F. Feldmann, A. Fell, M. Hermle, and S. W. Glunz. "n-Type Si solar cells with passivating electron contact: Identifying sources for efficiency limitations by wafer thickness and resistivity variation". In: *Solar Energy Materials and Solar Cells* 173 (2017), pp. 96–105.

[55] K. Yoshikawa, H. Kawasaki, W. Yoshida, T. Irie, K. Konishi, K. Nakano, T. Uto, D. Adachi, M. Kanematsu, H. Uzu, *et al.* "Silicon heterojunction solar cell with interdigitated back contacts for a photoconversion efficiency over 26%". In: *Nature energy* 2.5 (2017), pp. 1–8.

[56] Longi. *At 26.81 %, LONGi sets a new world record efficiency for silicon solar cells*. 2022. URL: https://www.longi.com/en/news/propelling-the-transformation/ (visited on 02/01/2023).

[57] F. Haase, C. Hollemann, S. Schäfer, A. Merkle, M. Rienäcker, J. Krügener, R. Brendel, and R. Peibst. “Laser contact openings for local poly-Si-metal contacts enabling 26.1%-efficient POLO-IBC solar cells”. In: *Solar Energy Materials and Solar Cells* 186 (2018), pp. 184–193.

[58] C. Battaglia, X. Yin, M. Zheng, I. D. Sharp, T. Chen, S. McDonnell, A. Azcatl, C. Carraro, B. Ma, R. Maboudian, *et al.* “Hole selective MoO x contact for silicon solar cells”. In: *Nano letters* 14.2 (2014), pp. 967–971.

[59] C. Battaglia, S. M. De Nicolas, S. De Wolf, X. Yin, M. Zheng, C. Ballif, and A. Javey. “Silicon heterojunction solar cell with passivated hole selective MoOx contact”. In: *Applied Physics Letters* 104.11 (2014), p. 113902.

[60] J. Geissbühler, J. Werner, S. Martin de Nicolas, L. Barraud, A. Hessler-Wyser, M. Despeisse, S. Nicolay, A. Tomasi, B. Niesen, S. De Wolf, *et al.* “22.5% efficient silicon heterojunction solar cell with molybdenum oxide hole collector”. In: *Applied Physics Letters* 107.8 (2015), p. 081601.

[61] J. Dréon, Q. Jeangros, J. Cattin, J. Haschke, L. Antognini, C. Ballif, and M. Boccard. “23.5%-efficient silicon heterojunction silicon solar cell using molybdenum oxide as hole-selective contact”. In: *Nano Energy* 70 (2020), p. 104495.

[62] X. Yang, Q. Bi, H. Ali, K. Davis, W. V. Schoenfeld, and K. Weber. “High-performance TiO2-based electron-selective contacts for crystalline silicon solar cells”. In: *Advanced Materials* 28.28 (2016), pp. 5891–5897.

[63] S. Avasthi, W. E. McClain, G. Man, A. Kahn, J. Schwartz, and J. C. Sturm. “Hole-blocking titanium-oxide/silicon heterojunction and its application to photovoltaics”. In: *Applied Physics Letters* 102.20 (2013), p. 203901.

[64] JinkoSolar Holding Co. Ltd. *JinkoSolar’s High-efficiency N-Type Monocrystalline Silicon Solar Cell Sets New Record with Maximum Conversion Efficiency of 26.89%.* 2023. URL: https://ir.jinkosolar.com/news-releases/news-release-details/jinkosolars-high-efficiency-n-type-monocrystalline-silicon-3 (visited on 11/14/2023).

[65] J. Bullock, Y. Wan, Z. Xu, S. Essig, M. Hettick, H. Wang, W. Ji, M. Boccard, A. Cuevas, C. Ballif, *et al.* “Stable dopant-free asymmetric heterocontact silicon solar cells with efficiencies above 20%”. In: *ACS Energy Letters* 3.3 (2018), pp. 508–513.

[66] ITRPV. *International Technology Roadmap for Photovoltaic (ITRPV) 2022 Results.* 2023. URL: https://www.vdma.org/international-technology-roadmap-photovoltaic (visited on 07/25/2023).

[67] M. Hermle, F. Feldmann, M. Bivour, J. C. Goldschmidt, and S. W. Glunz. “Passivating contacts and tandem concepts: Approaches for the highest silicon-based solar cell efficiencies”. In: *Applied Physics Reviews* 7.2 (2020), p. 021305.

[68] L. Tutsch, F. Feldmann, M. Bivour, W. Wolke, M. Hermle, and J. Rentsch. “Integrating transparent conductive oxides to improve the infrared response of silicon solar cells with passivating rear contacts”. In: *AIP Conference Proceedings*. Vol. 1999. 1. AIP Publishing LLC. 2018, p. 040023.

[69] M. Wimmer, M. Bär, D. Gerlach, R. Wilks, S. Scherf, C. Lupulescu, F. Ruske, R. Félix, J. Hüpkes, G. Gavrila, *et al.* “Hard x-ray photoelectron spectroscopy study of the buried Si/ZnO thin-film solar cell interface: Direct evidence for the formation of Si–O at the expense of Zn-O bonds”. In: *Applied physics letters* 99.15 (2011), p. 152104.

[70] C. Messmer, M. Bivour, C. Luderer, L. Tutsch, J. Schön, and M. Hermle. “Influence of interfacial oxides at TCO/doped Si thin film contacts on the charge carrier transport of passivating contacts”. In: *IEEE Journal of Photovoltaics* 10.2 (2019), pp. 343–350.

[71] L. Neusel, M. Bivour, and M. Hermle. “Selectivity issues of MoOx based hole contacts”. In: *Energy Procedia* 124 (2017), pp. 425–434.

[72] M. T. S. K. A. Sen, P. Bronsveld, and A. Weeber. “Thermally stable MoOx hole selective contact with Al2O3 interlayer for industrial size silicon solar cells”. In: *Solar Energy Materials and Solar Cells* 230 (2021), p. 111139.

[73] M. T. S. K. Ah Sen, A. Mewe, J. Melskens, J. Bolding, M. van de Poll, and A. Weeber. “Soft deposition of TCOs by pulsed laser for high-quality ultra-thin poly-Si passivating contacts”. In: *Journal of Applied Physics* 134.15 (2023).

2

EXPERIMENTAL DETAILS & MODELLING APPROACH

2.1. SOLAR CELL FABRICATION

THe research of this thesis focuses on the surface passivating and hole carrier-selective properties of MoO_x contacts, low Pulsed Laser Deposition (PLD) induced damage on surface passivation of ultra-thin poly-Si contacts, and their integration in complete c-Si solar cells. To investigate in detail the hole contact properties of the MoO_x stack, the performance of the devices should not be limited by other layers. As a result, an electron poly-Si(n+)/SiO_x contact has been chosen as the rear contact because of its excellent surface passivation properties, low contact resistance, and stability under exposure to high thermal budget. The developed solar cell structure is referred as a "moly-poly" cell, and the main fabrication steps are shown in Figure 2.1. Solar cells are manufactured on 6-inch pseudo-square (156 x 156 mm^2) M2 n-type Czochralski (Cz) c-Si wafers with a resistivity of about 3-4 Ωcm. The substrates are textured in a KOH etching solution, followed by a pre-gettering step ($POCl_3$ diffusion in a Tempress tube furnace and phosphosilicate removal by HF), and subsequently subjected to a smoothing etch (consisting of a HNO_3 and HF solution) of the pyramids. Subsequently, the Si textured substrates are cleaned sequentially in a standard Radio Corporation of America (RCA) 1 and 2, and nitric acid oxidation of Si (NAOS) solutions. The samples are dipped in a 1% HF bath and rinsed before further processing. Next, the rear and front contact layers can be deposited on the Si substrate. Transparent conductive oxide (TCO) layers are required at both front and rear of the solar cell since it also acts as an anti-reflection coating (ARC) and provides lateral transport at the front contact, and improves the internal reflection at the rear side. A full Ag blanket electrode is deposited by sputtering while the front Ag metal grid is screen-printed. The next sections provide a detailed explanation of the front MoO_x and rear poly-Si contacts fabrication.

2.1.1. POLY-SI CONTACT PROCESSING

Figure 2.2 shows the main fabrication steps of our electron poly-Si(n+) contact. Prior to the interlayer formation, the Si substrate is dipped in a 1% diluted HF bath to remove any native oxide present at the Si surface. Subsequently, a tunneling SiO_x film (~1.3 nm) is thermally grown at 610 °C in a low pressure chemical vapor deposition (LPCVD) reactor from Tempress. Next, a 20 nm phosphorus in-situ doped amorphous silicon (a-Si:H(n+)) layer is deposited on the rear side of the c-Si substrate by plasma enhanced chemical vapor deposition (PECVD), which is consequently crystallized in an N_2 environment at 900 °C. Finally, the contact is hydrogenated either by a PECVD NH_3 plasma at 375 °C or by a sacrificial spatial atomic layer deposition (sALD from Levitech) Al_2O_3 layer – after a post-deposition anneal (PDA) at 600 °C. The Al_2O_3 layer is subsequently etched off in a 1% diluted HF solution.

2.1.2. MoO_X FRONT CONTACT PROCESSING

Figure 2.3 shows the main fabrication steps of the front hole MoO_x contact. Similar to the rear contact formation, the half fabricates are dipped in a 1% HF solution and rinsed before the deposition of the passivating interlayer. Interlayers based

on intrinsic a-Si:H and Al_2O_3 are deposited by PECVD and sALD, respectively. The fabrication of the interlayers is described in detail in the respective chapters. Subsequently, a thin layer of MoO_x is deposited at high vacuum (~$7x10^{-6}$ mbar) in an electron beam physical vapor deposition (PVD) tool without any subsequent thermal treatment. Next, a TCO layer is deposited on top of the MoO_x layer to form the front hole contact. Note that it is essential that the MoO_x layer is capped shortly after deposition to reduce air exposure which is known to degrade the work function (WF) properties of the MoO_x contact [1]. Additionally, MoO_x and TCO layers deposited by PLD technique (developed by Solmates B.V.) are investigated in this work. The fundamental principles of PLD are explained in the following section.

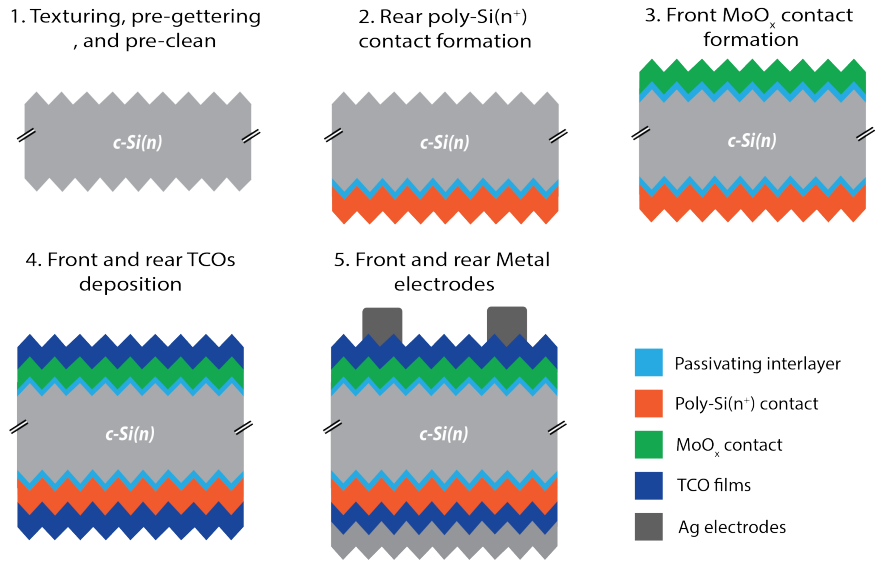

Figure 2.1.: Schematic of main processing steps for the manufacturing of moly-poly cells. Note that the front electrode was screen-printed while the full Ag rear electrode was sputtered.

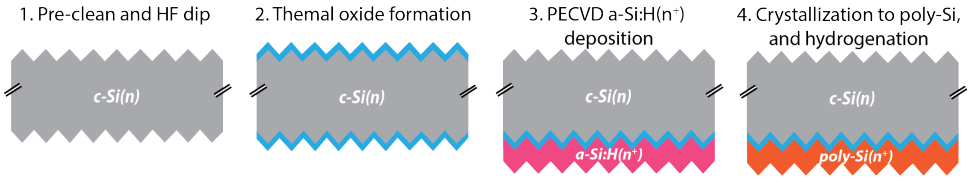

Figure 2.2.: Main fabrication steps of the rear poly-Si(n+) contact.

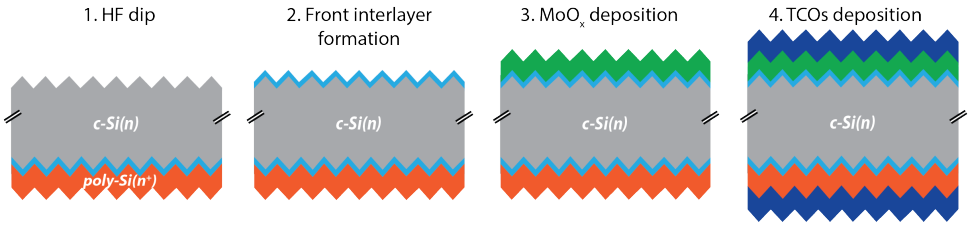

Figure 2.3.: Main fabrication steps of the front MoO_x contact.

2.1.3. PULSED LASER DEPOSITION TECHNIQUE

PLD is a PVD technique that shares process characteristics with molecular beam epitaxy and some with sputtering techniques. In PLD, a high intensity pulsed laser is utilized as an energy source, and is directed towards a target material. As a result, the material is vaporized, and subsequently is deposited on a substrate. PLD was re-developed in the late 1980s and popularized as a successful growing technique for in-situ growth of high-temperature superconducting films due to its excellent stoichiometric tuning [2]. After several decades of significant development, PLD is widely employed in both academic research and industrial applications to grow films used in various fields, including insulators [3], semiconductors [4–6], polymers [7–9], metals [10], and organics materials [11]. PLD has several unique characteristics that have shown to be beneficial for complex oxide thin-film growth. Several unique features of PLD include complex stoichiometry control, generation of energetic species, and vast range of operating pressure from ultrahigh vacuum to several millibars [12].

The principle of PLD processes is relatively simple, as illustrated in Figure 2.4. A high energy density ultraviolet (UV) laser with a narrow wavelength bandwidth is directed towards a target material by utilizing several precisely aligned mirrors. The target which is situated in a vacuum chamber is repeatedly ablated by the focused UV laser with pulses of few nanoseconds duration. Note that, in our PLD system, targets can be exchanged without breaking vacuum. The target stage can be either rotated or scanned which allows for uniform material ablation across the target. This is because the laser spot size is only few cm^2 big. Through decomposition of the material, the target material is vaporized, and subsequently forms a plasma plume which expands perpendicularly from the target surface. The PLD chamber can be operated in high vacuum or in the presence of background gas(es). The presence of background gas(es) interacts with the ablated target material and can be used to tune the properties of the deposited material. Similarly to the target stage, the substrate stage is either rotated or scanned to allow uniform layer growth. While PLD processes are rather simple, the material ablation is quite complex. For clarity, the main PLD processes can be summarized in 4 main stages (illustrated in Figure 2.4):

1. Absorption of laser light and ablation of material,

2. Creation of a plasma plume,

3. Expansion of plume into vacuum or background gas,

4. Deposition of ablated species on a substrate and nucleation and growth of the film.

During the first stage, the laser light is absorbed by the target material and results in the explosive removal of ions, electrons, and neutral atoms [13]. The ablation of materials upon laser absorption is mainly dependent on laser fluency, absorption, laser light reflection, and cohesive energy [10]. The cohesive energy is the energy required to release an atom from a solid and varies from material to material. In stage 2, a plasma plume is created due to the ablation of partly ionized particles after a laser pulse. At this point, the pressure of the plume (5-10 bars) drives the free expansion of the ablated atoms into vacuum or the background gas [14]. The expansion eventually reaches a constant velocity in vacuum while the plume is slowed down by the background gas. The introduction of a background gas during a PLD process serves two purposes. Firstly, the background gas and the plasma plume interacts and subsequently results in the formation of various material phases [12]. Typically, background gases, such as O_2 and N_2 are used for oxides and nitrides thin films growth, respectively, and allows for excellent layer composition tunability. Additionally, background gases can be used to reduce the kinetic energy of the ablated species. This allows for the thermalization of the energetic species which results in a "soft landing" of species on the substrate [15].

The PLD system, developed by Solmates BV, consists of a KrF excimer laser that generates ultra-short laser pulses with a wavelength of 248 nm, directing them towards the target. Additionally, the system includes a loadlock capable of accommodating 25 industrial-size wafers and supporting up to 4 different target materials, facilitating in-situ large-area deposition of various layer stacks. Various deposition parameters can be varied allowing for controlled tuning of various films. Table 2.1 shows the variability of the system parameters. The following sections summarize some important deposition parameters:

- LASER FLUENCE AND REPETITION RATE

  The laser fluency and repetition rate are important parameters of the pulsed excimer laser which control the number of particles arriving at the surface of the sample. The repetition rate is defined by the frequency of pulses created by the excimer laser and can influence the deposited film composition. For instance, high repetition rate has shown to result in Ru deficiencies in $SrRuO_3$ thin films which is caused by an increase in the adatom interaction [16]. Laser fluency is defined as the laser energy of a pulse per unit area, and is commonly expressed as Joule per cm^2. Laser fluency has a strong influence on the ablation rate, and therefore deposition rate. At high fluence, the ablated particles have large kinetic energy which results in a sputter-like deposition. The sputtering effect can be destructive for multicomponent film. For instance, Van de Reit el al.[17] showed that Ga-atoms are depleted in a FeSiGaRu thin film due to the high component volatility. On the other hand, low fluence leads to preferential evaporation of the most volatile components [12].

Table 2.1.: Minimum and maximum limits of the PLD parameters.

PLD parameter	Min - Max
Repetition rate [Hz]	5 -100
Laser fluency [J/cm^2]	0.93 - 1.55
Chamber pressure [mbar]	0.005 - 0.5
Substrate temperature [°C]	25 - 600

- COMPOSITION AND PRESSURE OF BACKGROUND GAS

  Background gases such as, N_2, O_2, and Ar can be introduced in the PLD chamber during deposition to alter the composition, thickness, and crystallinity of films [13]. For instance, N_2 and O_2 can be used to adjust the stoichiometry of the nitride and oxide layers, respectively. The background gas pressure is arguably the most important parameter to control the kinetic energies of species arriving at the substrate [18]. Note that the free mean path of particles can be controlled by varying the chamber pressure, distance between the target and substrate, and by the laser energy.

- DEPOSITION TEMPERATURE

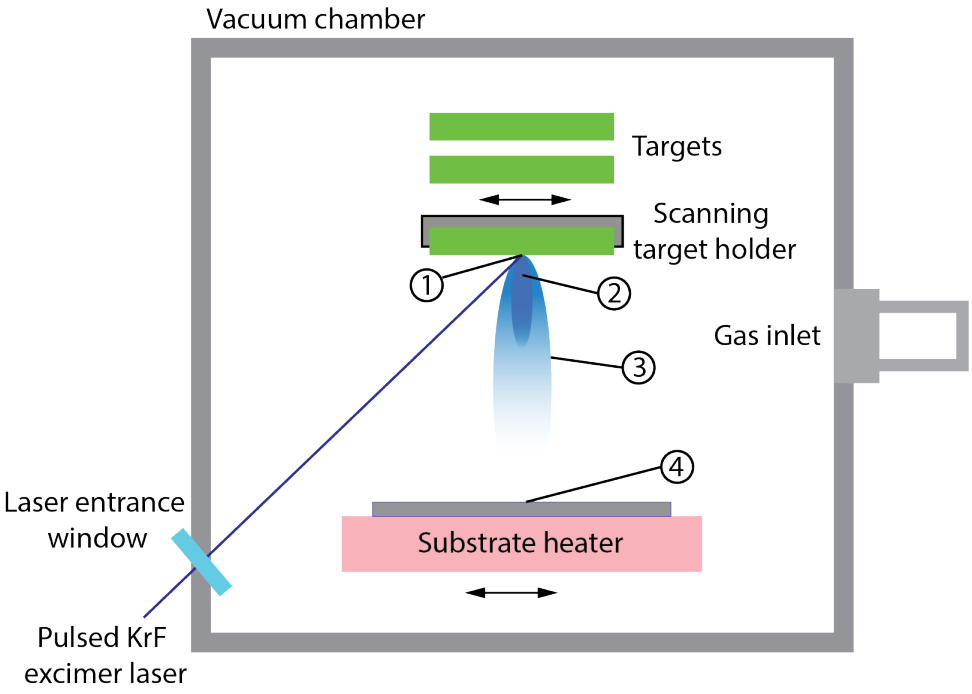

Figure 2.4.: A schematic of a typical PLD system. The main PLD stages are noted from 1 to 4.

The substrate temperature plays a significant role in the growth properties of the layer. For instance, the crystallinity of TCOs can be tuned by the deposition temperature by which high temperature facilitates the formation of a polycrystalline layer while low deposition temperature results in the formation of an amorphous layer.

2.2. CHARACTERIZATION TECHNIQUES

2.2.1. LAYER CHARACTERIZATION

OPTO-ELECTRICAL PROPERTIES

In this thesis, layer thickness, refractive index (n), and absorption coefficient (k) were determined by a spectroscopic ellipsometry (SE) setup (J.A Woollam Co., Inc.). SE is a non-destructive optical technique used to measure the optical properties of a layer. Figure 2.5 illustrates the basic principles of SE. SE is based on reflection of incident polarized light on samples, and can be expressed as $p-$ (parallel to the incident plane) and $s-$ polarizations (perpendicular). Upon reflection, the sample induces a phase shift (Δ) of the $p-$ and $s-$ components and this phase shift depends on the optical constant (n & k) of the sample, and on the layer thickness [4–7]. In Figure 2.5, the reflected $p-$ and $s-$ components are no longer consistent and are prompted to rotation as the reflected light propagates. As a result, reflected electric field vectors ($E_{f,rs}$, $E_{f,rp}$) becomes elliptical – hence the name of the technique "ellipsometry". The amplitude ratio (ψ) and Δ between the $p-$ and $s-$ polarizations are measured by the ellipsometry which correlates with the n & k of the sample, respectively. The author recommends for book from Fujiwara and Collins [19] for an extensive understanding of spectroscopic ellipsometry.

Films were deposited on a one-sided mechanically mirror polished c-Si substrate. The rear side was left unpolished to avoid backside reflections during measurement. Measurements were carried at 3 different incidence angles (60°, 70°, and 80°) and for photon energies ranging between 1.1 to 5 eV. Subsequently, models based on several oscillators were developed and fitted to account for different absorption across the photon energies. Further details about the different oscillators used to characterize the layers can be found in the experimental section.

2.2.2. SURFACE PASSIVATION & CONTACT SELECTIVITY

In order to understand and further optimize our newly developed layers, it is paramount to characterize the surface passivation properties and carrier selectivity of the deposited layers. In the moly-poly cell, the developed interlayer for the hole contact is required to provide sufficient chemical passivation to reduce the dangling bonds present at the Si surface, and the MoO_x layer should induced a strong upward banding for good carrier-selectivity while inducing a field-like effect passivation. Furthermore, ITO deposition on top of the MoO_x often degrades on the surface passivation of the contact due to sputtered-induced damage. The impact of these additional process steps and potential post-treatments (such as annealing) on the surface passivation quality has to be investigated for further optimization. To

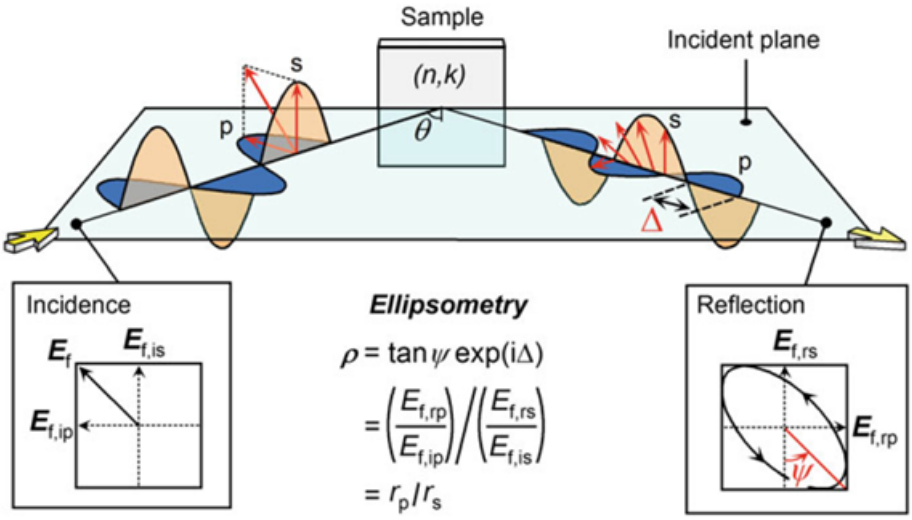

Figure 2.5.: Schematic of the basic principle of SE. Figure taken from [19].

investigate the influence of depositing a single additional layer or combined layers stack, symmetric half-fabricates are manufactured to monitor the surface passivation properties.

The surface passivation is determined by the Sinton WCT-120 carrier lifetime tester. Figure 2.6 shows the schematic of the lifetime tester and highlights the principle of this measurement. The reader can find further description in [20]. A sample is placed under a short decaying flashlight and the photoconductance of the sample is measured by the coil underneath. As a result, the lifetime of the sample as a function of carrier injection level can be obtained. Effective lifetime (τ_{eff}) was measured at injection level of 1x10^{15} cm^{-3}. In addition, the implied open-circuit voltage (iV_{oc}) can be calculated at 1 sun. In our case, 5 consecutive flashes are applied on the sample which results in an average lifetime measurement. Furthermore, the lifetime is measured on different 5 locations across the sample. Transient or quasi-steady state photoconductance (QSSPC) modes are used according to the τ_{eff} of the sample; for τ_{eff} above 200 μs transitent mode is used.

Metal oxide contacts, such as MoO_x often suffer from carrier-selectivity issues which impede its implementation in Si solar cells. The carrier-selectivity of the contact issues are often only detected after a current-voltage (IV) measurement, as an S-shaped IV curve. This requires metallization of the cell and often a post-annealing treatment to achieve good contact. An alternative method to detect the carrier-selectivity losses of a contact can be achieved by measuring the difference between the iV_{oc} and external V_{oc} ($\Delta V_{\text{oc}} = iV_{\text{oc}} - V_{\text{oc}}$). The ΔV_{oc} can be used as a figure of merit to quantify the carrier-selectivity loss [22, 23]. In this case, the external V_{oc} is measured by the $SunsV_{\text{oc}}$ method. The $SunsV_{\text{oc}}$ method was developed by Sinton and Cuevas [24] and offers a pseudo IV characteristic of the

solar cell, as if no series resistance is presented. The V_{oc} of the solar cell is measured at 1 sun. The measurement sample used to determine ΔV_{oc} is shown in Figure 2.7. This method is appealing since it can be performed on unmetallized half-fabricates as long as the both contacts consist of a TCO layer. This is because TCO layers are often conductive enough to enable for $SunsV_{oc}$ measurement. As a result, carrier-selectivity loss of the contact can be determined without metallization and prior to the effect of a post-annealing treatment.

2.2.3. CONTACT RESISTIVITY

Contact resistivities (ρ_c) for various stacks are important parameters for passivating contacts developed in the thesis. Dark vertical JV measurements were used on symmetric samples where the current density across a specified area is defined. Several resistance contributions in bulk and at interfaces need to be known. The details of contact test structures can be found in experimental details of the respective chapters.

2.2.4. SOLAR CELL CHARACTERIZATION

The electrical performance of solar cells is determined by using an AAA Wacom solar simulator which simulates an AM1.5G spectrum at standard test conditions (STC, 25 °C, Air Mass 1.5 global spectrum and 1000 W/m^2 as input irradiance). The light intensity is calibrated for each set of measurements by using a reference solar cell with known electrical characteristics. The rear side solar cell is placed on a metal alloy chuck while front side metal grid electrode is connected with a metal pin probe. Under illumination, the electrical characteristics of the solar cell i.e. V_{oc},

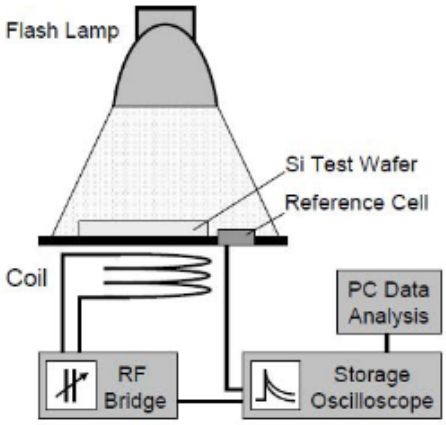

Figure 2.6.: Schematic illustrating the main components of a Sinton lifetime tester.Figure taken from [21].

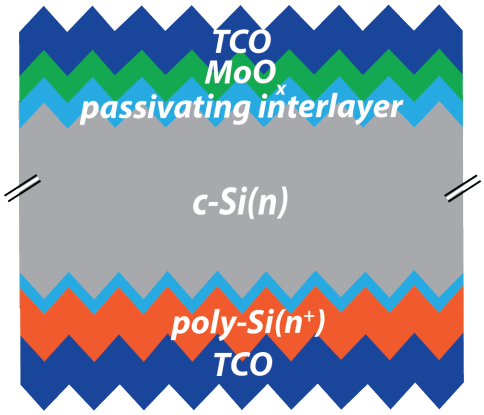

Figure 2.7.: Measurement sample to determine the iV_{oc}, $SunsV_{oc}$ and hence the ΔV_{oc} of the solar cell.

short-circuit current (J_{sc}), fill factor (FF), and efficiency (η) are measured. The η is calculated by the following equation:

$$\eta = \frac{J_{sc}.V_{oc}.FF}{P_{in}} \tag{2.1}$$

where P_{in} is the power input.

The J_{sc} defines the integrated generation and recombination current of a solar cell but it does not give any information about the wavelength dependence. Alternatively, the spectral response (SR) of the solar cell can be used to define the charge extraction across the sunlight spectrum. Figure 2.8 shows the schematic of a typical SR setup. The SR tool consists of a light source and a chopper wheel that intermittently interrupts the photon flux. Subsequently, monochromator filers are used at TNO that selectively allows photons within a specific, narrow wavelength range to pass through. This filtered light is then used to illuminate both a reference cell (for which the SR is already known) and the solar cell that is being investigated. Due to the periodic on-off pattern of light generated by the chopper wheel, the use of lock-in amplifiers becomes necessary for signal detection and analysis. SR of the cell can be measured as a function of wavelength and subsequently the external quantum efficiency (EQE) can be calculated. EQE gives information about the percentage of collected carrier generation by the incident light. By determining the amount of light that has been reflected or transmitted from the solar cell, the so-called internal quantum efficiency (IQE) can be calculated from the reflectance (R(λ)):

$$IQE(\lambda) = \frac{EQE(\lambda)}{1 - R(\lambda)} \tag{2.2}$$

2.2.5. MODELLING APPROACH

In this section, we elaborate on the modelling approach used this work to further understand the carrier-selectivity performance of various solar cells. The simulations are performed with ATLAS software tool with was developed by Silvaco International.

ATLAS can be used to predict the electrical performance of a solar cell by simulating the transport of carriers through a two dimensional grid. The numerical simulation mainly consists of the solar cell structure creation, and selecting the numerical simulation of the contacts and material properties [25]. The former consists by defining the parameter of the various contacts and subsequently generating a mesh which encompass the different materials and regions of the solar cell. Typically, the mesh need to be made finer near the regions of interests. Subsequently, the materials properties are defined, such as bandgap, work function, band misalignments, electron affinity, and electron and hole mobilities of the material. To accurately define the carrier transport and carrier generation/recombination of the solar cell, suitable physical models have to be chosen. Once the parameters and physical models have been set, numerical models have to be chosen to allow for converting solutions of the solar cell device problems.

Subsequently, the electrical characteristics of the modelled solar cell can be extracted. The simulation software is explained in further details in [26].

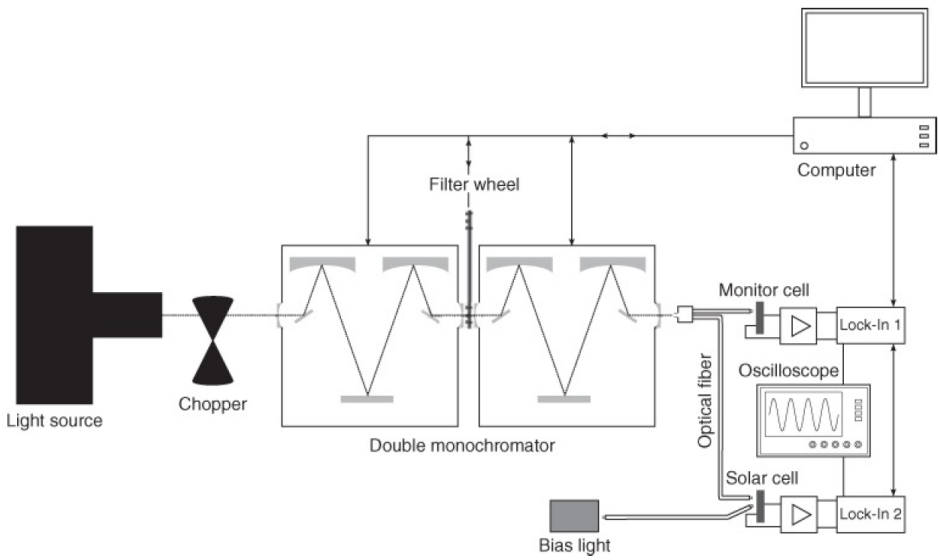

Figure 2.8.: Schematic of the spectral response setup used to characterize the EQE of the solar cells. Figure taken from [20].

REFERENCES

[1] M. Vasilopoulou, A. M. Douvas, D. G. Georgiadou, L. C. Palilis, S. Kennou, L. Sygellou, A. Soultati, I. Kostis, G. Papadimitropoulos, D. Davazoglou, *et al.* "The influence of hydrogenation and oxygen vacancies on molybdenum oxides work function and gap states for application in organic optoelectronics". In: *Journal of the American Chemical Society* 134.39 (2012), pp. 16178–16187.

[2] A. Inam, M. Hegde, X. Wu, T. Venkatesan, P. England, P. Miceli, E. Chase, C. Chang, J. Tarascon, and J. Wachtman. "As-deposited high T c and J c superconducting thin films made at low temperatures". In: *Applied physics letters* 53.10 (1988), pp. 908–910.

[3] J. M. Warrender and M. J. Aziz. "Kinetic energy effects on morphology evolution during pulsed laser deposition of metal-on-insulator films". In: *Physical Review B* 75.8 (2007), p. 085433.

[4] V. Rawat and T. Sands. "Growth of Ti N/ Ga N metal/semiconductor multilayers by reactive pulsed laser deposition". In: *Journal of Applied Physics* 100.6 (2006), p. 064901.

[5] F. Dumas-Bouchiat, C. Champeaux, A. Catherinot, A. Crunteanu, and P. Blondy. "RF-microwave switches based on reversible semiconductor-metal transition of VO 2 thin films synthesized by pulsed-laser deposition". In: *Applied Physics Letters* 91.22 (2007), p. 223505.

[6] W. Shen and H. Kwok. "Crystalline phases of II-VI compound semiconductors grown by pulsed laser deposition". In: *Applied physics letters* 65.17 (1994), pp. 2162–2164.

[7] D. M. Bubb, J. Horwitz, J. Callahan, R. McGill, E. Houser, D. Chrisey, M. Papantonakis, R. Haglund Jr, M. Galicia, and A. Vertes. "Resonant infrared pulsed-laser deposition of polymer films using a free-electron laser". In: *Journal of Vacuum Science & Technology A: Vacuum, Surfaces, and Films* 19.5 (2001), pp. 2698–2702.

[8] A. Mercado, C. Allmond, J. Hoekstra, and J. Fitz-Gerald. "Pulsed laser deposition vs. matrix assisted pulsed laser evaporation for growth of biodegradable polymer thin films". In: *Applied Physics A* 81 (2005), pp. 591–599.

[9] H.-U. Krebs, M. Weisheit, J. Faupel, E. Süske, T. Scharf, C. Fuhse, M. Störmer, K. Sturm, M. Seibt, H. Kijewski, *et al.* "Pulsed laser deposition (PLD)–a versatile thin film technique". In: *Advances in solid state physics* (2003), pp. 505–518.

[10] J. Gonzalo, Á. Perea, D. Babonneau, C. N. Afonso, N. Beer, J. Barnes, A. K. Petford-Long, D. Hole, and P. D. Townsend. "Competing processes during the production of metal nanoparticles by pulsed laser deposition". In: (2005).

[11] H. Kim, J. Horwitz, G. Kushto, Z. Kafafi, and D. Chrisey. “Indium tin oxide thin films grown on flexible plastic substrates by pulsed-laser deposition for organic light-emitting diodes”. In: *Applied physics letters* 79.3 (2001), pp. 284–286.

[12] R. Eason. *Pulsed laser deposition of thin films: applications-led growth of functional materials*. John Wiley & Sons, 2007.

[13] J. Schou. “Physical aspects of the pulsed laser deposition technique: The stoichiometric transfer of material from target to film”. In: *Applied Surface Science* 255.10 (2009), pp. 5191–5198.

[14] A. K. Vaseashta and I. N. Mihailescu. *Functionalized nanoscale materials, devices and systems*. Springer Science & Business Media, 2008.

[15] Y. Smirnov, L. Schmengler, R. Kuik, P.-A. Repecaud, M. Najafi, D. Zhang, M. Theelen, E. Aydin, S. Veenstra, S. De Wolf, *et al.* “Scalable pulsed laser deposition of transparent rear electrode for perovskite solar cells”. In: *Advanced Materials Technologies* 6.2 (2021), p. 2000856.

[16] H. Schraknepper, C. Bäumer, F. Gunkel, R. Dittmann, and R. De Souza. “Pulsed laser deposition of SrRuO3 thin-films: The role of the pulse repetition rate”. In: *APL materials* 4.12 (2016).

[17] E. Van de Riet, J. Kools, and J. Dieleman. “Incongruent transfer in laser deposition of FeSiGaRu thin films”. In: *Journal of applied physics* 73.12 (1993), pp. 8290–8296.

[18] A. Ojeda-G-P, M. Döbeli, and T. Lippert. “Influence of plume properties on thin film composition in pulsed laser deposition”. In: *Advanced Materials Interfaces* 5.18 (2018), p. 1701062.

[19] H. Fujiwara and R. W. Collins. *Spectroscopic ellipsometry for photovoltaics*. Vol. 1. Springer, 2018.

[20] P. Würfel and U. Würfel. *Physics of solar cells: from basic principles to advanced concepts*. John Wiley & Sons, 2016.

[21] S. Rein. *Lifetime spectroscopy: a method of defect characterization in silicon for photovoltaic applications*. Vol. 85. Springer Science & Business Media, 2005.

[22] M. Bivour, S. Schröer, and M. Hermle. “Numerical analysis of electrical TCO/a-Si: H (p) contact properties for silicon heterojunction solar cells”. In: *Energy Procedia* 38 (2013), pp. 658–669.

[23] M. Bivour, J. Temmler, F. Zähringer, S. Glunz, and M. Hermle. “High work function metal oxides for the hole contact of silicon solar cells”. In: *2016 IEEE 43rd Photovoltaic Specialists Conference (PVSC)*. IEEE. 2016, pp. 0215–0220.

[24] M. J. Kerr, A. Cuevas, and R. A. Sinton. “Generalized analysis of quasi-steady-state and transient decay open circuit voltage measurements”. In: *Journal of applied physics* 91.1 (2002), pp. 399–404.

[25] A. U. M. A. Device. “ATLAS User’s Manual, A Device Simulation Software Package”. In: *Santa Clara, CA, USA* (2015).

[26] S. Michael, A. Bates, and M. Green. “Silvaco ATLAS as a solar cell modeling tool”. In: *Conference Record of the Thirty-first IEEE Photovoltaic Specialists Conference, 2005*. IEEE. 2005, pp. 719–721.

3

THERMALLY STABLE MoO_X HOLE SELECTIVE CONTACT WITH Al_2O_3 INTERLAYER FOR INDUSTRIAL SIZE C-SI SOLAR CELLS

In general, intrinsic hydrogenated amorphous silicon (a-Si:H(i)) has been used below MoO_x to form a good contact. An a-Si:H(i)/MoO_x stack gives good surface passivation, but can result in poor carrier selectivity after exposure to slightly elevated temperatures. For this reason, we investigated an alternative interface layer, a very thin Al_2O_3 tunneling layer (< 2 nm), deposited by atomic layer deposition (ALD), that can provide surface passivation, higher transparency and thermal stability without affecting the hole transport properties across the contact. To demonstrate this passivating contact structure a 6" moly-poly cell, with an Al_2O_3/MoO_x stack at the front side and n-type doped polysilicon at the rear side, was made using a high-throughput spatial ALD tool, and e-beam PVD, for the Al_2O_3 and MoO_x layers, respectively. This resulted in an efficiency of 18.2% with a V_{oc} of 651 mV, a FF of 75.6% and a J_{sc} of 36.9 mA/cm^2. A post-deposition anneal (PDA) of the thin Al_2O_3 interlayer has significant effect on the Al_2O_3 thickness, layer stoichiometry, contact selectivity, and sputtering-induced damage. Annealing at higher T_{PDA} (350-600 °C) results in ineffective hole carrier transport and makes the stack more sensitive to ITO damage. The best performing device was, therefore, made using an Al_2O_3 layer without a PDA treatment. Moreover, we found that this solar cell structure is thermally stable up to at least 210 °C , and even slightly improves under annealing which makes this device industrially appealing.

This chapter is based on an article published by M. T. S. K. A. Sen, P. Bronsveld, and A. Weeber. "Thermally stable MoO_X hole selective contact with Al_2O_3 interlayer for industrial size silicon solar cells" in Solar Energy Materials and Solar Cells Journal **230**, 111139 (2021), doi:10.1016/j.solmat.2021.111139 [1].

3.1. INTRODUCTION

To achieve high conversion efficiencies, it is required to minimize the charge carrier recombination at the metal/Si interface in c-Si solar cells. This carrier recombination can be avoided by inserting thin functional layers in between the metal contacts and the Si absorber. These thin films need to combine two important functionalities: they need to both passivate the defects at the Si surface, and allow the collection for one type of charge carrier. For instance, silicon heterojunction (SHJ) and doped polycrystalline Si (poly-Si) technologies are prime examples of passivating and carrier-selective contacts that fulfill the aforementioned requirements. Nevertheless, these passivating and carrier-selective contacts present one major drawback: they absorb light in the same range as the Si absorber and are therefore a source of parasitic absorption losses, when placed at the front side of the solar cell. As a result, this has prompted for the exploration of alternative transparent carrier-selective contacts, such as nanocrystalline and/or alloyed Si based structures [2–4], and transition metal oxides (TMOs) [5–7].

Among these TMO contacts, molybdenum oxide (MoO_x) has demonstrated to have some advantages as a hole-selective contact in comparison to doped Si-based contacts. MoO_x is a wide bandgap (~3 eV) material, and has a high work function (WF), which induces upward band bending of the conduction band when contacted to Si. However, MoO_x does not provide sufficient chemical surface passivation when contacted to silicon. For this reason a passivating interlayer, commonly, intrinsic hydrogenated amorphous Si (a-Si:H(i)) is utilized. By using this scheme, a solar cell with a front ITO/MoO_x/a-Si:H(i)/c-Si contact has recently been demonstrated to achieve a conversion efficiency of 23.83 % during the writing of this thesis [8]. Nevertheless, this solar cell structure often results in the appearance of an S-shaped current-voltage (IV) curve when annealed at standard SHJ curing temperatures. This S-shaped IV curve is commonly attributed to the induced band bending loss inside the c-Si absorber, which reduces the concentration of holes near the contact and therewith the selective properties; the asymmetric concentration of carriers, that is required to maintain a selective contact, is then lost [9]. Although the origin of the induced band bending loss is still under debate [10, 11], it seems likely that the presence of the a-Si:H(i) interlayer influences the contact selectivity. For this reason, we have explored alternative interlayers for this contact, like an ultra-thin Al_2O_3 interlayer.

The excellent Si surface passivation properties, combined with a controllable thickness and excellent surface conformity, makes ultra-thin Al_2O_3 films, grown by atomic layer deposition (ALD), a promising tunneling interlayer for hole contacts. Its outstanding Si surface passivation arises from a combination of good chemical and field effect passivation properties; the chemical passivation originates from a thin hydrogenated SiO_2 interlayer while the field effect passivation is the result of a high, negative fixed charge density (Q_f), which is located within ~1 nm from the Si interface. A post-deposition anneal (PDA) treatment is often essential to achieve high level of surface passivation by allowing structural rearrangements at the interface [11, 12]. Additionally, ultra-thin ALD Al_2O_3 films show good recombination current density (J_0) and contact resistivity (ρ_c) properties when utilized as an interlayer for

hole selective contacts [13–15]. However, the implementation of the Al_2O_3 interlayer in combination with a hole selective MoO_x contact has not yet been established before this study on a completed solar cell.

In this work, we explored the possible application of an ultra-thin Al_2O_3 interlayer in a MoO_x-based hole-selective contact. More specific, we investigated the effect of PDA temperature (T_{PDA}) on the structural and electrical properties of an ultra-thin Al_2O_3 interlayer, and its influence on the surface passivation and carrier selectivity of a MoO_x contact in completed solar cells.

3.2. EXPERIMENTAL DETAILS

The solar cell structure in which the Al_2O_3 interlayers (referred as moly-poly cells) are investigated, consists of a rear ITO/poly-Si(n+)/SiO_2 contact and a front Al_2O_3/MoO_x/ITO contact. The Poly-Si/SiO_2 contact is chosen for its good passivating properties, low contact resistance, and stability under exposure to temperatures elevating 200 °C. The "moly-poly" solar cell process flow is shown in Figure 3.1.

6-inch pseudo-square (156 x 156 mm^2) n-type Cz c-Si wafers with a resistivity of about 3 Ωcm are selected, and textured in a KOH etching solution, followed by a

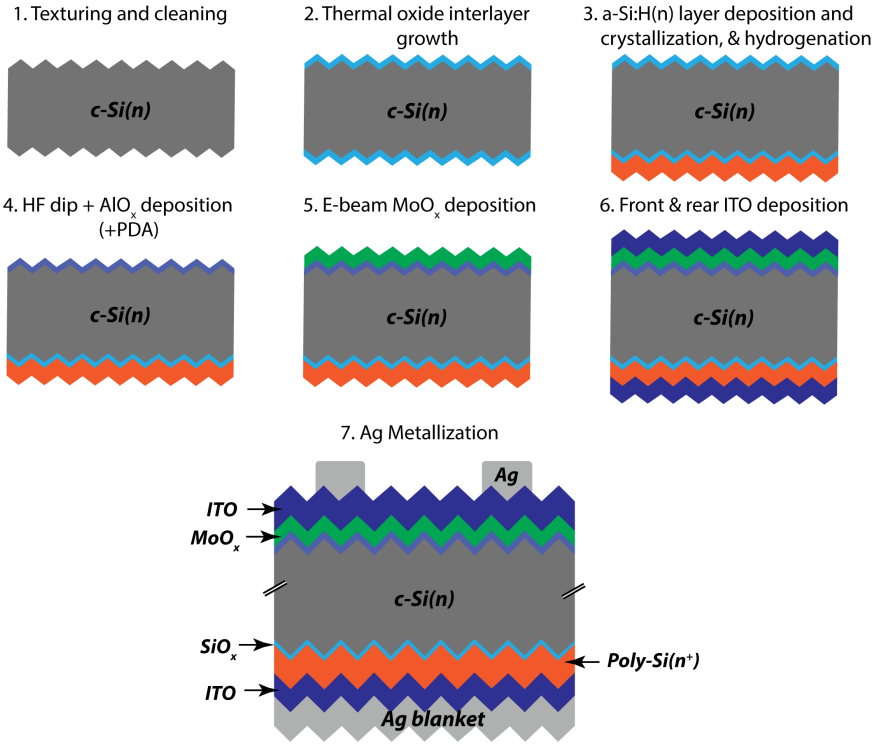

Figure 3.1.: Schematic representation of our process flow for the "moly-poly" solar cells consisting of a rear Poly(n+)/SiO_2 and a front Al_2O_3/MoO_x contact.

pre-gettering step ($POCl_3$ diffusion and phosphosilicate removal), and subsequently subjected to a smoothing etch. The wafers are sequentially cleaned in an RCA 1 and 2, and NAOS solutions. The samples are dipped in a 1% HF bath before further processing. Firstly, a tunneling SiO_x film (~ 1.3 nm) is thermally grown at 610 °C in a low pressure chemical vapor deposition (LPCVD) reactor. Subsequently, a 20 nm phosphorus doped amorphous silicon (a-Si:H(n+)) is deposited on the rear side of the samples by plasma enhanced chemical vapor deposition (PECVD), and consequently is crystallized in an N_2 environment at 900 °C. A PECVD NH_3 plasma at 375 °C is used to hydrogenate this newly formed poly-Si(n+) rear side contact.

Next, the samples are dipped in a 1% diluted HF bath to remove the front thermal SiO_x layer, and subsequently 8 cycles of spatial ALD Al_2O_3 interlayer is deposited using the Levitrack system from Levitech. On top of the Al_2O_3 film, a 5 nm MoO_x thin film is deposited at high vacuum ($7x10^{-6}$ mbar) in an electron beam physical vapor deposition (PVD) tool without any subsequent thermal treatment. The deposition rate of MoO_x is ranged between 0.3 to 0.5 nm/s. Finally, the device was capped, on both sides, with an ITO film in a PVD sputtering tool. The rear side Ag contact is also deposited by sputtering without air break directly afterwards. The front Ag grid is screen printed using a low temperature Ag paste, and finally, the device was annealed in air for curing the metal print.

The injection dependent minority carrier lifetime of the samples is evaluated by transient photoconductance measurements using a Sinton WCT-120. The *IV* measurements of the solar cells are performed under Standard Test Conditions in a Wacom AAA solar simulator and are corrected for spectral mismatch. The spectral response is measured over the full area of the device and at different wavelengths by using a filter wheel and with application of bias light. The reflection of the cells is also measured in order to determine the internal quantum efficiency (IQE). To study the absorption properties of the different films, a PerkinElmer Lambda 950/1050 spectrophotometer is utilized at 300 – 1200 nm wavelength range. X-ray photoelectron spectroscopy (XPS) is performed on the oxide layers using a Thermo Scientific KA1066 spectrometer using monochromatic Al Kα X-rays source. 8 cycles of spatial ALD Al_2O_3 layers were deposited on mechanically polished Si wafers to accurately determine the optical properties using spectroscopic ellipsometry measurements (SE, JA Woollam).

3.3. RESULTS

3.3.1. INFLUENCE OF THERMAL TREATMENTS ON THE AL_2O_3 STRUCTURAL PROPERTIES

Firstly, we investigate the influence of the T_{PDA} on the thickness of spatial ALD Al_2O_3 film. The thermal treatment is performed in an N_2 environment and is varied between 250 to 600 °C using separate samples for each temperature setting. The effect of T_{PDA} on the layer thickness is shown in Figure 3.2. Note that, the ellipsometry model that is used to measure interlayer thickness, accounts for the interfacial SiO_y layer – which is typically present at the surface of Si - and the subsequent formation of the Al_2O_3 film. For simplicity, the deposited

Al_2O_3/SiO_x stack is referred as the ALD Al_2O_3 interlayer, unless stated otherwise. The as-deposited layer results in an average thickness of ~ 1.43 nm and is not prompted to major change after a thermal treatment is performed at T_{PDA} = 250 °C. On the contrary, a substantial increase in layer thickness of about 0.6 nm is observed, when the Al_2O_3 layer is annealed at 350 °C. A further increase in thermal budget causes an observable increase in layer thickness, suggesting that the growth process of the interlayer is not saturated yet.

Further insight on changes in the elemental composition and chemical bonds during annealing of the Al_2O_3 interlayer can be obtained by performing XPS measurements. Figure 3.3(a) shows the relative intensity of the different components of the Si 2p spectra where the Si substrate and suboxides are denoted as Si^0 and Si^{x+} (x=1,..,4), respectively. The change in Si 2p spectra of the annealed for ultra-thin Al_2O_3 samples (200 - 450 °C) are depicted in Figure 3.3(b). A general decrease of the Si peak is observed with increasing T_{PDA} while an increase in Si oxide peak is measured at higher binding energy. The appearance of Si oxide peak upon anneal can be mainly attributed to the formation of Si^{+3} and Si^{+4} oxidation states. Nevertheless, it can be noted that samples annealed at T < 250 °C show no distinct Si oxide peak. In contrast, the Si oxide peak increases at annealing temperature above 300 °C indicating an enhanced Si-O coordination during the PDA treatment.

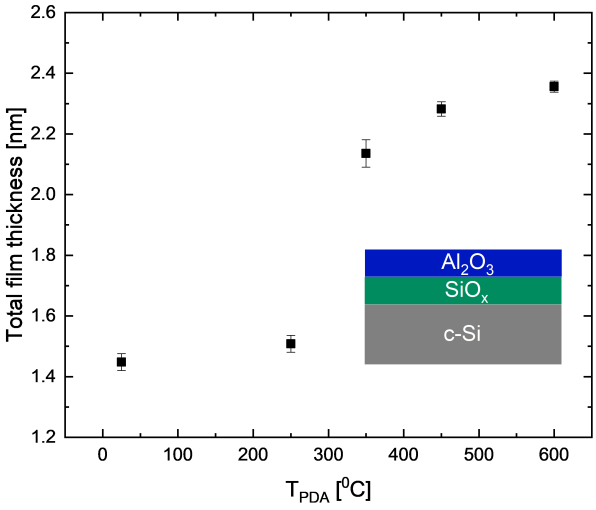

Figure 3.2.: Thickness of 8 cycles spatial ALD Al_2O_3 film after different PDA with temperature ranging from 250-600 °C, 5 points measured across the wafer. The film thickness represents the total thickness of the SiO_x and the Al_2O_3 layers and it was included in the ellipsometry model. Note that T_{PDA} = 25 °C represents the as-deposited Al_2O_3 film.

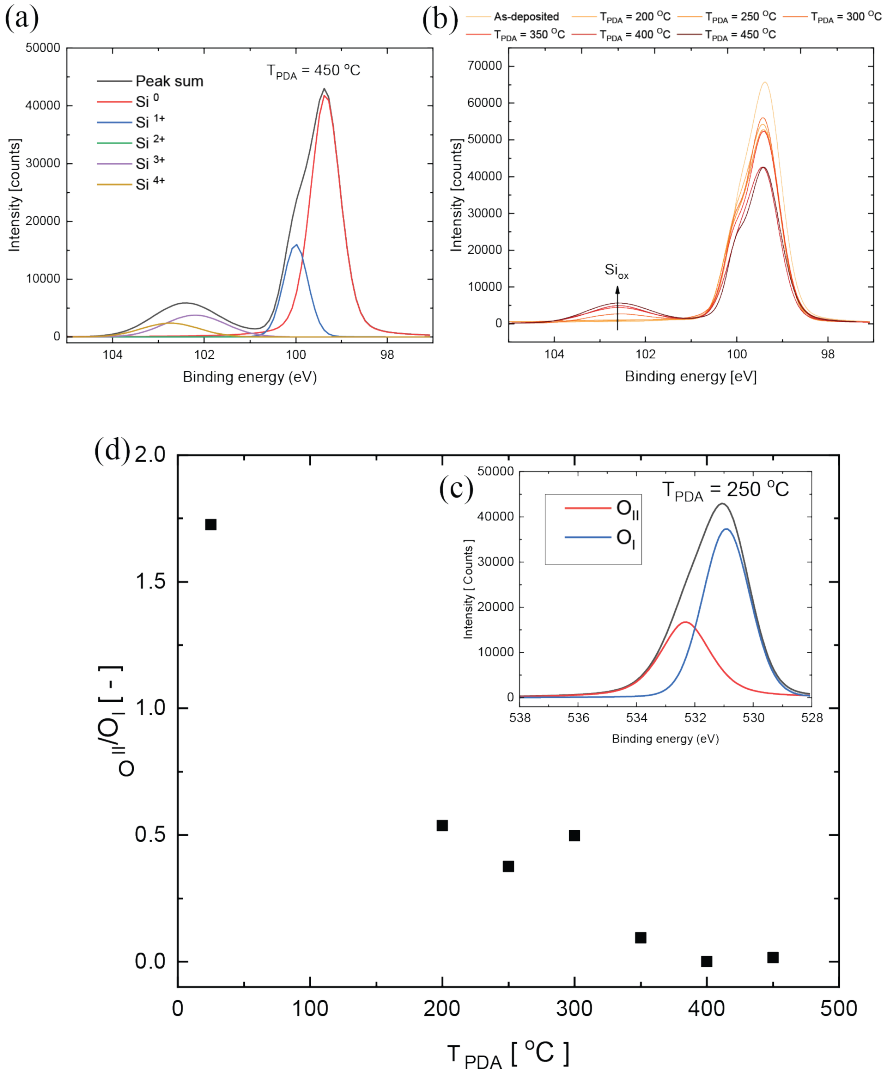

Figure 3.3.: (a) Oxidation states decomposed for Si 2p photoelectron peak annealed at T_{PDA} = 450 °C, (b) Si 2p of annealed Al_2O_3 films (c) decomposed O 2s photoelectron peak annealed at T_{PDA} = 250 °C, and (d) O_{II}/O_I ratio calculated for the decomposed O2s spectra for ultra-thin Al_2O_3 films annealed at T_{PDA} 200 – 450 °C. Shirley background is used and subtracted from the analysis.

Altogether, the XPS data indicates that the thickening of the interlayer is probably due to the formation of Si-O bonds and, therefore, due to oxidation of the Si interface.

In Figure 3.3(c), the O 1s spectra is decomposed into two distinct peaks: the lower binding energy, O_I represents the Al-O, and the higher binding energy, O_{II} represents the OH groups [16, 17]. Figure 3.3(d) depicts the ratio between O_{II} and O_I, as a function of T_{PDA}. The O_{II}/O_I decreases significantly with annealing temperature, which indicates that there is a strong rearrangement of the atomic bindings under release of H during annealing [18].

3.3.2. SURFACE PASSIVATION AND CONTACT SELECTIVITY OF SOLAR CELL PRECURSOR

Here, we investigate the effect of T_{PDA} on the surface passivation and contact selectivity of the solar cell precursor after MoO_x and ITO films deposition (precursors are shown in Figure 3.1 as step 4 and 5). In addition, a curing anneal treatment is performed on the precursors at standard SHJ conditions (190 °C for 30 min). Note that, no curing step is included in between the MoO_x and ITO depositions. Figure 3.4(a) shows the effects of T_{PDA} on the iV_{oc} after deposition of MoO_x, after subsequent deposition of ITO, and followed by a curing annealing. An increase in iV_{oc} is observed with respect to T_{PDA}, after MoO_x is deposited on the annealed Al_2O_3 interlayer (see appendix A). Subsequently, PVD ITO films are deposited on both sides of the cell percursor. Interestingly, the induced sputtering damage is more pronounced for an Al_2O_3 interlayer that received a higher T_{PDA} treatment. After performing a curing anneal treatment, the precursor with an Al_2O_3 interlayer annealed at 350 °C shows partial recovery of the passivation quality. On the other hand, the solar cell with an Al_2O_3 interlayer treated at T_{PDA} = 600 °C shows a decrease in iV_{oc}. In this case, the sputtering-induced damage cannot be recovered and iV_{oc} decreases even further after subsequent curing anneal.

Next, we investigate the contact selectivity loss before and after a curing anneal, by comparing iV_{oc} and $SunsV_{oc}$ values on the same samples. It is often observed that MoO_x contacts with an a-Si:H interlayer show a loss in selectivity after a curing anneal at temperatures above 130 °C [19]. This is related to a reduction in the induced band bending [20] due to a lowered MoO_x WF. Due to this loss in WF, the high internal potential (iV_{oc}), as a result of a high quality c-Si wafer and good surface passivation, cannot be fully 'extracted', which results in a lowered external potential (V_{oc}). For this reason, ΔV_{oc} (iV_{oc}-V_{oc}) is commonly used as a figure of merit to define the selectivity loss of the contact. In Figure 3.5(b), this selectivity loss is depicted for different T_{PDA} of the Al_2O_3 interlayer, before and after 190 °C curing of cell precursors (without Ag contacts). The contact selectivity shows a dependency on the thermal treatment performed on the Al_2O_3 interlayer; a decrease in contact selectivity loss is observed with decreasing T_{PDA}. At T_{PDA} = 600 °C, the selectivity loss of the contact is high but can be partially reduced to 90 mV after annealing. However, at T_{PDA} <350 °C, minor contact selectivity loss is displayed by the samples, before and after anneal. In comparison, a substantial contact selectivity loss was observed, before and after curing, when an a-Si:H(i) interlayer was used with our MoO_x contact [21]. This demonstrates a stable contact selectivity of our moly-poly cells with Al_2O_3 interlayer and after annealing.

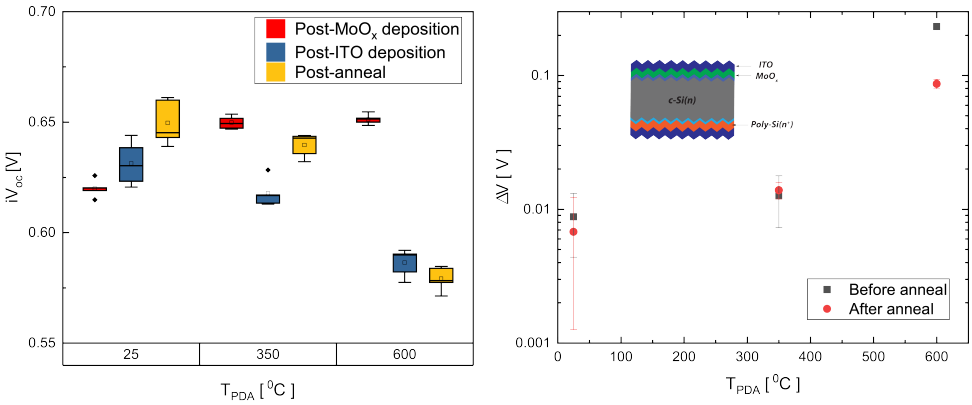

Figure 3.4.: Left: iV_{oc} of the hole contact at different manufacturing stages of the hole contact at different T_{PDA}. Right: ΔV_{oc} ($iV_{oc} - external V_{oc}$) before and after anneal (190 °C) at the specified T_{PDA}.

3.3.3. *IV* RESULTS

The front metal grid was screen-printed on the 6 inch cell, and subsequently the same curing anneal as for the cell precursors, 190 °C for 30 min, was performed to recover the sputtering damage and ensure good contact between Ag and ITO layers. Figure 3.5 (left) shows a significant difference in IV characteristics depending on the thermal treatment on the Al_2O_3 interlayer; a decrease in FF and V_{oc} is observed for solar cells with an Al_2O_3 interlayer that received a PDA at 350 °C or 600 °C in the MoO_x contact. The solar cell with a 350 °C anneal of the Al_2O_3 interlayer shows a slight appearance of an S-shaped IV curve. This effect is aggravated when a thermal budget of T_{PDA} = 600 °C is used to treat the Al_2O_3 interlayer. On the other hand, the solar cell without PDA on the Al_2O_3 interlayer exhibits good FF and V_{oc} without any S-shaped IV characteristics. Additionally, we show, in Figure 3.4 (right), that the insertion of an Al_2O_3 interlayer does not affect the FF, and even improves the V_{oc} of the MoO_x contact.

The best conversion efficiency was, therefore, obtained after the solar cell was cured at 210 °C, while no change in contact selectivity was observed. This resulted

Table 3.1.: IV characteristics for solar cells with Al_2O_3 interlayers treated at different temperatures. The champion solar cell was achieved by using a curing temperature of 210 °C.

T_{PDA} of interlayer [°C]	T_{curing} [°C]	J_{sc} [mA/cm^2]	V_{oc} [mV]	FF	η [%]
600	190	32.2	516	20.1	3.3
350	190	37.2	628	60.3	14.1
As-deposited	190	36.9	650	75.5	18.1
As-deposited	210	36.9	651	75.6	18.2

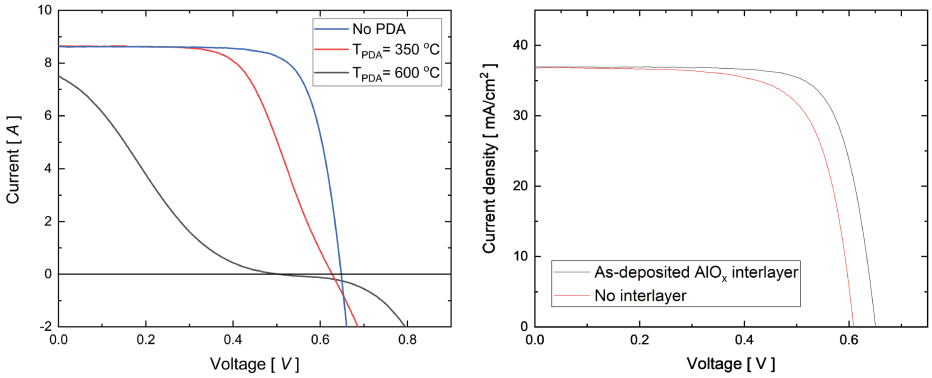

Figure 3.5.: Left: IV curves of the 'moly-poly' solar cells with different T_{PDA} performed on the Al_2O_3 interlayer. Right: comparison between MoO_x contacts with and without the as-deposited Al_2O_3 interlayer.

in a 6 inch solar cell with a reasonable conversion efficiency of 18.2% with V_{oc} of 651 mV, FF of 75.6% and J_{sc} of 36.9 mA/cm^2, as shown in Table 3.1. The increase in thermal budget did not lead to an S-shaped IV curve, which was commonly perceived for solar cells with an a-Si:H interlayer in the MoO_x contact. A slight gain in FF andV_{oc} is observed as the annealing time and annealing temperature are increased. Likely reasons for this gain are an improvement in surface passivation after ITO is sputtered [22], an increase in FF due to a better crystallization of the ITO, the ITO sheet resistance changes from 113 to 95 Ω/sq as it is annealed from 190 to 210 °C, and a better contact between the metal electrodes and the ITO layer. By manufacturing the MoO_x contact without an a-Si:H based layer, a higher thermal budget can been used. This may benefit the device's performance, while allowing for higher temperature metal contacts and better module interconnection processes, in comparison to SHJ technologies.

3.3.4. OPTICAL LOSSES ANALYSIS

To quantify the current losses shown by our solar cell structure, an in-depth analysis is performed by following a method presented by Paviet-Salomon et al. [23]. This analysis is shown in Figure 3.6(a) where the losses of our moly-poly cell can be categorized in terms of external and internal losses. External losses refers to optical losses that is caused by reflection and escape of light at the front side of the solar cell. In contrast, internal losses originates from the parasitic absorption induced by passivating and carrier-selective contacts, and consequently, do not contribute to the absorption of light in the Si absorber. To facilitate the discussion, the internal losses are separated in three regions throughout the solar spectrum: short wavelength losses ranging between 350 – 600 nm (J_{short}), medium wavelength losses ranging between 600 – 1000 nm (J_{medium}), and long wavelength losses ranging between 1000 – 1200 nm (J_{long}). Finally, we account for the shadowing loss caused by the front Ag

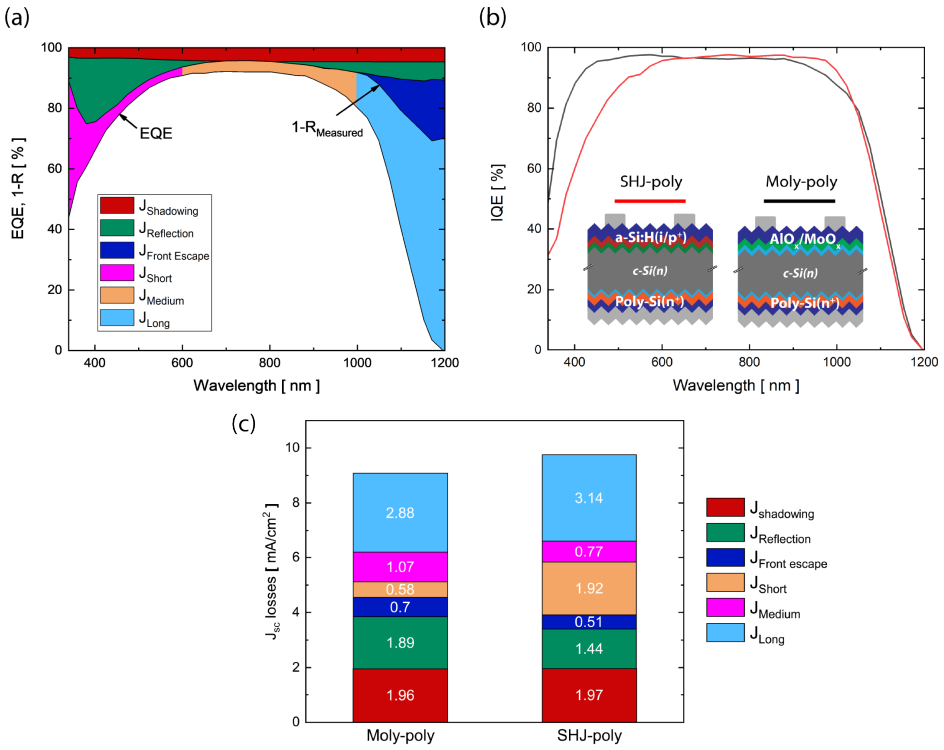

Figure 3.6.: (a) Internal and external J_{sc} losses analysis of our moly-poly solar cell, (b) IQE and (c) quantified J_{sc} losses compared for our reference SHJ-poly and moly-poly solar cells.

metal grid while no transmission losses is considered at the rear side since the cell consists of a full metallized Ag blanket.

In addition, the optical characteristic of our moly-poly cell is compared to a conventional front SHJ (a-Si:H($i/p+$) contacts and is referred as the "SHJ-poly" cell. Figure 3.6(b) compares the internal quantum efficiency (IQE) of both cells. A clear gain in spectral response is observed by replacing the SHJ emitter by MoO_x/Al_2O_3 stack, in the short wavelength region. Nevertheless, the apparent IQE loss of the moly-poly cell in the medium wavelength region should be improved to make full use of the transparency potential of this contact. To quantify the current gain, a breakdown of the J_{sc} losses is calculated, as shown in Figure 3.6(c). The total J_{sc} loss for the moly-poly and SHJ-poly cells are 9.08 mA/cm^2 and 9.75 mA/cm^2, respectively. The $J_{reflection}$ loss of the moly-poly cell is 0.45 mA/cm^2 higher than the SHJ-poly one which is due to the unoptimized ITO thickness. A noticeable gain in J_{short} of 1.32 mA/cm^2 is obtained by replacing an a-Si:H($i/p+$) by our MoO_x/Al_2O_3 stack and is now limited by the parasitic absorption of the ITO film. This exhibit the excellent transparency potential of this contact. On the other hand, a difference of 0.3 mA/cm^2 exists in the middle wavelength range between both cells, and is likely

related to the sub-bandgap absorption caused by sub-stoichiometric MoO_x film [10]. Further optimization can be performed to achieve a highly transparent contact by minimizing the observed losses.

3.4. DISCUSSION

The Al_2O_3 interlayer, in its as-deposited state, consists of an amorphous SiO_x interfacial layer and residual OH groups at the Si interface which originate from the imperfect growth during the ALD initial cycles [24]. At this stage, no consistent Si-O and Si-H bonds are formed at the Si interface. After a thermal treatment in an N_2 environment, the residual OH groups are consumed to create new Si-O and Si-H bonds which passivate some of the Si dangling bonds present at the interface. However, this reaction only happens at T_{PDA}> 300 °C where the thermal energy is sufficient for the oxidation of Si by OH groups under release of H [25]. At even higher annealing temperature, an increase in layer stoichiometry indicates that the Si-O bonds are still being formed since this reaction relies on the thermal activation energy to facilitate the formation of Si-O bonds. As a result, the enhanced Si-O coordination leads to an improved chemical passivation but in turn causes the thickening of the interlayer, which becomes critical, when it is used as a tunneling transport interlayer in a hole selective contact. In the case of an Al_2O_3 interlayer annealed at T_{PDA} < 300 °C, the OH groups do not contribute to the formation of the oxide interlayer and hence are allowed to effuse from the layer. This is shown by the reduction of O_{II} peak of the Al_2O_3 layers.

Interestingly, the induced sputtering damage, caused by ITO deposition on our contacts, shows a strong dependency on the thermal budget used on the interlayer. Sputtering damage is commonly caused by high energetic particles bombardment and/or photons which disturbs the bonding configuration at the interface [26]. This effect is commonly observed for SHJ solar cells where Si-H bonds from the a-Si:H(i) interlayer are ruptured after TCO deposition. Nevertheless, the surface passivation can be fully restored by a low temperature annealing treatment (~200 °C). On the other hand, for doped poly-Si passivating contacts - which consist of a SiO_x interlayer, the sputtering damage can only be partially cured by thermal treatments. Tutsch et al. [22] showed that an improved surface passivation of poly-Si contacts can be attained by increasing the thermal budget (>350 °C) during the post-annealing step. This likely indicates that the activation energy required to re-passivate the SiO_x interlayer of poly-Si contacts is larger than in a-Si:H films. Here, we speculate that the enhanced Si-O coordination - due to annealing of the Al_2O_3 films, is the origin of the aggravated sputtering damage; the sputtering damage causes the de-passivation of the Si-O bonds at the interface which cannot be fully repaired under a low thermal budget (190-210 °C). Nevertheless, further analysis is required to underpin the exact passivation mechanism of the interfacial layers which is beyond the scope of this study.

Additionally, the contact selectivity loss and formation of the S-shaped IV curve show a high dependency on the thermal treatment performed on the Al_2O_3 interlayer. The contact selectivity limitation has been typically reported for MoO_x contacts with

an a-Si:H(i) interlayer and originates from the reduced MoO_x WF under a thermal treatment [10, 27]. However, in our case, the deposition process of the MoO_x layers was identical for all solar cells since the MoO_x layers were exposed to the same post-thermal process. As a result, there is no reason to assume that the WF of these layers and, therewith the induced band bending, should be different. Alternatively, the contact selectivity loss and the appearance of an S-shaped IV curve, caused by the annealing of the Al_2O_3 interlayer, are likely to be caused by the impeded hole carrier collection across the interlayer. This, in turn, results in an accumulation of holes under the c-Si absorber surface [28] which can cause severe recombination losses [29] and hence, contact selectivity loss. The transport barrier for holes can be explained by the thickening of the interlayer with annealing temperature which results in an inefficient tunneling transport through the interlayer. Additionally, the tunneling transport across the annealed interlayer can be restricted due to the interlayer bandgap widening caused by the increase in layer stoichiometry [30]. This results in a higher valence band offset which impedes the hole collection [3, 30, 31]. In the case of an as-deposited Al_2O_3 interlayer, no selectivity loss is observed for the contact and even slightly improves with annealing. The thermal stability is likely to originate from an enhance hole interlayer transport properties which does not hamper the hole carriers collection.

It is worth noting that additional confirmation of these observations can be obtained through further measurements. Specifically, measurements, such as surface photovoltage (SPV), could be carried out to verify the impact of the oxide interlayers on the induced band bending facilitated by the MoO_x layer. Conversely, the rise in the valence band edge position resulting from an increase in T_{PDA} could be determined through ultraviolet photoelectron spectroscopy (UPS) measurements. These additional measurements could be part of a future project to further confirm the interacting observed effects.

3.5. CONCLUSIONS

In this work, we demonstrated that an ultra-thin Al_2O_3 can be used as an interlayer for MoO_x-based contacts. The Al_2O_3 interlayer allows for an improved surface passivation while showing no detrimental effect on the contact selectivity and the shape of the IV curve. In addition, we showed that a PDA treatment on the Al_2O_3 interlayer can have a negative effect on the performance of the device for the following reasons: 1) the interlayer thickness considerably increases at T_{PDA}> 300 °C due to the formation of Si-O bonds, 2) Si-O bonds formed during annealing become more sensitive to sputtering damage, 3) annealing limits the hole transport through the interlayer and consequently results in a contact selectivity loss. As a result, we showed that an excellent contact selectivity and thermal stability can be achieved by using an as-deposited Al_2O_3 interlayer. Nevertheless, further work is required to improve the surface passivation of the Al_2O_3 interlayer without hampering the hole carriers transport through the interlayer, and to determine more details about the involving carrier transport mechanisms.

REFERENCES

[1] M. T. S. K. A. Sen, P. Bronsveld, and A. Weeber. “Thermally stable MoOx hole selective contact with Al2O3 interlayer for industrial size silicon solar cells”. In: *Solar Energy Materials and Solar Cells* 230 (2021), p. 111139.

[2] L. Mazzarella, S. Kirner, O. Gabriel, S. S. Schmidt, L. Korte, B. Stannowski, B. Rech, and R. Schlatmann. “Nanocrystalline silicon emitter optimization for Si-HJ solar cells: substrate selectivity and CO2 plasma treatment effect”. In: *physica status solidi (a)* 214.2 (2017), p. 1532958.

[3] J. Peter Seif, A. Descoeudres, M. Filipič, F. Smole, M. Topič, Z. Charles Holman, S. De Wolf, and C. Ballif. “Amorphous silicon oxide window layers for high-efficiency silicon heterojunction solar cells”. In: *Journal of Applied Physics* 115.2 (2014), p. 024502.

[4] A. N. Fioretti, M. Boccard, R. Monnard, and C. Ballif. “Low-temperature p-type microcrystalline silicon as carrier selective contact for silicon heterojunction solar cells”. In: *IEEE Journal of Photovoltaics* 9.5 (2019), pp. 1158–1165.

[5] C. Battaglia, S. M. De Nicolas, S. De Wolf, X. Yin, M. Zheng, C. Ballif, and A. Javey. “Silicon heterojunction solar cell with passivated hole selective MoOx contact”. In: *Applied Physics Letters* 104.11 (2014), p. 113902.

[6] M. Bivour, J. Temmler, F. Zähringer, S. Glunz, and M. Hermle. “High work function metal oxides for the hole contact of silicon solar cells”. In: *2016 IEEE 43rd Photovoltaic Specialists Conference (PVSC)*. IEEE. 2016, pp. 0215–0220.

[7] L. G. Gerling, C. Voz, R. Alcubilla, and J. Puigdollers. “Origin of passivation in hole-selective transition metal oxides for crystalline silicon heterojunction solar cells”. In: *Journal of Materials Research* 32 (2017), pp. 260–268.

[8] L. Cao, P. Procel, A. Alcañiz, J. Yan, F. Tichelaar, E. Özkol, Y. Zhao, C. Han, G. Yang, Z. Yao, *et al.* “Achieving 23.83% conversion efficiency in silicon heterojunction solar cell with ultra-thin MoOx hole collector layer via tailoring (i) a-Si: H/MoOx interface”. In: *Progress in Photovoltaics: research and applications* (2022).

[9] P. Würfel and U. Würfel. *Physics of solar cells: from basic principles to advanced concepts*. John Wiley & Sons, 2016.

[10] L. Neusel, M. Bivour, and M. Hermle. “Selectivity issues of MoOx based hole contacts”. In: *Energy Procedia* 124 (2017), pp. 425–434.

[11] B. Hoex, J. Schmidt, P. Pohl, M. Van de Sanden, and W. Kessels. “Silicon surface passivation by atomic layer deposited Al 2 O 3”. In: *Journal of Applied Physics* 104.4 (2008), p. 044903.

[12] G. Dingemans, P. Engelhart, R. Seguin, F. Einsele, B. Hoex, M. Van de Sanden, and W. Kessels. “Stability of Al 2 O 3 and Al 2 O 3/a-SiN x: H stacks for surface passivation of crystalline silicon”. In: *Journal of Applied Physics* 106.11 (2009), p. 114907.

[13] B. E. Davis and N. C. Strandwitz. “Aluminum oxide passivating tunneling interlayers for molybdenum oxide hole-selective contacts”. In: *IEEE Journal of Photovoltaics* 10.3 (2020), pp. 722–728.

[14] Z. Xin, Z. P. Ling, P. Wang, J. Ge, C. Ke, K. B. Choi, A. G. Aberle, and R. Stangl. “Ultra-thin atomic layer deposited aluminium oxide tunnel layer passivated hole-selective contacts for silicon solar cells”. In: *Solar Energy Materials and Solar Cells* 191 (2019), pp. 164–174.

[15] G. Gregory, C. Feit, Z. Gao, P. Banerjee, T. Jurca, and K. O. Davis. “Improving the passivation of molybdenum oxide hole-selective contacts with 1 nm hydrogenated aluminum oxide films for silicon solar cells”. In: *physica status solidi (a)* 217.15 (2020), p. 2000093.

[16] O. Renault, L. Gosset, D. Rouchon, and A. Ermolieff. “Angle-resolved x-ray photoelectron spectroscopy of ultrathin Al 2 O 3 films grown by atomic layer deposition”. In: *Journal of Vacuum Science & Technology A: Vacuum, Surfaces, and Films* 20.6 (2002), pp. 1867–1876.

[17] M. Alexander, G. Thompson, and G. Beamson. “Characterization of the oxide/hydroxide surface of aluminium using x-ray photoelectron spectroscopy: a procedure for curve fitting the O 1s core level”. In: *Surface and Interface Analysis: An International Journal devoted to the development and application of techniques for the analysis of surfaces, interfaces and thin films* 29.7 (2000), pp. 468–477.

[18] G. Dingemans, W. Beyer, M. Van de Sanden, and W. Kessels. “Hydrogen induced passivation of Si interfaces by Al 2 O 3 films and SiO 2/Al 2 O 3 stacks”. In: *Applied physics letters* 97.15 (2010), p. 152106.

[19] J. Geissbühler, J. Werner, S. Martin de Nicolas, L. Barraud, A. Hessler-Wyser, M. Despeisse, S. Nicolay, A. Tomasi, B. Niesen, S. De Wolf, *et al.* “22.5% efficient silicon heterojunction solar cell with molybdenum oxide hole collector”. In: *Applied Physics Letters* 107.8 (2015), p. 081601.

[20] F. Feldmann, M. Simon, M. Bivour, C. Reichel, M. Hermle, and S. W. Glunz. “Efficient carrier-selective p-and n-contacts for Si solar cells”. In: *Solar Energy Materials and Solar Cells* 131 (2014), pp. 100–104.

[21] M. A. Sen, P. Spinelli, B. Kikkert, E. Hoek, B. Macco, A. Weeber, and P. Bronsveld. “Electron beam evaporated molybdenum oxide as hole-selective contact in 6-inch c-Si heterojunction solar cells”. In: *AIP Conference Proceedings*. Vol. 1999. 1. AIP Publishing LLC. 2018, p. 040001.

[22] L. Tutsch, F. Feldmann, J. Polzin, C. Luderer, M. Bivour, A. Moldovan, J. Rentsch, and M. Hermle. “Implementing transparent conducting oxides by DC sputtering on ultrathin SiOx/poly-Si passivating contacts”. In: *Solar Energy Materials and Solar Cells* 200 (2019), p. 109960.

[23] B. Paviet-Salomon, A. Tomasi, A. Descoeudres, L. Barraud, S. Nicolay, M. Despeisse, S. De Wolf, and C. Ballif. “Back-contacted silicon heterojunction solar cells: optical-loss analysis and mitigation”. In: *IEEE Journal of Photovoltaics* 5.5 (2015), pp. 1293–1303.

[24] V. Naumann, M. Otto, R. B. Wehrspohn, and C. Hagendorf. “Chemical and structural study of electrically passivating Al2O3/Si interfaces prepared by atomic layer deposition”. In: *Journal of Vacuum Science & Technology A: Vacuum, Surfaces, and Films* 30.4 (2012), p. 04D106.

[25] L. Gosset, J.-F. Damlencourt, O. Renault, D. Rouchon, P. Holliger, A. Ermolieff, I. Trimaille, J.-J. Ganem, F. Martin, and M.-N. Semeria. “Interface and material characterization of thin Al2O3 layers deposited by ALD using TMA/H2O”. In: *Journal of non-crystalline solids* 303.1 (2002), pp. 17–23.

[26] B. Demaurex, S. De Wolf, A. Descoeudres, Z. Charles Holman, and C. Ballif. “Damage at hydrogenated amorphous/crystalline silicon interfaces by indium tin oxide overlayer sputtering”. In: *Applied Physics Letters* 101.17 (2012), p. 171604.

[27] S. Essig, J. Dréon, E. Rucavado, M. Mews, T. Koida, M. Boccard, J. Werner, J. Geissbühler, P. Löper, M. Morales-Masis, *et al.* “Toward annealing-stable molybdenum-oxide-based hole-selective contacts for silicon photovoltaics”. In: *Solar Rrl* 2.4 (2018), p. 1700227.

[28] M. Filipič, Z. C. Holman, F. Smole, S. De Wolf, C. Ballif, and M. Topič. “Analysis of lateral transport through the inversion layer in amorphous silicon/crystalline silicon heterojunction solar cells”. In: *Journal of Applied Physics* 114.7 (2013), p. 074504.

[29] R. Anderson. “Photocurrent suppression in heterojunction solar cells”. In: *Applied Physics Letters* 27.12 (1975), pp. 691–693.

[30] M. Liebhaber, M. Mews, T. Schulze, L. Korte, B. Rech, and K. Lips. “Valence band offset in heterojunctions between crystalline silicon and amorphous silicon (sub) oxides (a-SiOx: H, 0< x< 2)”. In: *Applied Physics Letters* 106.3 (2015), p. 031601.

[31] J. P. Seif, D. Menda, A. Descoeudres, L. Barraud, O. Özdemir, C. Ballif, and S. De Wolf. “Asymmetric band offsets in silicon heterojunction solar cells: Impact on device performance”. In: *Journal of Applied Physics* 120.5 (2016), p. 054501.

4

INFLUENCE OF PASSIVATING INTERLAYERS ON THE CARRIER SELECTIVITY OF MoO_X CONTACTS FOR C-SI SOLAR CELLS

The application of molybdenum oxide (MoO_x) as a hole-selective contact for silicon-based solar cells has been explored due to superior optical transmittance and potentially leaner manufacturing compared to fully amorphous silicon-based heterojunction (SHJ) devices. However, the development of MoO_x contacts has been hampered by their poor thermal stability, resulting in a carrier selectivity loss and an S-shaped IV curve. The aim of this study is to understand the influence of different passivating interlayers on the carrier selectivity of hole-selective MoO_x contacts for crystalline silicon (c-Si) solar cells. We highlight the effect of different interlayers on the surface passivation quality, contact selectivity, and the thermal stability of our MoO_x-contacted devices. The interlayers studied are intrinsic hydrogenated amorphous silicon (a-Si:H(i)), thermally grown ultrathin SiO_2, and a stack consisting of an ultrathin SiO_y and Al_2O_3 layer. Additionally, we simulate the interacting interlayer properties on the carrier selectivity of our MoO_x contacts using a simplified model. Among these interlayers, the Al_2O_3/SiO_y stack shows to be a promising alternative to SiO_2 by enabling efficient transport of holes while being able to sustain an annealing temperature of at least 250 °C underlining its potential in module manufacturing and outdoor operation.

This chapter is based on an article submitted by M. T. S. K. A. Sen, G. Janssen, A. Mewe, P. Bronsveld, J. Melskens, F. Hashemi, P. Procel, and A. Weeber. "Influence of passivating interlayers on the carrier selectivity of MoO_X contacts for c-Si solar cells Journal EPJ, submitted on: 20.02.24

4.1. Introduction

Currently, the conversion efficiencies of conventional homojunction crystalline silicon (c-Si) solar cells are mainly limited by the recombination of charge carriers occurring at the metal/silicon interface. This limitation is minimized by including a stack of passivating and carrier-selective layers in between the Si absorber and metal electrodes which effectively suppresses the recombination at the c-Si surface while simultaneously being conductive to either electrons or holes generated in the c-Si absorber. Nowadays, the highest conversion efficiency of Si solar cells comprising amorphous silicon heterojunction (SHJ) or doped polycrystalline Si contacts are manufactured by using this type of so-called passivating contact scheme [1, 2]. Nevertheless, these highly doped Si-based passivating contacts are a source of parasitic absorption, which consequently reduces the total amount of photogenerated carriers inside the Si absorber, resulting in a lower current. For instance, doped poly-Si typically used in passivating contact structures, suffers from high parasitic absorption [3]. In the case of amorphous silicon, its direct band gap of approximately 1.7 eV in combination with its heavily doped layers hinder the short-circuit current density (J_{sc}) of SHJ solar cells [4, 5].

In order to minimize the J_{sc} losses sustained by these layers, alternative transparent selective contacts, such as metal oxides have been explored due to their wide band gap, capability to extract charge carriers, good surface passivation quality on c-Si, and the relatively simple physical vapor deposition (PVD) techniques that have been used to fabricate them [6, 7]. For instance, evaporated MoO_x has been investigated for its transparency in the blue wavelength region and its ability to act as a hole-selective contact for c-Si solar cells [8–10]. Recently, a conversion efficiency of 23.83 % and J_{sc} gain of 2.77 mA/cm^2 have been achieved by replacing the p-type hydrogenated amorphous silicon (a-Si:H(p+)) layer with a MoO_x hole-selective contact in a SHJ solar cell structure [11]. Nevertheless, a MoO_x/a-Si:H(i)/c-Si contact has shown to degrade considerably at standard SHJ annealing conditions [12, 13], causing the appearance of an S-shaped current-voltage (IV) curve, and accordingly a loss in fill factor (FF). Additionally, while the doped a-Si:H layer is omitted in that structure, the intrinsic a-Si:H layer is still present, meaning that the high transparency of the MoO_x layer is not fully exploited due to the absorptive nature of intrinsic a-Si:H (a-Si:H(i)) layer. The lack of thermal stability of the MoO_x/a-Si:H(i)/c-Si contact is a significant limitation in the potential manufacturing of the SHJ-like solar cells since an annealing temperature of about 200 °C is often required to recover from sputtering damage after deposition of the transparent conductive oxide (TCO) layer and is an essential back-end treatment during metallization and TCO post-crystallization. While a MoO_x/a-Si:H(i)/c-Si contact provides excellent surface passivation properties, the insertion of an a-Si:H(i) interlayer poses several transport issues which could result in the formation of the S-shaped IV curve.

In search of alternative passivating interlayers, ultrathin SiO_2 layers (< 2 nm) are a potential candidate in replacing a-Si:H(i) due to their ability to provide excellent surface passivation and contact selectivity when combined with doped poly-Si contacts [14]. However, unlike poly-Si contacts where excellent surface passivation properties can be achieved, the insertion of an oxide interlayer results

in apparent hole collection issues when combined with MoO_x [15–17] even though sufficient band bending is typically obtained at the c-Si interface [18]. Conversely, the selectivity of MoO_x contacts with an Al_2O_3 interlayer has shown to be promising with good surface passivation and contact resistance properties [19]. In addition, as shown in Chapter 3, an ultrathin atomic layer deposited (ALD) Al_2O_3/SiO_y interlayer stack does not impede the hole selectivity provided by the MoO_x contact, resulting in good contact selectivity and cell performance [20]. Note that the ultrathin SiO_y is naturally formed at the c-Si surface during the initial cycles of the ALD Al_2O_3 process, as has been repeatedly documented elsewhere [21, 22].

The aim of this work is to further understand the interaction between the salient factors of the passivating interlayer, or interlayer stack, and MoO_x contact that influence the contact selectivity. A comparative study between different interlayers, notably a-Si:H(i), SiO_2, and Al_2O_3/SiO_y is made where the non-ideal carrier extraction behavior, caused by the insertion of an interlayer on our MoO_x based contact, is addressed. Since the carrier transport mechanisms of the aforementioned interlayers involve different transport mechanisms, such as band-to-band tunneling, defect-assisted transport, and pinhole aided transport, a simple model is developed to encompass the different transport properties of these interlayers. In this model, the interlayer is represented by a thin layer with limited charge carrier mobility. This gives us a premise to explore different interlayers with suitable layer parameters that are necessary to obtain an effective MoO_x-based passivating contact.

4.2. EXPERIMENTAL DETAILS

4.2.1. SOLAR CELL FABRICATION AND CHARACTERIZATION

To investigate the impact of the different interlayers on the solar cell performance n-type c-Si solar cells with MoO_x-based hole contacts at the front are studied. A rear poly-Si(n+) contact is used because of its excellent surface passivation quality, contact resistance, and thermal stability, such that the front hole MoO_x-based contact is limiting in the measurements and not the rear poly-Si contact.

The manufacturing steps of the solar cells with front side thermal SiO_2, Al_2O_3/SiO_y, or a-Si:H(i) interlayers and the cell schematic are shown in Figure 6.1. The 6-inch, 180 µm thick pseudo-square Cz c-Si(n) substrates with a resistivity of about 3 Ohm.cm were processed as follows: textured in a KOH solution, pre-gettered with $POCl_3$ diffusion followed by phosphosilicate removal (removal of the pre-gettered layer), surface smoothing etch, and finally cleaned in RCA 1 and 2, and nitric acid oxidation step (NAOS) solutions. Note that the surface smoothing is only a minor surface treatment in the sense that the textured morphology is still preserved overall. The substrates were dipped in a 1% HF solution prior to the formation of the NH_3 plasma hydrogenated rear SiO_2/poly-Si(n+) contact. The SiO_2 interlayer (~1.3 nm) was thermally grown in a low pressure chemical vapor deposition (LPCVD) chamber at 610 °C. In the case of an ultrathin SiO_2 interlayer, the thermal oxide at the front side was preserved. The samples with a-Si:H(i) and Al_2O_3/SiO_y interlayers were dipped in a 1% HF bath to remove the front thermal oxide. Subsequently, the a-Si:H(i) and Al_2O_3/SiO_y interlayers were deposited using plasma-enhanced chemical

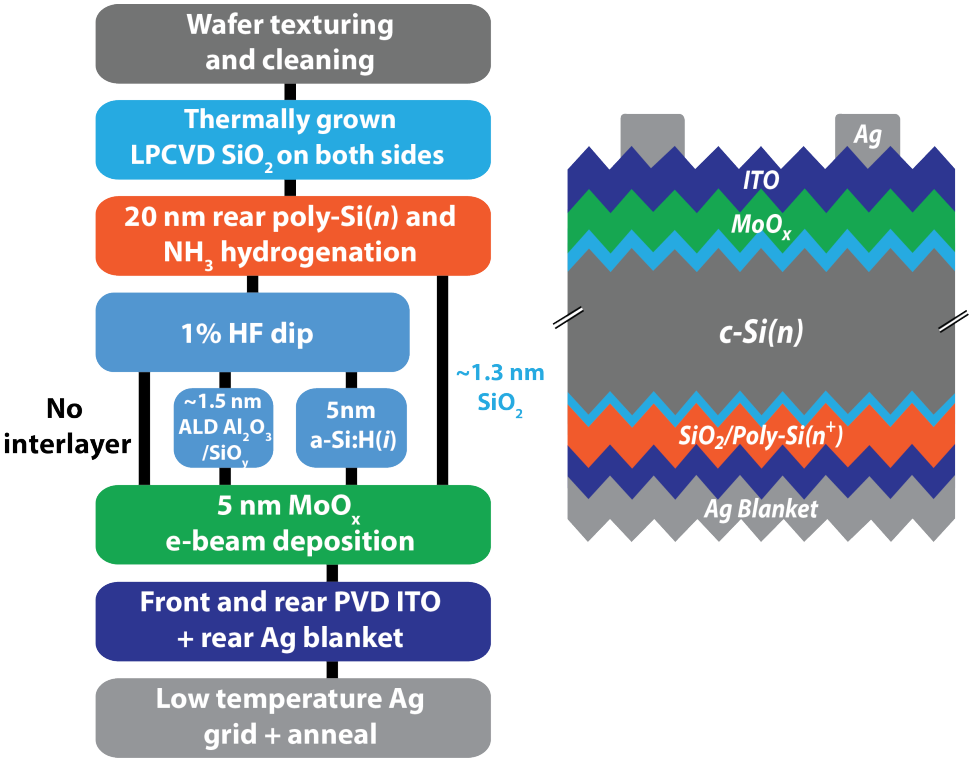

Figure 4.1.: Process flow for the manufacturing of the solar cells with different interlayers (left), and a schematic of the solar cells (right).

vapor deposition (PECVD) and spatial ALD tools, respectively. 8 cycles of spatial ALD Al_2O_3 were used to deposit a 1.5 nm thick Al_2O_3/SiO_y stack. These layers were deposited using a Levitrack deposition tool without any subsequent post-deposition annealing treatment. The samples without interlayer only received an HF dip prior to MoO_x deposition. Next, the samples were transferred to an electron beam physical vapor deposition (PVD) tool where a 5 nm MoO_x layer was deposited in a high vacuum ($7x10^{-6}$ mbar) environment. Finally, indium tin oxide (ITO) films were deposited in a sputtering tool on both sides of the samples and a full area Ag sheet was also deposited at the rear side by sputtering. To finalize the solar cells, a front Ag grid was screen printed using a low temperature Ag paste and the device was cured in air at different temperatures.

The photoconductance of charge carrier lifetime samples was measured by using a Sinton WCT-120 system, as well as the internal voltage expressed in terms of the implied open circuit voltage iV_{oc}. The external V_{oc} of the half-fabricated cells were measured by a $SunsV_{oc}$ Sinton tool which does not require metal contacts due to the conductivity of the ITO films, as shown in Figure 4.2. The solar cells were characterized by IV measurements in a Wacom AAA solar simulator at

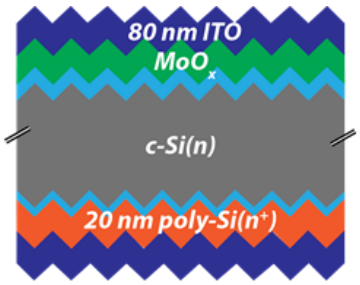

Figure 4.2.: Solar cell precursors with front MoO_x and rear poly-Si(n+) contacts for iV_{oc} and $SunsV_{oc}$ measurements.

standard test conditions. The results were corrected for spectral mismatch. Dark IV measurements were performed at varying temperature between 25 and 65 °C using the Wacom solar simulator. The interlayer films were deposited on single-side polished c-Si wafers with unpolished backsides to eliminate back reflections during ellipsometry measurement. The thickness of the interlayers was determined using a spectroscopic ellipsometer (J.A. Woollam Co., Inc.). Ellipsometric data was collected at three angles of incidence (60°, 70°, and 80°) and over a photon energy range of 1.1 to 5 eV. The Cauchy model was used to analyze oxide layers.

4.2.2. SIMULATIONS AND CALCULATIONS

2D simulations were performed by using the Atlas package of Silvaco [25] and using a simple metal-semiconductor like contact. Figure 4.3 depicts the cell structure used

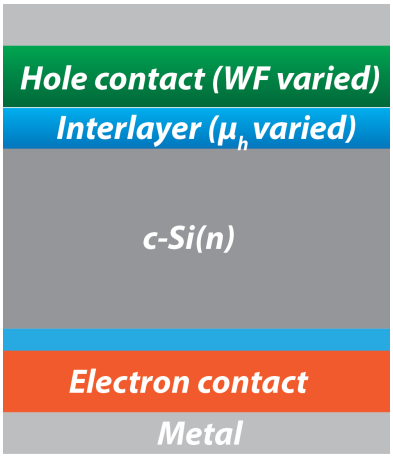

Figure 4.3.: Schematic of the cell structure used in Atlas to simulate the contact selectivity of the cell with varying interlayer μ_h and hole WF.

Table 4.1.: Atlas simulation parameters for the different layers

	Parameter	Value
c-Si(n) absorber	Thickness	180 μm
	Resistivity	5 Ohm.cm
	μ_h and μ_e	Klaassen model [23]
	SRH lifetime	3 ms
	Fermi level	4.74 eV
	Intrinsic concentration	8.6 x 10^9 cm^{-3}
	Auger lifetime	Richter model [24]
n-contact	Doping level	3x10^{20} cm^{-3}
	Thickness	100 nm
	μ_h and μ_e	10^{-3} $cm^2V^{-1}s^{-1}$
p-contact	Interlayer thickness	1.5 nm
	μ_h and μ_e	10^{-2}-10^{-8} $cm^2V^{-1}s^{-1}$
	Thickness	100 nm
	Work function	4.91 - 5.33 eV

in the simulations. The front contact, consisting of an ultrathin interlayer with limited carrier mobility, hole-selective layer with a varying work function (WF), and a metal electrode. The rear electron contact is built similarly to the hole contact but consists of optimized parameters that minimize the recombination and contact resistivity.

This model intends to simulate the effects of the surface passivating interlayers and MoO_x layer on the carrier selectivity of the hole contact. Therefore, for the sake of simplicity, we mimic the effect of MoO_x by using the properties of a p-type material based on a poly-silicon contact as shown in [26]. In this regard, the transport of holes is simplified at the hole contact and metal electrode. This assumption is only valid for comparison purposes as we focus on the study of interlayer with different WF for the hole contact layer. The doping level of the p-type hole contact is varied to account for the change in the WF of the contact. We assume the carrier mobility in the interlayer as the parameter affecting the selectivity of the hole contact [27, 28]; the hole mobility (μ_h) value characterizes the actual physical mechanism of the charge transport across the interlayer [26]. This simplified approach facilitates a meaningful comparative interpretation of the impact on majority carrier transport across the interlayers in relation to the observed loss in carrier selectivity, while avoiding unnecessary complexity introduced by incorporating different possible transport mechanisms throughout the interlayers.

Accordingly, in this study, simulations with different mobility values emulate the behavior of the device using different interlayer materials. Table 4.1 shows the values of the simulation parameters for the c-Si(n) absorber as well as the hole and electron contacts. The interlayer is modelled as a 1.5 nm c-Si(i) thick layer where μ_h is varied. Mobility values are varied between 10^{-2} to 10^{-7} $cm^2V^{-1}s^{-1}$ in this simulation work. Mobility values around 10^{-2} $cm^2V^{-1}s^{-1}$ are indicative of an interlayer with minimal transport resistance. Conversely, an exceedingly low value of 10^{-7} $cm^2V^{-1}s^{-1}$

or lower corresponds to resistances calculated for the quantum tunnelling of holes through an ideal, defect-free SiO_2 interlayer [26, 29]. The electron mobility of the interlayer is set at 10^{-5} $cm^2V^{-1}s^{-1}$ which represents electron carrier mobility for a tunneling SiO_2 and a-Si:H(i) interlayers.

4.3. RESULTS

4.3.1. INTERLAYER PASSIVATING PROPERTIES OF MoO_x CONTACTS

In this section, we investigate and compare the influence of different interlayers, i.e. a-Si:H(i), ultrathin spatial ALD Al_2O_3/SiO_y, and thermally grown SiO_2, on the surface passivation provided by the contact structures. The thickness of the thermal oxide – measured by ellipsometry – is around 1.3 nm - and the oxide layer is combined with our poly-Si contacts. In comparison, the combined thickness of the Al_2O_3/SiO_y stack is around 1.5 nm after 8 spatial ALD cycles to grow Al_2O_3. To analyze the surface passivation properties of the interlayers on our MoO_x contacts, the iV_{oc} value is monitored after the deposition of MoO_x and ITO layers, and a subsequent annealing at 190 °C, as shown in Figure 4.4. The distribution of iVoc values for each group, represented by box and whisker plots, is based on measurements from five samples per group. The MoO_x contact without an interlayer shows poor passivation which can be mainly attributed to the poor surface passivation properties of the substoichiometric oxide formed during the initial growth of the evaporated MoO_x layer [30]. However, the surface passivation of our MoO_x contacts improves by introducing the thermally grown SiO_2 and ALD grown Al_2O_3/SiO_y interlayers. On the other hand, excellent surface passivation is achieved by using an a-Si:H(i) interlayer. iV_{oc} above 700 mV is achieved after an annealing treatment at 190 °C. Subsequently, ITO layers were sputtered on the front and rear contacts. Interestingly, iV_{oc} improves for cell precursors with an Al_2O_3/SiO_y interlayer and without interlayer. In contrast, iV_{oc} decreases for precursors with SiO_2 and a-Si:H(i) interlayers due to the sputtering damage originated from the ITO deposition [31]. However, the sputtering damage can be partially recovered after an annealing treatment. Samples with an Al_2O_3/SiO_y interlayer and with no interlayer show no change in iV_{oc} after annealing at 190 °C.

4.3.2. EFFECT OF INTERLAYER PROPERTIES ON THE CARRIER SELECTIVITY OF MoO_x CONTACTS

To investigate the contact selectivity of our MoO_x contacts, we use the difference in internal and external ΔV_{oc} (ΔV_{oc} = iV_{oc}-V_{oc}) as a simple figure of merit with low values signifying a high carrier selectivity [32]. In case of low contact selectivity, the external V_{oc} of the cell is much lower than the internal V_{oc}, resulting in a high ΔV_{oc} value. This implies that the transport of majority carriers to the electrode is hindered. Note that the cell precursor used to measure the iV_{oc} and V_{oc} is shown in Figure 4.2.

Figure 4.5 shows ΔV_{oc} for different MoO_x contacts in their as-deposited states and as a function of annealing temperature. These samples were annealed in air

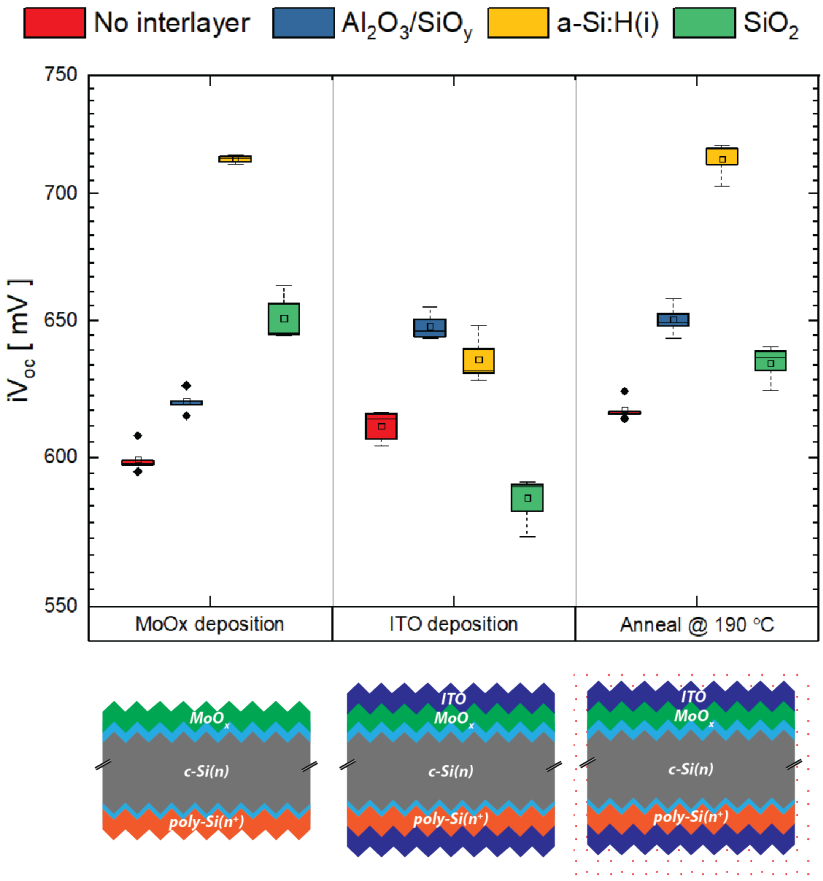

Figure 4.4.: iV_{oc} of half-fabricates after deposition of MoO_x and ITO layers, and subsequent annealing at 190 °C. Note that the order of the interlayer configurations (no interlayer, Al2O3/SiOy, a-Si:H(i), and SiO2) is consistent across all figures.

at a starting temperature of 190 °C – which represents the standard SHJ annealing conditions – followed by cumulative annealing up to 250 °C, with a 20 °C temperature step. The insertion of a-Si:H(i) and Al_2O_3/SiO_y interlayers does not affect the ΔV_{oc} prior to annealing and results in comparable ΔV_{oc} to the MoO_x/c-Si contact. In the case of a thermal SiO_2 interlayer, a high ΔV_{oc} value of about 258 mV is observed prior to annealing and no major change in ΔV_{oc} is observed after subsequent annealing. For the MoO_x/a-Si:H(i) contact, a steady increase in ΔV_{oc} from 15 to 30 mV is measured upon an increase in thermal budget, consistent with previous literature [13, 33]. This decrease in selectivity is attributed to a reduction in the induced band bending at the MoO_x contact. This reduction in band bending is likely due to a decrease in the MoO_x WF, potentially caused by hydrogen effusion from the a-Si:H(i) interlayer and/or the formation of a parasitic layer at the MoO_x/a-Si:H(i)

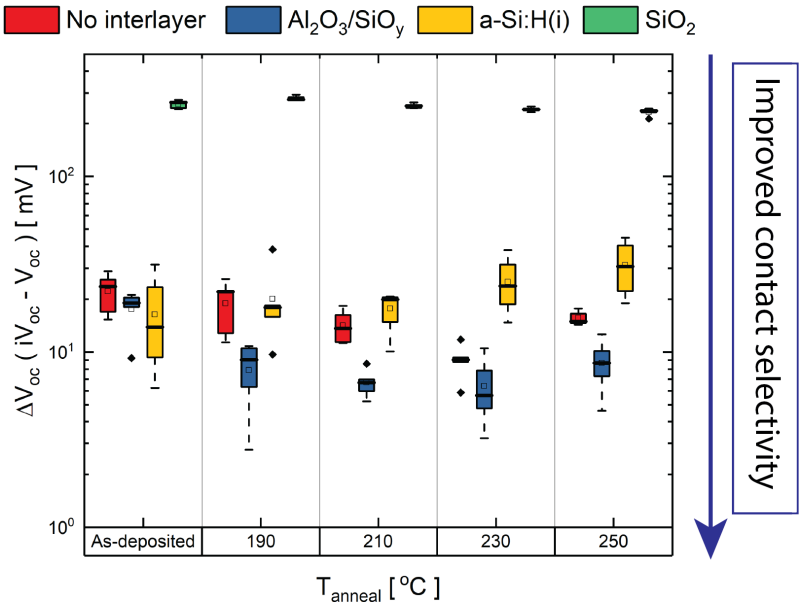

Figure 4.5.: ΔV_{oc} behavior of different MoO_x contacts as a function of cumulative annealing (190 – 250 °C)

interface [13, 33]. For the MoO_x/a-Si:H(i) contact, a steady increase in ΔV_{oc} from 15 to 30 mV is measured upon an increase in thermal budget, corresponding to results already presented in literature;[13, 33] the decrease in induced band bending provided by the MoO_x contact causes a loss in asymmetric carrier concentration near the Si absorber. In comparison, the contact selectivity of the $MoO_x/Al_2O_3/SiO_y$ contact improves upon annealing at 190 °C and remains stable after further increases in annealing temperature; an average ΔV_{oc} of about 5 mV is measured after an annealing treatment at 230 °C with a slight increase observed following annealing at 250 °C.

4.3.3. EFFECTS OF PASSIVATING INTERLAYERS ON *IV* CHARACTERISTICS

In this section, we investigate the influence of the passivating interlayers on the light IV parameters. The light IV curve and characteristics of the solar cells are shown in Figure 4.6 and Table 4.2. As expected, a MoO_x/a-Si:H(i) contact results in a high V_{oc} due to the excellent surface passivation of the a-Si:H(i) interlayer but is limited by the contact selectivity loss after annealing. On the other hand, while ultrathin Al_2O_3/SiO_y and SiO_2 interlayers have shown a similar effective surface recombination velocity (S_{eff}) (based on iV_{oc}), the high carrier selectivity loss of the MoO_x/SiO_2 contact results in a much lower V_{oc} and FF in comparison to the $MoO_x/Al_2O_3/SiO_y$ contact. Finally, solar cells with a-Si:H(i) and Al_2O_3/SiO_y interlayers at the hole

contact result in comparable conversion efficiencies just above 18 %; the J_{sc} and FF values are higher for the $MoO_x/Al_2O_3/SiO_y$ contact due to superior transparency and carrier selectivity, respectively.

4.3.4. INTERLAYER TRANSPORT: TEMPERATURE-DEPENDENT DARK IV

Further insights to explain the difference in ΔV_{oc} associated with different oxide interlayers can be acquired by performing a temperature-dependent dark IV analysis. Series resistance (R_s) is extracted from the 2-diode model for temperatures in the 25 – 65 °C range for the SiO_2 and Al_2O_3/SiO_y interlayers, as shown in Figure 4.7. The carrier transport across the interlayer can either occur by tunneling or by thermionic emission. An indirect measurement of the band offsets between the c-Si and the interlayer can be made by extracting the activation energy (E_a) from the slope of the temperature-dependent series resistance R_s by assuming an Arrhenius dependency [34]. As a result, we obtain E_a values of 117 meV and 2390 meV for the $MoO_x/Al_2O_3/SiO_y$ and MoO_x/SiO_2 contacts, respectively. E_a of the Al_2O_3/SiO_y interlayer is considerably lower than the thermally grown oxide which indicates that an inefficient hole carrier transport exists for the thermally grown SiO_2 interlayer. To further determine the effect of hole majority transport on the carrier selectivity of the contact, we simulated the effect of the interlayer hole mobility and contact WF on the hole contact properties.

4.3.5. SIMULATION OF HOLE CONTACT

EFFECT OF SURFACE PASSIVATION ON THE CARRIER SELECTIVITY

In this section, the influence of the surface recombination properties and μ_h properties of the interlayer on the carrier selectivity are simulated with respect to varying hole contact WF. We first investigate the influence of the surface recombination properties of the interlayer on the hole selectivity. Figure 4.8 (a) and (b) show the simulated results of the dependence of the hole selectivity on S_{eff}, contact WF, and μ_h. As expected, a lower hole contact WF leads to a loss in ΔV_{oc} due to a decreased hole concentration near the interface. The decrease in concentration elevates the hole resistance (R_h) across the contact, which is inversely proportional to the both carrier concentration and the hole mobility [27]. Additionally, S_{eff} of the interlayer has a significant influence on the ΔV_{oc} of the contact, particularly for interlayers with low mobility (μ_h = 10^{-7}

Table 4.2.: Measured IV characteristics for solar cells with different interlayers and without an interlayer.

Passativing interlayer	J_{sc} [mA/cm^2]	V_{oc} [mV]	FF [%]	η [%]
No interlayer	36.9	610	72.1	16.2
Al_2O_3/SiO_y	36.9	651	75.6	18.2
a-Si:H(i)	36.2	679	73.8	18.1
SiO_2	35.2	440	34.6	5.4

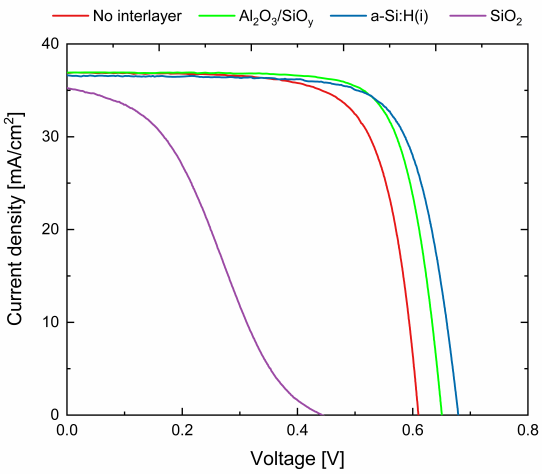

Figure 4.6.: Influence of passivating a-Si:H(i), Al_2O_3/SiO_y, and SiO_2 interlayers on the light IV characteristics of the MoO_x contacts and different interlayers.

$cm^2V^{-1}s^{-1}$). Interestingly, an increase in ΔV_{oc} is observed with decreasing S_{eff}. This counterintuitive behavior can be explained by the competing contributions of hole resistance within the interlayer ($R_{h,\ int}$) and the absorber ($R_{h,\ abs}$), as highlighted by Onno et al. [35]. ΔV_{oc} depends on both components, and the relationship is

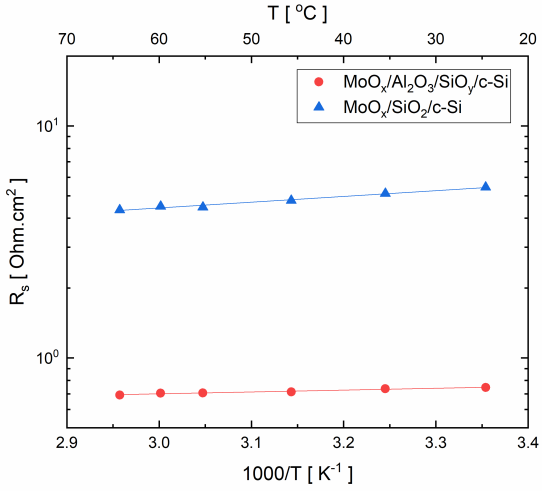

Figure 4.7.: Dark JV measurements were used to extract R_s as a function of cell temperature (25-65 °C). The fitted lines are used to calculate the activation energy.

described by:

$$\Delta V_{oc} = (J_{r,surf} + J_{r,m}) R_{h,\ abs} + J_{r,m} R_{h,\ int} \tag{4.1}$$

where $J_{r,\ surf}$ and $J_{r,m}$ are recombination current density at the Si surface and metal contact, respectively. Consequently, for an interlayer with $\mu_h = 10^{-7}$ $cm^2V^{-1}s^{-1}$, decreasing S_{eff} shifts the recombination dominance towards the surface, increasing $J_{r,\ surf}$ at the expense of $J_{r,\ m}$.

EFFECT OF INTERLAYER HOLE MOBILITY ON THE CARRIER SELECTIVITY

Figure 4.9 (a) and (b) show the simulated interacting effect of μ_h and contact WF on the cell ΔV_{oc} and FF, respectively. S_{eff} of the contact was set to 33 cm/s (as shown in Appendix B) which approximately represents the surface passivation of the MoO_x contacts with Al_2O_3/SiO_y and SiO_2 interlayers. At WF > 5.25 eV, ΔV_{oc} is minimal since the majority concentration is high enough which effectively reduces $R_{h,abs}$ (referring to Equation 1), even for a interlayer with low mobility ($\mu_h = 10^{-7}$ $cm^2V^{-1}s^{-1}$). This reduction in $R_{h,abs}$ allows for efficient hole extraction, minimizing recombination losses and maintaining a high V_{oc}, even with less optimal interlayer transport properties. However, for this high WF a steep decrease in FF is noted at $\mu_h = 10^{-7}$ $cm^2V^{-1}s^{-1}$. At moderate WF (5.1 – 5.2 eV), noticeable selectivity and FF losses are observed with a strong dependence on μ_h; a decrease in μ_h of the interlayer yields higher ΔV_{oc} and FF losses. However, at WF < 5.1 eV, contact selectivity cannot be maintained anymore even for high μ_h of the interlayer. The simulation results indicate that for both the SiO_2 and Al_2O_3 interlayers the MoO_x WF in the range of 5.1-5.2 eV is found. This estimation is supported by the close agreement between the simulated Voc values and the experimental measurements presented in 4.5(a) and 4.9(a), respectively. The moderate WF range is defined as the values where a good selectivity can be achieved with sufficient hole mobility

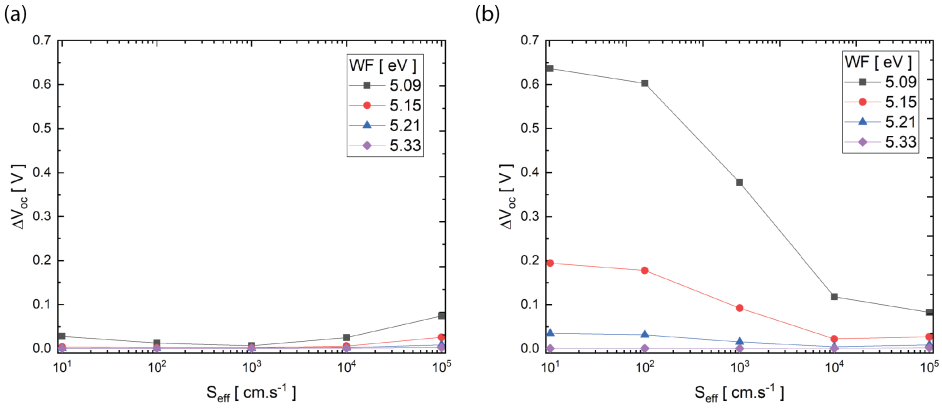

Figure 4.8.: Simulated ΔV_{oc} as a function of S_{eff} for hole contact shown for WF varying from 5.09 to 5.33 eV, and for μ_h of (a) 10^{-5} $cm^2V^{-1}s^{-1}$ and (b) 10^{-7} $cm^2V^{-1}s^{-1}$.

provided by the interlayer. The significantly high ΔV_{oc} and FF losses, measured for our MoO_x/SiO_2/c-Si(n) contact, suggest that the SiO_2 interlayer corresponds to a μ_h in the vicinity of 10^{-7} - 10^{-8} $cm^2V^{-1}s^{-1}$. This observation is consistent with the characteristics of the thermal SiO_2 interlayer and supports the proposed mobility for a defect-free SiO_2 interlayer, with a thickness ranging from 1.1 to 1.5 nm [26]. On the other hand, the evident reduction in both ΔV_{oc} and FF within our MoO_x/a-Si:H(i)/c-Si(n) contact, as influenced with by an elevated thermal budget treatment, exhibits a good correlation with an interlayer mobility of about 10^{-5} $cm^2V^{-1}s^{-1}$ or slightly higher. Finally, the good ΔV_{oc} and FF values obtained with the $MoO_x/Al_2O_3/SiO_y$ stack implies that the interlayer presents minimal resistance to hole carriers, and likely possesses a high μ_h value of about 10^{-2} $cm^2V^{-1}s^{-1}$.

To investigate the impact of μ_h on recombination losses and cell efficiency, we analysed the simulated JV curves and recombination current distributions. 4.10(a) and (b) depict the simulated JV curves and recombination current densities at the p- and n-contacts, and within the absorber (bulk) for μ_h values of 10^{-5} and 10^{-7} $cm^2V^{-1}s^{-1}$, respectively, at a hole contact WF of 5.21 eV. At μ_h = 10^{-5} $cm^2V^{-1}s^{-1}$, the total current (extracted current minus recombination current) follows a diode-like behaviour, resulting in a high FF. Here, recombination within the bulk absorber is the primary efficiency-limiting factor. However, when μ_h is reduced to 10^{-7} $cm^2V^{-1}s^{-1}$, the FF decreases significantly, and the JV curve exhibits an S-shape. This indicates that while bulk recombination remains dominant, it no longer follows a simple diode behaviour. The high R_h at the low-mobility interlayer impedes hole transport, forcing the majority hole carriers holes to recombine within the c-Si bulk, as shown by the J_r in 4.10(b).

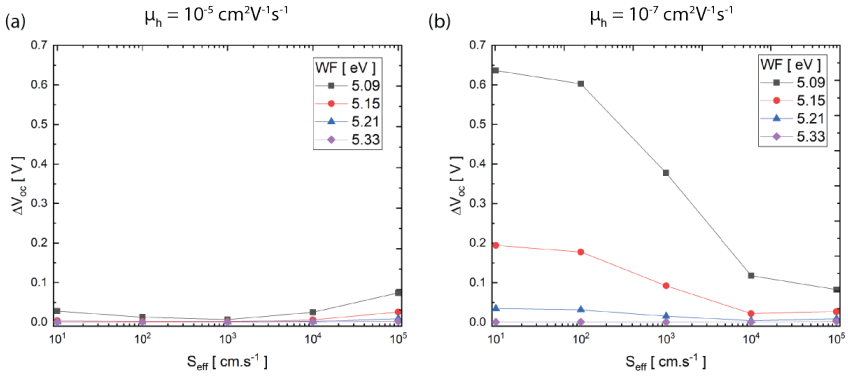

Figure 4.9.: Simulated effect of varying μ_h (10^{-2} – 10^{-7} $cm^2V^{-1}s^{-1}$) and hole WF contact (4.92 – 5.34 eV) (a) on ΔV_{oc}, (b) and on FF. S_{eff} is set to 33 cm/s which is representative of the passivation of Al_2O_3/SiO_y and SiO_2 interlayers with a MoO_x contact. Electron mobility of the interlayer is set to 10^{-5} $cm^2V^{-1}s^{-1}$.

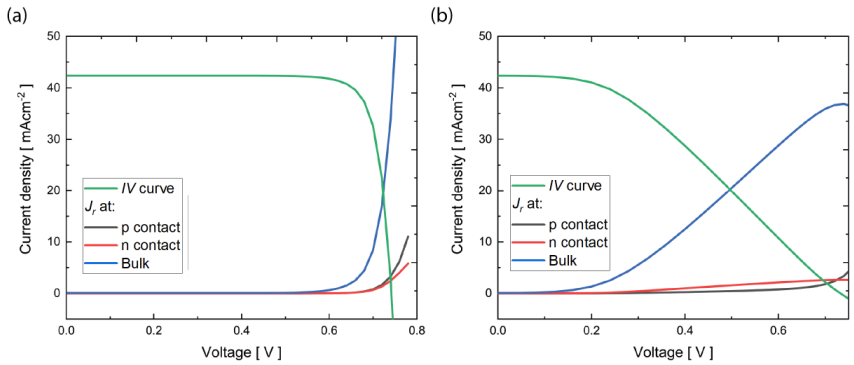

Figure 4.10.: Simulated JV curves, and recombination currents at the p- and n- contact, and in the absorber (bulk) as a function of cell voltage, for μ_h of (a) 10^{-5} and (b) 10^{-7} $cm^2V^{-1}s^{-1}$.

4.4. DISCUSSION

While the mobility model employed in this study simplifies carrier transport across the MoO_x contacts, it is essential to acknowledge the complexity of the actual contacts. In reality, several transport mechanisms, such as thermionic emission, band-to-band tunneling, and trap-assisted tunneling, exist at the interfaces of the MoO_x contacts. Additionally, the influence of the TCO layer and interlayer formation at the interfaces were not considered in this model, potentially introducing additional transport limitations. Nevertheless, as a comparative study, the presented model proves valuable in discerning differences in observed selectivity losses and recognizing the limitations imposed by the interlayers on the MoO_x contacts. The following section explains the differences in contact selectivity of the MoO_x contacts.

The combination of an a-Si:H(i) interlayer with MoO_x contact shows excellent surface passivation properties, but results in a decreasing hole selectivity with increasing annealing temperature. Several factors can contribute to this difference: (1) the degradation of induced band bending with annealing temperature which is also exacerbated by the presence of an a-Si:H(i) interlayer [33] – possibly attributed to a pronounced Fermi level pinning effect; (2) high contact resistance resulting from an intermixed oxide region formed at the interface between the MoO_x/a-Si:H(i) contact, combined with the sensitive alignment between the MoO_x conduction band and valence band of the a-Si:H(i) interlayer[36, 37]. The latter arises from the necessity of closely aligning the conduction band of the MoO_x layer with the valence band of the a-Si:H(i) layer for efficient tunneling transport [37].

By omitting the a-Si:H(i) interlayer, good contact selectivity and FF were obtained but the MoO_x/c-Si contact lacks surface passivation properties. The surface passivation and carrier selectivity of the MoO_x contact improve by inserting an ultrathin Al_2O_3/SiO_y stack, resulting in higher FF and V_{oc} values, low E_a, and improved contact thermal stability. This improvement can be attributed to the high hole mobility of approximately 10^{-2} $cm^2V^{-1}s^{-1}$ of the Al_2O_3/SiO_y interlayer which

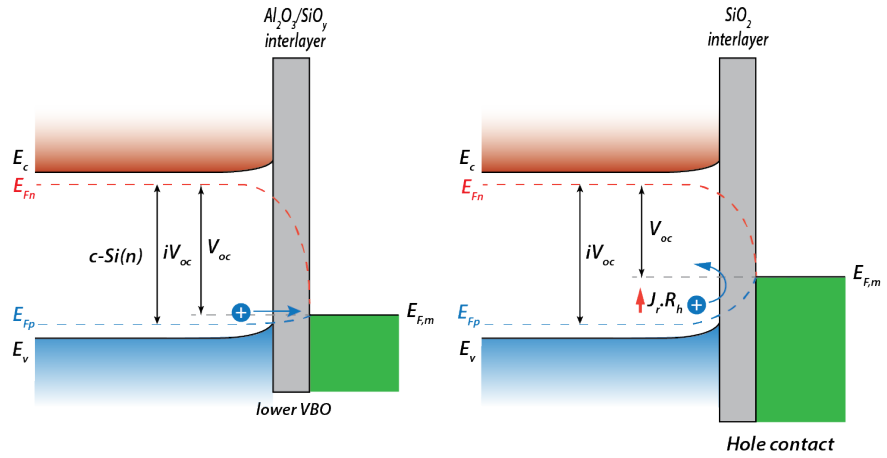

Figure 4.11.: Schematic band diagrams of hole contacts with Al_2O_3/SiO_y (left) and SiO_2 (right) interlayers, illustrating the contrasting energy barriers and hole and electron quasi-Fermi levels ($E_{Fp,n}$) alignment.

does not impede the extraction of majority hole charge carriers. This effect is linked to the amorphous and non-stoichiometric nature of the SiO_y formed at the c-Si surface, as shown in [20]. Furthermore, the considerably low E_a suggests a smaller valence band offset (VBO) between SiO_y and c-Si, thereby facilitating the transport of holes. While both thermionic emission and tunneling can contribute to carrier transport through thin oxide layers, the low E_a value for the $MoO_x/Al_2O_3/SiO_y$ contact is consistent with typical thermionic emission barriers reported for similar structures [38]. Similarly, several studies show that oxygen incorporation in a-SiOx:H interlayers result in an inefficient hole transport and consequently in an S-shaped IV curve [4, 38]. In addition, Al_2O_3/SiO_y films on c-Si substrates typically consist of high negative fixed charge properties which can promote the collection of holes as majority carriers; an inversion layer near the c-Si surface is created which increases the hole concentration. The negative fixed charge of our Al_2O_3/SiO_y film was, indeed, detected by conducting a corona charge experiment. However, further work is required to quantify the magnitude of this fixed charge of the layer due to the quick dissipation of charges after corona charge deposition. Further details can be found in Appendix B.

In comparison, a high carrier selectivity loss is apparent for the thermally grown SiO_2 interlayer although similar surface passivation properties to the Al_2O_3/SiO_y interlayer were achieved; surface passivation affects hole resistance near the c-Si surface which ultimately influences the hole selectivity [26, 35]. Additionally, the large disparity in the calculated E_a between the two interlayers suggests differences in transport mechanisms. The high E_a for SiO_2 indicates a larger energy barrier, likely hindering thermionic emission and suggesting that tunneling is the dominant transport mechanism, which is less efficient than thermionic emission. This is in contrast to the Al_2O_3/SiO_y interlayer, where the low E_a suggests a smaller barrier

resulting in a more effective thermionic emission. The observed ΔV_{oc} and FF losses of the MoO_x/SiO_2/c-Si contact are likely the result of a significantly lower interlayer μ_h in the range of 10^{-7} – 10^{-8} $cm^2V^{-1}s^{-1}$. This difference in layer mobility is likely caused by a large VBO with c-Si (4.7 eV) of the SiO_2 interlayer which creates a large barrier for holes. As a result, a significant step in the quasi-Fermi level of the holes (E_{Fp}) is introduced at the interface, as illustrated in 4.11, thereby reducing the current towards the hole contact. This step acts as an additional barrier to hole extraction, further impeding the flow of holes through the contact resulting in an increase in Jr,abs. This increases Rh,int which consequently contributes to the observed loss in carrier selectivity.

Although the contact selectivity loss can be reduced by increasing the contact WF, such high contact WF is often not feasible. In practice, a more effective approach is to enhance the interlayer mobility. For instance, in the case of poly-Si(p+) contacts, a post-deposition annealing step at high temperature is usually required for boron diffusion from the poly-Si to the SiO_2 and c-Si absorber. The increase in boron concentration in the poly-Si(p+) increases the contact WF, but also causes an increase in boron diffusion inside the Si substrate, leading to a higher defect density at the interface. Nevertheless, this post-deposition annealing step is crucial in enhancing the hole mobility across the SiO_2 interlayer; this process allows for the creation of pinholes and/or to reduce the interlayer thickness, thereby improving the transport of holes [39]. For MoO_x/SiO_2 contacts, a high temperature treatment is not viable due to the lack of thermal stability of the MoO_x layer [40].

Additionally, the thermal instability of the MoO_x contact poses challenges in implementing post-hydrogenation techniques to enhance the surface passivation at the Si/interlayer interface. Conventionally, the diffusion of hydrogen to the interface of poly-Si contacts can be achieved in several different schemes such as hydrogen-rich capping layers or a remote hydrogen plasma treatment [41, 42]. However, in the case of MoO_x contacts, similar hydrogenation techniques are challenging since the MoO_x layer interacts with hydrogen thereby degrading the WF value of the MoO_x layer [43]. The introduction of an ALD Al_2O_3 interlayer addresses some of these issues, allowing for improvement of the surface passivation without compromising on the contact selectivity. While further layer optimizations and post-deposition treatments on the Al_2O_3 interlayer can be developed to enhance the surface passivation properties, it must be ensured that these processes do not compromise the interlayer hole mobility, keeping it above 10^{-5} $cm^2V^{-1}s^{-1}$. Chapter 5 delves into the possible hydrogenation strategies to improve the surface passivation of the MoO_x contact.

4.5. CONCLUSIONS

In this work, we highlight the importance of high hole contact WF to create a strong induced band bending near the c-Si interface and the necessity of a sufficient hole mobility through the interlayer to achieve an effective hole-selective contact. An a-Si:H(i) interlayer can provide excellent surface passivation, but the MoO_x WF loss upon a thermal annealing treatment results in observable contact selectivity loss. On

the other hand, a dense, stoichiometric, thermally grown SiO_2 interlayer will cause considerable contact selectivity losses if no post-treatment is performed to improve the hole mobility. An ultrathin Al_2O_3/SiO_y interlayer provides better transparency, hole transport, and thermal stability when combined with MoO_x. This is because the sub-stoichiometric SiO_y layer does not hinder the transport of holes across the Al_2O_3/SiO_y interlayer. Hydrogenation strategies prior to the MoO_x deposition can be explored to improve the surface passivation provided by the Al_2O_3/SiO_y interlayer stack to ultimately improve the quality of MoO_x-based contacts in c-Si solar cells.

REFERENCES

[1] H. Lin, M. Yang, X. Ru, G. Wang, S. Yin, F. Peng, C. Hong, M. Qu, J. Lu, L. Fang, *et al.* "Silicon heterojunction solar cells with up to 26.81% efficiency achieved by electrically optimized nanocrystalline-silicon hole contact layers". In: *Nature Energy* (2023), pp. 1–11.

[2] Jinko Solar Holding Co. Ltd. *JinkoSolar's High-efficiency N-Type Monocrystalline Silicon Solar Cell Sets New Record with Maximum Conversion Efficiency of 26.89%*. 2023. URL: https://www.prnewswire.com/news-releases/jinkosolars-high-efficiency-n-type-monocrystalline-silicon-solar-cell-sets-new-record-with-maximum-conversion-efficiency-of-26-89-301971256.html (visited on 02/13/2024).

[3] A. Richter, R. Müller, J. Benick, F. Feldmann, B. Steinhauser, C. Reichel, A. Fell, M. Bivour, M. Hermle, and S. W. Glunz. "Design rules for high-efficiency both-sides-contacted silicon solar cells with balanced charge carrier transport and recombination losses". In: *Nature Energy* 6.4 (2021), pp. 429–438.

[4] J. Peter Seif, A. Descoeudres, M. Filipič, F. Smole, M. Topič, Z. Charles Holman, S. De Wolf, and C. Ballif. "Amorphous silicon oxide window layers for high-efficiency silicon heterojunction solar cells". In: *Journal of Applied Physics* 115.2 (2014), p. 024502.

[5] Z. C. Holman, A. Descoeudres, L. Barraud, F. Z. Fernandez, J. P. Seif, S. De Wolf, and C. Ballif. "Current losses at the front of silicon heterojunction solar cells". In: *IEEE Journal of Photovoltaics* 2.1 (2012), pp. 7–15.

[6] J. Melskens, B. W. van de Loo, B. Macco, L. E. Black, S. Smit, and W. Kessels. "Passivating contacts for crystalline silicon solar cells: From concepts and materials to prospects". In: *IEEE Journal of Photovoltaics* 8.2 (2018), pp. 373–388.

[7] L. Black, B. Van De Loo, B. Macco, J. Melskens, W. Berghuis, and W. Kessels. "Explorative studies of novel silicon surface passivation materials: Considerations and lessons learned". In: *Solar Energy Materials and Solar Cells* 188 (2018), pp. 182–189.

[8] C. Battaglia, X. Yin, M. Zheng, I. D. Sharp, T. Chen, S. McDonnell, A. Azcatl, C. Carraro, B. Ma, R. Maboudian, *et al.* "Hole selective MoO x contact for silicon solar cells". In: *Nano letters* 14.2 (2014), pp. 967–971.

[9] C. Battaglia, S. M. De Nicolas, S. De Wolf, X. Yin, M. Zheng, C. Ballif, and A. Javey. "Silicon heterojunction solar cell with passivated hole selective MoOx contact". In: *Applied Physics Letters* 104.11 (2014), p. 113902.

[10] J. Bullock, D. Yan, A. Cuevas, Y. Wan, and C. Samundsett. “N-and p-typesilicon solar cells with molybdenum oxide hole contacts”. In: *Energy Procedia* 77 (2015), pp. 446–450.

[11] L. Cao, P. Procel, A. Alcañiz, J. Yan, F. Tichelaar, E. Özkol, Y. Zhao, C. Han, G. Yang, Z. Yao, *et al.* “Achieving 23.83% conversion efficiency in silicon heterojunction solar cell with ultra-thin MoOx hole collector layer via tailoring (i) a-Si: H/MoOx interface”. In: *Progress in Photovoltaics: research and applications* (2022).

[12] J. Geissbühler, J. Werner, S. Martin de Nicolas, L. Barraud, A. Hessler-Wyser, M. Despeisse, S. Nicolay, A. Tomasi, B. Niesen, S. De Wolf, *et al.* “22.5% efficient silicon heterojunction solar cell with molybdenum oxide hole collector”. In: *Applied Physics Letters* 107.8 (2015), p. 081601.

[13] L. Neusel, M. Bivour, and M. Hermle. “Selectivity issues of MoOx based hole contacts”. In: *Energy Procedia* 124 (2017), pp. 425–434.

[14] S. W. Glunz, F. Feldmann, A. Richter, M. Bivour, C. Reichel, H. Steinkemper, J. Benick, and M. Hermle. “The irresistible charm of a simple current flow pattern–25% with a solar cell featuring a full-area back contact”. In: *Proceedings of the 31st European Photovoltaic Solar Energy Conference and Exhibition*. München WIP. 2015, pp. 259–263.

[15] M. Boccard, X. Yang, K. Weber, and Z. C. Holman. “Passivation and carrier selectivity of TiO 2 contacts combined with different passivation layers and electrodes for silicon solar cells”. In: *2016 IEEE 43rd Photovoltaic Specialists Conference (PVSC)*. IEEE. 2016, pp. 2403–2407.

[16] T. Kamioka, Y. Hayashi, Y. Isogai, K. Nakamura, and Y. Ohshita. “Effects of annealing temperature on workfunction of MoOx at MoOx/SiO2 interface and process-induced damage in indium tin oxide/MoOx/SiOx/Si stack”. In: *Japanese Journal of Applied Physics* 57.7 (2018), p. 076501.

[17] J. Tong, T. T. Le, W. Liang, M. A. Hossain, K. R. McIntosh, P. Narangari, S. Armand, T. C. Kho, K. T. Khoo, Y. Zakaria, *et al.* “Impact of Pregrown SiO x on the Carrier Selectivity and Thermal Stability of Molybdenum-Oxide-Passivated Contact for Si Solar Cells”. In: *ACS Applied Materials & Interfaces* 13.30 (2021), pp. 36426–36435.

[18] M. Bivour, B. Macco, J. Temmler, W. E. Kessels, and M. Hermle. “Atomic layer deposited molybdenum oxide for the hole-selective contact of silicon solar cells”. In: *Energy Procedia* 92 (2016), pp. 443–449.

[19] B. E. Davis and N. C. Strandwitz. “Aluminum oxide passivating tunneling interlayers for molybdenum oxide hole-selective contacts”. In: *IEEE Journal of Photovoltaics* 10.3 (2020), pp. 722–728.

[20] M. T. S. K. A. Sen, P. Bronsveld, and A. Weeber. “Thermally stable MoOx hole selective contact with Al2O3 interlayer for industrial size silicon solar cells”. In: *Solar Energy Materials and Solar Cells* 230 (2021), p. 111139.

[21] V. Naumann, M. Otto, R. B. Wehrspohn, and C. Hagendorf. “Chemical and structural study of electrically passivating Al2O3/Si interfaces prepared by atomic layer deposition”. In: *Journal of Vacuum Science & Technology A: Vacuum, Surfaces, and Films* 30.4 (2012), p. 04D106.

[22] O. Renault, L. Gosset, D. Rouchon, and A. Ermolieff. “Angle-resolved x-ray photoelectron spectroscopy of ultrathin Al 2 O 3 films grown by atomic layer deposition”. In: *Journal of Vacuum Science & Technology A: Vacuum, Surfaces, and Films* 20.6 (2002), pp. 1867–1876.

[23] D. Klaassen. “A unified mobility model for device simulation—I. Model equations and concentration dependence”. In: *Solid-State Electronics* 35.7 (1992), pp. 953–959.

[24] A. Richter, S. W. Glunz, F. Werner, J. Schmidt, and A. Cuevas. “Improved quantitative description of Auger recombination in crystalline silicon”. In: *Physical review B* 86.16 (2012), p. 165202.

[25] S. Michael, A. Bates, and M. Green. “Silvaco ATLAS as a solar cell modeling tool”. In: *Conference Record of the Thirty-first IEEE Photovoltaic Specialists Conference, 2005.* IEEE. 2005, pp. 719–721.

[26] G. Janssen, M. A. Sen, and P. Bronsveld. “a Simplified Model To Simulate Passivating & Selective Hole-Collecting Contacts”. In: *36th* (2019), pp. 2–8.

[27] U. Würfel, A. Cuevas, and P. Würfel. “Charge carrier separation in solar cells”. In: *IEEE Journal of Photovoltaics* 5.1 (2014), pp. 461–469.

[28] G. Janssen, M. Stodolny, I. Romijn, and L. Geerligs. *The role of the oxide in the carrier selectivity of metal/poly-Si/oxide contacts to silicon wafers.* Petten: ECN, 2017.

[29] F. Feldmann, G. Nogay, J.-I. Polzin, B. Steinhauser, A. Richter, A. Fell, C. Schmiga, M. Hermle, and S. W. Glunz. “A study on the charge carrier transport of passivating contacts”. In: *IEEE Journal of Photovoltaics* 8.6 (2018), pp. 1503–1509.

[30] L. G. Gerling, C. Voz, R. Alcubilla, and J. Puigdollers. “Origin of passivation in hole-selective transition metal oxides for crystalline silicon heterojunction solar cells”. In: *Journal of Materials Research* 32 (2017), pp. 260–268.

[31] B. Demaurex, S. De Wolf, A. Descoeudres, Z. Charles Holman, and C. Ballif. “Damage at hydrogenated amorphous/crystalline silicon interfaces by indium tin oxide overlayer sputtering”. In: *Applied Physics Letters* 101.17 (2012), p. 171604.

[32] M. Bivour, C. Messmer, L. Neusel, F. Zähringer, J. Schön, S. Glunz, and M. Hermle. “Principles of carrier-selective contacts based on induced junctions”. In: *33rd European PV Solar Energy Conference and Exhibition, Amsterdam, The Netherlands.* 2017, pp. 25–29.

[33] S. Essig, J. Dréon, E. Rucavado, M. Mews, T. Koida, M. Boccard, J. Werner, J. Geissbühler, P. Löper, M. Morales-Masis, *et al.* “Toward annealing-stable molybdenum-oxide-based hole-selective contacts for silicon photovoltaics”. In: *Solar Rrl* 2.4 (2018), p. 1700227.

[34] J. P. Seif, D. Menda, A. Descoeudres, L. Barraud, O. Özdemir, C. Ballif, and S. De Wolf. “Asymmetric band offsets in silicon heterojunction solar cells: Impact on device performance”. In: *Journal of Applied Physics* 120.5 (2016), p. 054501.

[35] A. Onno, C. Chen, and Z. C. Holman. “Electron and hole partial specific resistances: a framework to understand contacts to solar cells”. In: *2019 IEEE 46th Photovoltaic Specialists Conference (PVSC)*. IEEE. 2019, pp. 2329–2333.

[36] D. Sacchetto, Q. Jeangros, G. Christmann, L. Barraud, A. Descoeudres, J. Geissbühler, M. Despeisse, A. Hessler-Wyser, S. Nicolay, and C. Ballif. “ITO/MoOx/a-Si: H (i) hole-selective contacts for silicon heterojunction solar cells: degradation mechanisms and cell integration”. In: *IEEE Journal of Photovoltaics* 7.6 (2017), pp. 1584–1590.

[37] C. Messmer, M. Bivour, C. Luderer, L. Tutsch, J. Schön, and M. Hermle. “Influence of interfacial oxides at TCO/doped Si thin film contacts on the charge carrier transport of passivating contacts”. In: *IEEE Journal of Photovoltaics* 10.2 (2019), pp. 343–350.

[38] M. Liebhaber, M. Mews, T. Schulze, L. Korte, B. Rech, and K. Lips. “Valence band offset in heterojunctions between crystalline silicon and amorphous silicon (sub) oxides (a-SiOx: H, 0< x< 2)”. In: *Applied Physics Letters* 106.3 (2015), p. 031601.

[39] R. Peibst, U. Römer, Y. Larionova, M. Rienäcker, A. Merkle, N. Folchert, S. Reiter, M. Turcu, B. Min, J. Krügener, *et al.* “Working principle of carrier selective poly-Si/c-Si junctions: Is tunnelling the whole story?” In: *Solar Energy Materials and Solar Cells* 158 (2016), pp. 60–67.

[40] J. Cho, N. Nawal, A. Hadipour, M. R. Payo, A. van der Heide, H. S. Radhakrishnan, M. Debucquoy, I. Gordon, J. Szlufcik, and J. Poortmans. “Interface analysis and intrinsic thermal stability of MoOx based hole-selective contacts for silicon heterojunction solar cells”. In: *Solar Energy Materials and Solar Cells* 201 (2019), p. 110074.

[41] B. W. van de Loo, B. Macco, M. Schnabel, M. K. Stodolny, A. A. Mewe, D. L. Young, W. Nemeth, P. Stradins, and W. M. Kessels. “On the hydrogenation of Poly-Si passivating contacts by Al2O3 and SiNx thin films”. In: *Solar Energy Materials and Solar Cells* 215 (2020), p. 110592.

[42] F. Feldmann, M. Simon, M. Bivour, C. Reichel, M. Hermle, and S. W. Glunz. “Efficient carrier-selective p-and n-contacts for Si solar cells”. In: *Solar Energy Materials and Solar Cells* 131 (2014), pp. 100–104.

[43] M. T. Greiner, L. Chai, M. G. Helander, W.-M. Tang, and Z.-H. Lu. “Metal/metal-oxide interfaces: how metal contacts affect the work function and band structure of MoO3”. In: *Advanced Functional Materials* 23.2 (2013), pp. 215–226.

5

NOVEL PASSIVATING OXIDE INTERLAYER FORMED BY AL_2O_3 ETCHING FOR MOO_X HOLE-SELECTIVE CONTACT

As it can be recalled from Chapter 3, the cell efficiency of MoO_x hole-selective contact is limited by the surface passivation provided by the ultra-thin Al_2O_3/SiO_y interlayer. Although several post-hydrogenation methods exist to improve the surface passivation of an oxide interlayer, these processes are not suitable for MoO_x contacts and result in the electrical properties degradation of the contact. In order to improve the surface passivating quality of our MoO_x contact, a process to form a hydrogenated SiO_y interlayer is developed by selectively etching an atomic layer deposited (ALD) Al_2O_3 film by using a tetramethylammonium hydroxide (TMAH) solution. Al_2O_3 deposited on Si results in the natural formation of an ultra-thin SiO_y interlayer at the Si interface. After a post-deposition anneal (PDA) treatment, the hydrogen contained in the Al_2O_3 film is allowed to diffuse towards the SiO_y/Si interface and thereby provides excellent chemical surface passivation. By etching the Al_2O_3 film, an ultrathin passivating SiO_y interlayer can be obtained and used as a tunneling interlayer. After subsequent MoO_x deposition, excellent surface passivation is obtained on our newly formed MoO_x/SiO_y contact with an implied open circuit voltage (iV_{oc}) of up to 712 mV on a symmetric 6" textured Si substrate. Nevertheless, the etching conditions should be further optimized to reduce the contact resistivity. So far about 1000 $m\Omega.cm^2$ has been obtained using a 1% TMAH solution for 1 min.

This chapter is has been presented at the 8th World Conference on Photovoltaic Energy Conversion, M. Ah Sen, F. M. Hashemi, J. Melksen, A. Gutjahr, A. Weeber, Hydrogenated SiOy interlayer formed by etching Al2O3 for MoOx hole-selective contact.

5.1. INTRODUCTION

Among recent advancements in crystalline silicon photovoltaics (c-Si PV), polysilicon (poly-Si) passivating contacts have rapidly emerged as a promising technology by reaching solar cell efficiency above 26% for both $n-$ and $p-$ type Si absorbers [1–3]. Poly-Si technology – often referred as TOPCon (tunneling oxide passivated contact) – has been adopted by many PV manufacturers, with several having already commenced module production [4, 5]. The main reason for the rapid adaptation of this technology can be explained by the transferable processing steps from the mainstream passivated emitter and rear cell (PERC) technology to TOPCon structures; improved efficiency with few additional processing steps and similar to mainstream technology [6]. The high efficiency of poly-Si contacts originates from the high surface passivation properties provided by the ultra-thin SiO_x interlayer and highly doped poly-Si layer. Note that the latter also allows for a low contact resistance.

To achieve a low recombination current density (J_o), a hydrogenation step is crucial to passivate the electronically active Si dangling bonds at the Si/SiO_x interface. Typically, a high temperature process (~400 °C) is used to diffuse hydrogen to the Si/SiO_x interface. The introduction of hydrogen can be achieved in various ways such as, remote hydrogen plasma [7, 8], hydrogen rich capping layers (deposited on top of poly-Si) [9], or by release of hydrogen from doped layer upon high temperature anneal. However, these hydrogenation methods are often inadequate for MoO_x layer due to the higher processing temperature; the work function (WF) of MoO_x decreases upon an increase in annealing temperature thereby reducing the hole-carrier selectivity [10].

Although excellent hole-carrier selectivity was achieved by our $MoO_x/Al_2O_3/SiO_y$ contact (as shown in chapter 3), the surface passivation provided by the oxide interlayer is insufficient to achieve a high open circuit voltage (V_{oc}). In this chapter, we explore different hydrogenation strategies for improving the surface passivation of the underlying SiO_y interlayer. Hydrogenation methods such as, spatial atomic layer deposition (sALD) of an Al_2O_3 capping layer, NH_3 plasma and H_2 rich-environment anneal will be evaluated at different steps of the manufacturing of the MoO_x contact. Additionally, the formation of a highly passivated oxide interlayer by selective etching of Al_2O_3 will be studied for a MoO_x contact.

5.2. EXPERIMENTAL DETAILS

180 μm thick M2 size n-type Cz c-Si wafers with a resistivity of ~3 Ohm.cm were textured in a KOH etching solution, followed by a $POCl_3$ diffusion and removal - as pre-gettering step, and wet chemical rounding of the pyramids. Samples that received a pre-clean treatment were dipped in an RCA 1 and 2 clean, and repeated cycles of NAOS treatments. The samples are dipped in a 1% HF bath before the Al_2O_3 deposition. The surface passivating interlayer was deposited at 200 °C with 8 cycles of sALD Al_2O_3. For hydrogenation of the contacts, 42 cycles of Al_2O_3 capping layer (~6nm) were deposited and the samples subsequently received a post deposition anneal (PDA) in N_2 for 20 min at 600 °C – unless stated otherwise. Hydrogenation by

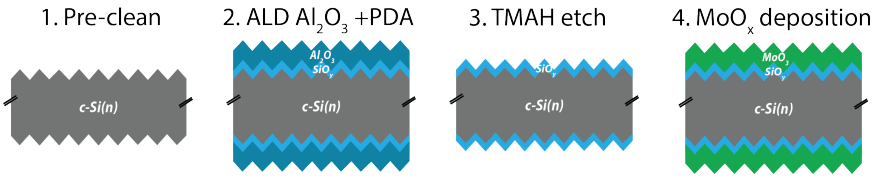

Figure 5.1.: Symmetric MoO_x/SiO_y contacts manufacturing process on 6 inch Cz *n*-type Si wafers.

NH_3 plasma and H_2 annealing environment were performed at various temperatures in a plasma enhanced chemical vapor deposition (PECVD) tool.

The Al_2O_3 layers were etched of in a diluted solution containing 1% TMAH which was heated up to the desired temperature. 5 nm thick MoO_x films were deposited by electron beam evaporation at a base pressure of 7.5 x 10^{-6} bar and at a deposition rate of 0.1 nm/s. Symmetric samples with the MoO_x/SiO_y contact stacks were manufactured as shown in 5.1. The injection dependent minority carrier lifetime of the samples was evaluated by transient photoconductance measurements using a Sinton WCT-120 setup. The effective lifetime (τ_{eff}) of the symmetric samples was measured at carrier concentration of 10^{15} cm^{-3}. The thickness of the Al_2O_3 films was determined by ellipsometry (J.A. Woollam) and measured on a polished Si substrate. *p*-type c-Si substrates with bulk resistivity of ~1 Ohm.cm were used to manufacture contact resistance samples. Contact resistance of the hole contacts were measured by vertical dark *IV*-measurement across the sample ($R_{Total} = R_{base} + 2 \times R_{contact}$).

5.3. RESULTS AND DISCUSSION

5.3.1. POST-HYDROGENATION STRATEGIES FOR MoO_X CONTACT

Conventionally, a post-hydrogenation step is required to improve the surface passivation of poly-Si contacts. Several processes at elevated temperature (~ 350 °C) can be applied to allow the diffusion of hydrogen through the poly-Si layer to the SiO_x/Si interface. The first section of this chapter investigates the effects of a conventional hydrogenation method by applying sALD Al_2O_3 capping on our MoO_x contacts. The $MoO_x/Al_2O_3/SiO_y$ contact, as previously demonstrated, shows a good hole-carrier selectivity but is limited by the surface passivation of the SiO_y interlayer. This is likely prompted by the lack of a dedicated hydrogenation step on the contact and/or mitigating x-ray induced damage originated from the e-beam MoO_x deposition. Here, we investigated the possible surface passivation limitations of our $MoO_x/Al_2O_3/SiO_y$ contact and the possibility to apply a post-hydrogenation step. An Al_2O_3 layer, deposited by sALD, is utilized as a hydrogen rich capping layer.

Various stacks, all consisting of a 8 cycles sALD Al_2O_3/SiO_y interlayer, are compared, as shown in Figure 5.2. All stacks are capped with a 6 nm thick sALD Al_2O_3 capping layer, and a post-deposition anneal (PDA) treatment in an N_2 environment at 600 °C is carried out. The stacks investigated include a reference 6 nm thick Al_2O_3/SiO_y, a $MoO_x/Al_2O_3/SiO_y$ contact, a Al_2O_3/SiO_y contact induced

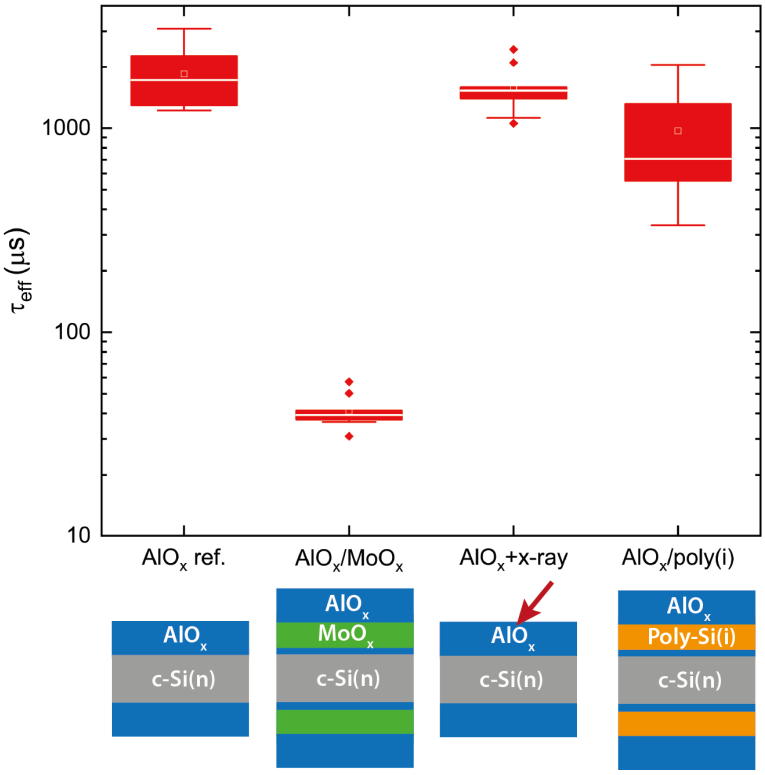

Figure 5.2.: Surface passivation comparison quality of different stacks capped with a hydrogenated Al_2O_3 capping layer, including, Al_2O_3 reference, MoO_x/ Al_2O_3/SiO_y contact, x-ray emission on Al_2O_3 interlayer, and poly-Si(i)/ Al_2O_3/SiO_y contact.

with x-rays, and an intrinsic poly-Si contact. The poly-Si contact with Al_2O_3/SiO_y interlayer was kept undoped due to the possible influence of significant in-diffusion of dopant into the Si bulk which can impact the surface passivation. To investigate the effect of x-ray induced damage by the e-beam deposition, a glass sheet is added on top the substrate to prevent MoO_x deposition while allowing x-ray emission on the Al_2O_3/SiO_y interlayer. Subsequently, Al_2O_3 was similarly deposited and annealed as was done for the reference sample.

Hydrogenated Al_2O_3 deposited on Si results in excellent τ_{eff} of ~2 ms after the PDA treatment due to its high negative fixed charged and chemical surface passivation properties. Intrinsic poly-Si/Al_2O_3/SiO_y contact shows good τ_{eff} of ~1 ms but the surface passivation is lower than the reference sample possibly because of the absence of field effect passivation provided by the instinsic poly-Si. Furthermore, this shows that the Al_2O_3/SiO_y interlayer can be used, with respect to surface

passivation, as a suitable interlayer for poly-Si contact. Al_2O_3 samples with x-ray induced damage show similar τ_{eff} as the Al_2O_3 reference sample. The negligible difference between the samples implies that the induced x-ray damage has minimal effect on the surface passivating quality of the interlayer and therefore cannot be the limiting factor for the passivation of our $MoO_x/Al_2O_3/SiO_y$ contact. This is possibly because of the low e-beam power used during the MoO_x deposition; MoO_x has a low sublimation point and therefore only requires little energy to evaporate. On the other hand, $MoO_x/Al_2O_3/SiO_y$ contact capped with a hydrogenated Al_2O_3 layer resulted in poor surface passivation after the PDA treatment. Several reasons can explain this behavior: (1) hydrogen release by the Al_2O_3 capping layer during the PDA treatment reacts with the oxygen present in the MoO_x layer thereby resulting in hydroxyl group formation [11]. Consequently, hydrogen diffusion to the Si interface is restricted while oxygen vacancies are formed in the MoO_x film which limits the surface passivation at the interface. (2) increase in oxygen deficiency of the MoO_x layer can be caused by the high thermal budget treatment [10]. This, in turn, results in a decrease in work function of the MoO_x layer which is essential to sufficient induced band bending within the c-Si absorber [12, 13]. In summary, good surface passivation can be achieved with an Al_2O_3/SiO_y interlayer when combined with a poly-Si contact. However, unlike the poly-Si contact, MoO_x layer seems to act as a hydrogen capping layer which prevents hydrogen diffusion to the Si interface. This is likely caused by an interaction of oxygen contained the MoO_x layer and the released hydrogen from the Al_2O_3 capping layer occurring during the post-annealing deposition treatment.

5.3.2. PRE-HYDROGENATION PROCESSES ON SiO_Y PASSIVATING INTERLAYER

HYDROGENATION BY H_2 ANNEALING ENVIRONMENMT AND NH_3 PLASMA

This section investigates the possible application of incorporating hydrogen to the oxide interlayer prior to MoO_x deposition. This is performed to avoid direct exposure of hydrogen and higher thermal annealing on the sensitive MoO_x layer. NH_3 plasma and annealing in a H_2 rich environment are used as a method to hydrogenate the oxide interlayer. Figure 5.3(a) and (b) show iV_{oc} as a function of processing temperature for NH_3 and H_2 hydrogenation treatment, respectively. NH_3 plasma, at hydrogenation temperature range between 175 – 450 °C, slightly improves the surface passivation of the oxide interlayer; optimal iV_{oc} is obtained after NH_3 hydrogenation temperature at 375°C. The passivation of the oxide improves with H_2 annealing temperature but is less effective than NH_3 plasma. After MoO_x deposition, the passivation of the contact increases due to the field-effect passivation provided by the MoO_x layer. iV_{oc} above 650 mV is achieved for a NH_3 hydrogenated oxide at 375°C. In comparison, high iV_{oc} (~720 mV) is achieved using the same hydrogenation conditions on a poly-Si(n+)/SiO_x contact. It is likely caused by the capping properties of poly-Si layer which is able to retain the hydrogen at the Si interface. On the other hand, when NH_3 hydrogenation is applied solely on the ultra-thin oxide, the hydrogen cannot be retained and thereby high surface

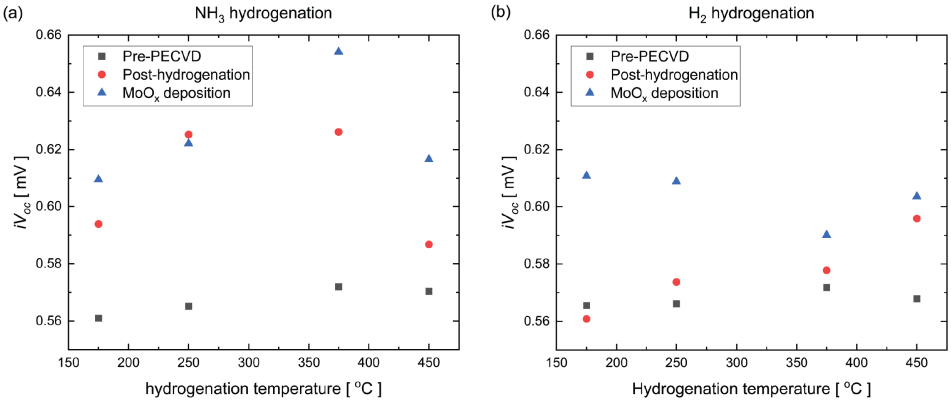

Figure 5.3.: iV_{oc} as a function of processing temperature for hydrogenation by (a) NH_3 plasma and (b) annealing in an H_2 environment on the ultra-thin oxide prior to, and after MoO_x deposition.

5

passivation quality cannot be achieved after MoO_x deposition. In the next section, we explore the possibility to effective incorporate hydrogen to the oxide interlayer by using Al_2O_3 layer as hydrogen source.

5.3.3. SiO_Y:H INTERLAYER BY Al_2O_3 ETCHING

Here, we explore an alternative strategy to form a passivating oxide interlayer prior to MoO_x deposition. This method intends to utilize the highly passivating SiO_y:H layer, which is naturally formed between the Si and Al_2O_3 interface, as an interlayer for our MoO_x contact. This is performed by selective etching of Al_2O_3 bulk layer in a TMAH solution without significantly damaging the oxide interlayer. Several parameters are varied, such as pre-cleaning substrate treatments, TMAH etching conditions, Al_2O_3 deposition and PDA temperature conditions to achieve good selective etching of the bulk layer.

TMAH ETCHING CONDITIONS

Firstly, we investigate the effects of the TMAH etching temperature (T_{etch}) and sALD deposition temperature (T_{dep}) on the etching rate in a 1% diluted TMAH solution of Al_2O_3 films. Table 5.1 shows the thickness of the Al_2O_3 layers after a TMAH etch at 40 °C and 60 °C, and for 30 s and 60 s for Al_2O_3 layers deposited at 100 and 200 °C. Al_2O_3 films, deposited at 100 °C, etch faster than the Al_2O_3 films deposited at 200 °C which is likely caused by the dependence of Al_2O_3 layer density on T_{dep} [14]. However, both films are completely etched away after 60 s in the TMAH bath at 60 °C. On the other hand, Al_2O_3 layer deposited at 200 °C, and etched at a temperature of 40 °C, shows a slower etching rate resulting in a total thickness of 10.4 nm after 60 s. Note that the SiO_y interlayer is hardly etched by the TMAH solution. The SiO_y

Table 5.1.: Thickness of sALD Al_2O_3 - excluding the SiO_y interlayer, etched in diluted TMAH solution at 40 °C and 60 °C. The Al_2O_3 films were deposited at 100 and 200 °C followed by a PDA at 600 °C.

Al_2O_3 T_{dep} [°C]	100 °C			200 °C	
Etching temperature/time	0 s	30 s	60 s	0 s	60 s
60 °C	11.4 nm	0 nm	0 nm	15.3 nm	0 nm
40 °C	11.9 nm	3.9 nm	0 nm	16.8 nm	10.4 nm

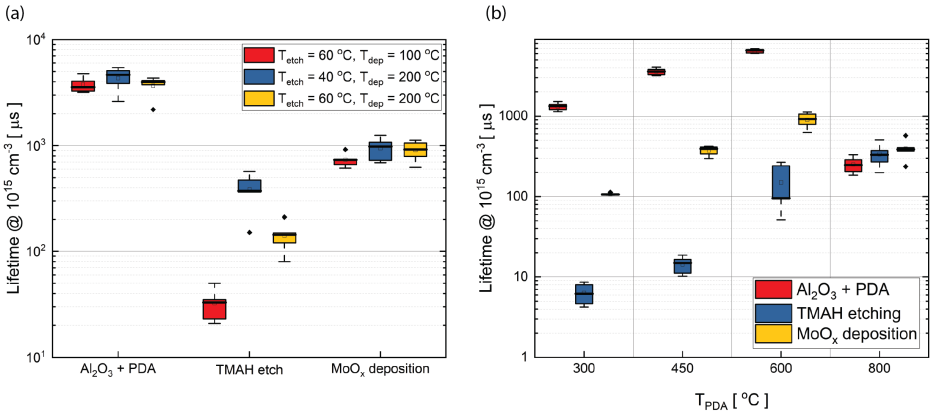

Figure 5.4.: (a) Effective lifetime comparison of Al_2O_3 films deposited at 100 °C and 200 °C and annealed at 600 °C are etched in a TMAH solution after which MoO_x is deposited. The effect of the etching bath temperature at 40 °C and 60 °C are also compared. (b) Effect of T_{PDA} between 300 to 800 °C on the surface passivation of MoO_x/SiO_y contact.

interlayer is about 1.2 nm thick after etching– as measured by ellipsometry – and is in the range for effective tunneling transport.

Subsequently, the effects of T_{etch} and T_{dep} on the surface passivating quality of newly exposed SiO_y interlayer are probed. Figure 5.4(a) shows the τ_{eff} of Al_2O_3 films after a PDA treatment at 600 °C, followed by TMAH etching, and post-MoO_x deposition. Excellent τ_{eff} is initially obtained for both Al_2O_3 films deposited at 100 °C and 200 °C. After Al_2O_3 etching, τ_{eff} decreases which is likely caused by an absence of the field effect passivation; the origin of the negative fixed charge provided by Al_2O_3 films is present within ~1 nm from the Si interface [15]. Additionally, the decrease in passivation quality can be also caused by some etching damage on the SiO_y interlayer which subsequently reduces the chemical passivation of the interlayer. The surface passivation quality of the contacts improves after MoO_x deposition due the induced band bending provided by the MoO_x layer. While some difference in τ_{eff} is observed after etching, the varying T_{etch} and T_{dep} conditions result in similar level of surface passivation properties after MoO_x deposition.

The surface passivation and hole-carrier transport across the interlayer are highly

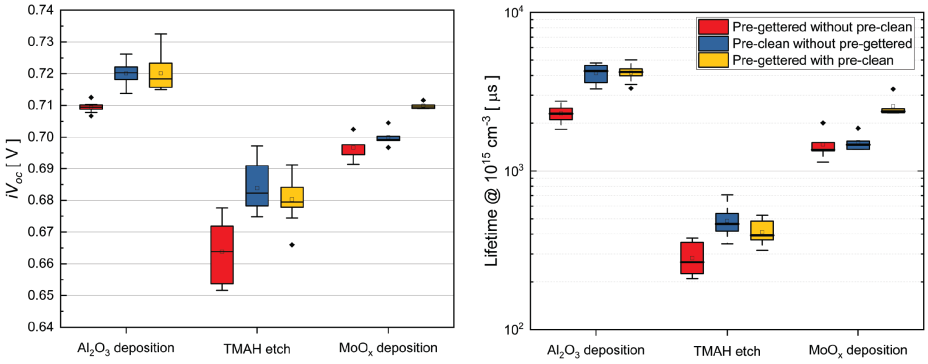

Figure 5.5.: Effect of pre-gettering and pre-clean on the iV_{oc} (left) and τ_{eff} (right) of MoO_x/SiO_y contact.

5

dependent on the PDA temperature (T_{PDA}) as its influences the formation of the SiO_y interlayer and effective hydrogen diffusion to the interface (as shown in Chapter 3). As a result, the effect of Al_2O_3 T_{PDA} variation (between 300 and 800 °C) on the τ_{eff} of the MoO_x/SiO_y contact is investigated, as depicted in Figure 5.4(b). An optimal surface passivation with Al_2O_3 layer is achieved at T_{PDA} = 600 °C with τ_{eff} above 6 ms, after the PDA treatment. After Al_2O_3 etching and MoO_x deposition, similar trend in τ_{eff} is observed. As a result, optimal surface passivation of MoO_x/SiO_y contact is, therefore, obtained at T_{PDA} = 600 °C. The optimal T_{PDA} obtained is likely caused by a balance between hydrogen supply to the SiO_y/Si interface and the de-passivation of defects that occurs at elevated temperatures [14]. Additionally, it has to be noted that the optimal T_{PDA} is dependent on the Al_2O_3 film properties such as, deposition conditions, and film thickness.

To further improve the surface passivation quality of the MoO_x/SiO_y contact, several pre-cleaning treatments are explored on the c-Si substrate, prior to SiO_y deposition. Figure 5.5 shows the effect of the pre-clean and pre-gettering prior to the Al_2O_3 deposition on the surface passivation of the MoO_x/SiO_y contact. A pre-clean – typically used prior to a-Si:H layer depositions – improves the surface passivation provided by the Al_2O_3 layer. Pre-gettering shows no influence in surface passivation after the PDA treatment. However, after the Al_2O_3 layer is etched and MoO_x is deposited, the lifetime of samples that were pre-gettered and received a pre-clean are significantly higher and yield excellent passivation with τ_{eff} = 2.3 ms and iV_{oc} = 709 mV on average for the MoO_x/SiO_y contact. The high level of surface passivation quality indicates that the etch process is not significantly damaging to the interlayer.

5.3.4. CONTACT RESISTIVITY

In this section, the contact resistivity of the contact is investigated. Figure 5.6 shows the contact resistivity (ρ_c) measurements, with respect to annealing temperature of

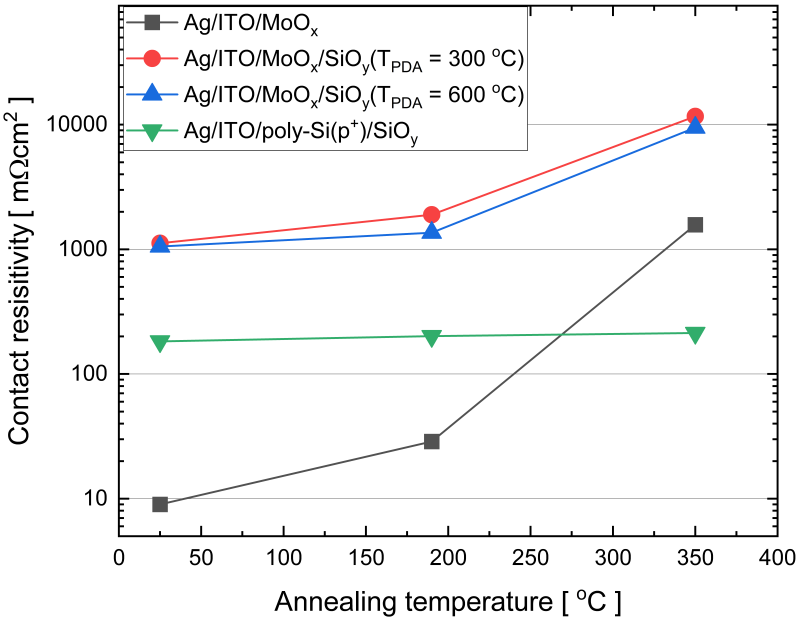

Figure 5.6.: Contact resistivity measurements of MoO_x, MoO_x/SiO_y with PDA treatment at 300 and 600 °C, and poly-Si/SiO_y contacts as a function of annealing temperature. *p*-type c-Si substrates were similarly textured and pre-clean prior to stacks formation.

a reference MoO_x contact without any pre-interlayer formation, poly-Si(p+)/SiO_y contact, and MoO_x contacts with SiO_y interlayer with a PDA treatment at 300 and 600 °C. As-deposited MoO_x contact shows excellent contact resistivity (below 10 mΩ.cm^2) and has also been previously shown by Bullock et al.[16]. Nevertheless, ρ_c increases with annealing temperature and results in a ρ_c > 1000 mΩ.cm^2, after an anneal at 350 °C. This effect is typcailly caused by a decrease in induced band-bending at the MoO_x/Si interface which in turn decreases the hole-carrier selectivity of the MoO_x contact [17]. MoO_x contacts with SiO_y interlayer annealed at 300 and 600 °C show high ρ_c prior to anneal, and surprisingly minor difference in ρ_c is observed between the contacts; an increase in carrier selectivity loss was observed with increase in T_{PDA} in Chapter 3 which corresponds to an increase in stoichiometry configuration of the SiO_y layer, as measured by XPS. The high ρ_c of the MoO_x/SiO_y contacts suggest that the interlayers significantly impede the transport of hole carriers and ought to be improved. In comparison, poly-Si(p+) contact displays a acceptable ρ_c of about 200 m Ω.cm^2 even after anneal at 350 °C. While a similar interlayer was utilized for the MoO_x and poly-Si contacts, the oxide interlayer was prompted to a

high temperature process required (900 °C) for the crystallization of the a-Si:H(p+) layer. This, in turn, allows for diffusion of dopant, formation of pinholes, and thinning of the interlayer occurring during the high temperature treatment which facilitate the transport of hole-carriers across the interlayer [18]. Several reasons could hamper the transport of hole carriers through the SiO_y interlayer. Further work to improve the majority carrier tunneling transport can be attained by reducing the thickness of the interlayer. It can be possibly achieved by precisely etching the SiO_y interlayer in a higher TMAH concentration. Tetzalaff et al .[19] showed that SiO_2 etches at a rate of about 0.1 nm/min in a 5% diluted TMAH solution. Nevertheless, prolonged etching could also impact the surface passivating quality of the interlayer and is ought to be considered.

5.4. CONCLUSIONS

Conventional hydrogenation methods on SiO_y interlayer are often inadequate for low-temperature contacts, such as MoO_x due to the interaction with hydrogen causing loss of contact selectivity. To overcome this limitation, Al_2O_3 was selectively etched exposing the underlaying passivating SiO_y interlayer. After subsequent MoO_x deposition, high iV_{oc} up to 712 mV was achieved on commercial size Si wafers. T_{etch} and T_{dep} of Al_2O_3 layer shows no influence on the passivation of the contact while a pre-clean is required to further improve the passivation. The oxide interlayer hinders the transport of hole majority carrier and should be improved to allow for low ρ_c values. Achieving this necessitates dedicated and extended TMAH etching optimizations to further diminish the thickness of the SiO_y interlayer, all while preserving surface passivation and enabling efficient majority carrier transport across the oxide interlayer.

REFERENCES

[1] A. Richter, J. Benick, R. Müller, F. Feldmann, C. Reichel, M. Hermle, and S. W. Glunz. “Tunnel oxide passivating electron contacts as full-area rear emitter of high-efficiency p-type silicon solar cells”. In: *Progress in Photovoltaics: Research and Applications* 26.8 (2018), pp. 579–586.

[2] F. Haase, C. Hollemann, S. Schäfer, A. Merkle, M. Rienäcker, J. Krügener, R. Brendel, and R. Peibst. “Laser contact openings for local poly-Si-metal contacts enabling 26.1%-efficient POLO-IBC solar cells”. In: *Solar Energy Materials and Solar Cells* 186 (2018), pp. 184–193.

[3] JinkoSolar Holding Co. Ltd. *JinkoSolar’s High-efficiency N-Type Monocrystalline Silicon Solar Cell Sets Our New Record with Maximum Conversion Efficiency of 26.4%*. 2022. URL: https://www.prnewswire.com/news-releases/jinkosolars-high-efficiency-n-type-monocrystalline-silicon-solar-cell-sets-our-new-record-with-maximum-conversion-efficiency-of-26-4-301700102.html (visited on 01/13/2023).

[4] V. Shaw. *JinkoSolar unveils new TOPCon solar products with record efficiency ratings*. 2023. URL: https://www.pv-magazine.com/2023/01/10/jinkosolar-unveils-new-topcon-solar-products-with-record-efficiency-ratings/ (visited on 01/13/2023).

[5] B. Santos. *Trina Solar starts producing 210 mm n-type TOPCon solar cells*. 2023. URL: https://www.pv-magazine.com/2023/01/10/trina-solar-starts-producing-210-mm-n-type-topcon-solar-cells/ (visited on 01/13/2023).

[6] B. Kafle, B. S. Goraya, S. Mack, F. Feldmann, S. Nold, and J. Rentsch. “TOPCon–Technology options for cost efficient industrial manufacturing”. In: *Solar Energy Materials and Solar Cells* 227 (2021), p. 111100.

[7] F. Feldmann, C. Reichel, R. Müller, and M. Hermle. “The application of poly-Si/SiOx contacts as passivated top/rear contacts in Si solar cells”. In: *Solar Energy Materials and Solar Cells* 159 (2017), pp. 265–271.

[8] F. Feldmann, M. Bivour, C. Reichel, H. Steinkemper, M. Hermle, and S. W. Glunz. “Tunnel oxide passivated contacts as an alternative to partial rear contacts”. In: *Solar Energy Materials and Solar Cells* 131 (2014), pp. 46–50.

[9] B. W. van de Loo, B. Macco, M. Schnabel, M. K. Stodolny, A. A. Mewe, D. L. Young, W. Nemeth, P. Stradins, and W. M. Kessels. “On the hydrogenation of Poly-Si passivating contacts by Al2O3 and SiNx thin films”. In: *Solar Energy Materials and Solar Cells* 215 (2020), p. 110592.

[10] T. Zhang, C.-Y. Lee, Y. Wan, S. Lim, and B. Hoex. “Investigation of the thermal stability of MoOx as hole-selective contacts for Si solar cells”. In: *Journal of Applied Physics* 124.7 (2018), p. 073106.

[11] M. Vasilopoulou, A. M. Douvas, D. G. Georgiadou, L. C. Palilis, S. Kennou, L. Sygellou, A. Soultati, I. Kostis, G. Papadimitropoulos, D. Davazoglou, *et al.* “The influence of hydrogenation and oxygen vacancies on molybdenum oxides work function and gap states for application in organic optoelectronics”. In: *Journal of the American Chemical Society* 134.39 (2012), pp. 16178–16187.

[12] M. T. Greiner, L. Chai, M. G. Helander, W.-M. Tang, and Z.-H. Lu. “Transition metal oxide work functions: the influence of cation oxidation state and oxygen vacancies”. In: *Advanced Functional Materials* 22.21 (2012), pp. 4557–4568.

[13] M. Bivour, S. Schröer, and M. Hermle. “Numerical analysis of electrical TCO/a-Si: H (p) contact properties for silicon heterojunction solar cells”. In: *Energy Procedia* 38 (2013), pp. 658–669.

[14] G. Dingemans, W. Beyer, M. Van de Sanden, and W. Kessels. “Hydrogen induced passivation of Si interfaces by Al 2 O 3 films and SiO 2/Al 2 O 3 stacks”. In: *Applied physics letters* 97.15 (2010), p. 152106.

[15] V. Naumann, M. Otto, R. B. Wehrspohn, and C. Hagendorf. “Chemical and structural study of electrically passivating Al2O3/Si interfaces prepared by atomic layer deposition”. In: *Journal of Vacuum Science & Technology A: Vacuum, Surfaces, and Films* 30.4 (2012), p. 04D106.

[16] J. Bullock, A. Cuevas, T. Allen, and C. Battaglia. “Molybdenum oxide MoOx: A versatile hole contact for silicon solar cells”. In: *Applied Physics Letters* 105.23 (2014), p. 232109.

[17] L. Neusel, M. Bivour, and M. Hermle. “Selectivity issues of MoOx based hole contacts”. In: *Energy Procedia* 124 (2017), pp. 425–434.

[18] R. Peibst, U. Römer, Y. Larionova, M. Rienäcker, A. Merkle, N. Folchert, S. Reiter, M. Turcu, B. Min, J. Krügener, *et al.* “Working principle of carrier selective poly-Si/c-Si junctions: Is tunnelling the whole story?” In: *Solar Energy Materials and Solar Cells* 158 (2016), pp. 60–67.

[19] D. Tetzlaff, M. Dzinnik, J. Krügener, Y. Larionova, S. Reiter, M. Turcu, R. Peibst, U. Höhne, J.-D. Kähler, and T. F. Wietler. “Introducing pinhole magnification by selective etching: application to poly-Si on ultra-thin silicon oxide films”. In: *Energy Procedia* 124 (2017), pp. 435–440.

6

SOFT DEPOSITION OF TCOS BY PULSED LASER FOR HIGH-QUALITY ULTRA-THIN POLY-SI PASSIVATING CONTACTS

In this work, the applicability of pulsed laser deposition (PLD) of transparent conductive oxides (TCOs) on high-quality ultra-thin poly-Si based passivating contacts is explored. Parasitic absorption caused by poly-Si layers can be minimized by reducing the poly-Si layer thickness. However, TCO deposition on poly-Si contacts, commonly by sputtering, results in severe deposition-induced damage and further aggravates the surface passivation for thinner poly-Si layers (<20 nm). Although a thermal treatment at elevated temperature (~350 °C) can be used to partially repair the surface passivation quality, the contact resistivity severely increases due to the formation of a parasitic oxide layer at the poly-Si/ITO interface. Alternatively, we show that PLD TCOs can be used to mitigate the damage on ultra-thin (~10 nm) poly-Si layers. Further improvement in poly-Si contact passivation can be achieved by increasing the deposition pressure while low contact resistivities (45 mΩcm^2) and good thermal stability (up to 350 °C) are achieved with a PLD indium-doped tin oxide (ITO) layer on high-quality ultra-thin poly-Si(n+) contacts. This allows for the application of a highly transparent front side contact by combining the excellent opto-electrical properties of a PLD ITO film with a 10 nm thin poly-Si contact.

This chapter is based on an article published by M. Ah Sen, A. Mewe, J. Melskens, J. Bolding, M. Van de Poll, A. Weeber, "Soft deposition of TCOs by pulsed laser for high-quality ultra-thin poly-Si passivating contacts" Journal of Applied Physics, 134(15), doi:10.1063/5.0158681 [1]. Special mentioned to Fatemeh Minaye Hashemi for her immense contribution.

6.1. INTRODUCTION

Poly-Si passivating contacts have been extensively explored in recent years, enabling a record solar cell conversion efficiency of 26.4% in combination with a front side diffused emitter cell architecture [2]. This solar cell structure is limited by the front emitter recombination loss [3]. These recombination losses can be reduced by using a front and rear passivating contacts approach, and hence allowing for a better overall surface passivation quality. The drawback of poly-Si passivating contacts, when used at the front side of a solar cell, is the parasitic absorption caused by the high dopant concentration in the relatively thick contact materials. While the parasitic absorption losses can be mitigated by reducing the poly-Si layer thickness to below 20 nm, a transparent conductive oxide (TCO) layer is necessary to provide lateral conductivity for charge carrier transport to the metal grid. However, the subsequent deposition of a TCO film on poly-Si layers normally results in a drop in surface passivation properties of the cell. Another option to reduce the parasitic absorption will be to apply a lower dopant concentration. However, that will reduce the field effect and overall passivation quality. In the end it will be better to work on the application of thinner poly-Si layers to mitigate parasitic absorption losses.

TCOs are typically deposited by sputtering which reduces the surface passivation quality of the contacts and has been generally reported for silicon heterojunction (SHJ) solar cells based on amorphous silicon layers [4]. Nevertheless, the sputtering-induced damage on SHJ solar cells can be recovered after a low-temperature annealing treatment (~200 °C) [5], which is also an essential process to enable a good contact between the TCO and screen-printed metal electrode. On the contrary, the sputtering-induced damage on poly-Si contacts is much more difficult to repair and requires a higher annealing temperature (>250 °C) in comparison to SHJ solar cells to reduce the deposition-induced damage [6]. This, in turn, impedes charge carrier transport across the poly-Si/TCO interface possibly due to the formation of a SiO_x interfacial layer [7–9]. Additionally, ultra-thin poly-Si layers (<20 nm) suffer from more severe sputtering-induced damage, since they cannot properly shield the c-Si/SiO_x interface from UV radiation and/or particle bombardment [10]. Consequently, minimizing the poly-Si thickness to further improve the photogenerated current of the cell is compromised by the aggravating sputtering-induced surface passivation loss of the contact.

On the other hand, pulsed laser deposition (PLD) has demonstrated its “soft” deposition properties on sensitive layers in organic [11, 12], perovskite [13], and most recently on SHJ solar cells [14]. PLD is based on the ablation of a solid target by a focused UV laser beam with nanosecond pulses, resulting in the removal of material from that target. This leads to the formation of a plasma plume that expands perpendicularly to the substrate which results in film growth. PLD has several unique characteristics that have shown to be beneficial to control the growth of complex oxide thin-films. For example, PLD allows for a vast range of tunability in processing parameters, since the laser source is physically decoupled from the processing chamber. Even though the physical aspects of PLD are relatively simple, the deposition process is intriguingly complex; the different regions in the allowed process parameter window are often interrelated and overlap. Additionally,

a large number of variable parameters exist and have direct influences on the layer properties.

In this work, we explore the influence of various PLD process parameters on the optical and electrical properties of ITO and the impact of sputtering and PLD-induced damage of the surface passivation quality of ultra-thin poly-Si contacts. Additionally, the effect of a post-annealing treatment on the contact resistivity of our poly-Si contacts is investigated.

6.2. EXPERIMENTAL DETAILS

6.2.1. SPUTTERING AND PLD OF ITO DEPOSITION

For comparison, a sputtered ITO film was deposited, as reference, with an inline sputtering DC magnetron tool. An ITO target containing 90 wt % of In_2O_3 and 10 wt % of SnO_2 was used while the deposition was performed at room temperature with an O_2 flow of about 2.6 sccm and a processing pressure of 0.01 mbar.

The PLD system, developed by Solmates BV, consists of a KrF excimer laser which creates ultra-short laser pulses at a wavelength of 248 nm which is directed towards the ITO target (90/10 wt% In_2O_3/SnO_2). The repetition rate and the fluence of the laser represent the frequency of the pulsed and energy density of the laser per pulse, respectively. Additionally, the laser properties, chamber pressure, O_2 to Ar ($Ar/(Ar+O_2)$) partial pressure, and substrate temperature are varied, as shown in Table 6.1. Note that all ITO films were deposited with the same deposition time. The samples were also subjected to a post-deposition annealing treatment in air at temperatures ranging from 190 to 350 °C.

6.2.2. ITO MATERIAL CHARACTERIZATION

Figure 6.1(a) shows the measurement schematic used to measure reflection and transmission of ITO films using a Lambda 950 spectrophotometer. The carrier concentration (N_e) and mobility (μ_e) of the ITO films were determined by using Hall effect measurements on samples with a in the van der Pauw contact configuration. To perform such measurements, the ITO layer was deposited on a thick SiO_2 (~450 nm) film which was thermally grown on a polished crystalline silicon (c-Si) substrate. A spectroscopic ellipsometry measurement (SE) system (J.A. Woollam Co., Inc.) was utilized to determine the thickness (d), and the refractive index and absorption coefficient (n & k) of the films. Note that the backside of the Si substrate was intentionally left unpolished to minimize the contribution of back side reflection during the SE measurement. Tauc-Lorentz and Drude oscillators were combined to model the optical parameters of our ITO films in both the ultra-violet and visible, and near infra-red parts of the spectrum, respectively. The sheet resistance (R_{sheet}) was measured using the four-point probe technique, from which the layer resistivity (ρ) was determined according to $R_{sheet} = \rho/d$.

Table 6.1.: PLD ITO films parameters variations

PLD parameter	Values
$O_2/(Ar+O_2)$ ratio [-]	0.2 - 1
Repetition rate [Hz]	10 - 100
Laser fluency [J/cm^2]	0.93 - 1.55
Chamber pressure [mbar]	0.02 - 0.2
Substrate temperature [°C]	25 - 400

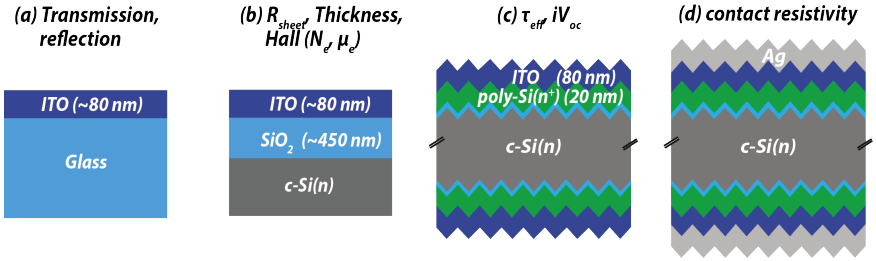

Figure 6.1.: Schematic overview of test measurement structures.

6

6.2.3. PROCESSING AND CHARACTERIZATION OF THE PASSIVATING CONTACTS

The impact of PLD ITO film deposition was investigated on a 20 nm thick poly-Si(n+) contact. Figure 6.1(c and d) shows the symmetric surface passivation and contact resistance test structures, as well as the solar cell schematic, respectively. M2-sized Czochralski (Cz) n-type wafers, with a base resistivity of ~ 3 Ω.cm and a thickness of a 180 μm, were textured using a KOH solution and rounded with a wet-chemical post treatment. As cleaning steps, the samples received a subsequential pre-treatment comprising of RCA 1 and 2, and nitric acid oxidation of silicon (NAOS) solutions. Subsequently, the wafers were dipped in a 1% diluted HF bath prior to the formation of an ultra-thin oxide in an oxidation tube using a mixture of O_2 and N_2 at 610 °C. Then, the ultra-thin n-type hydrogenated amorphous silicon (a-Si:H(n+)) layers with thickness of a 10 or 20 nm were deposited by plasma-enhanced chemical vapor deposition (PECVD). To form the poly-Si(n+) film, the crystallization was subsequently done at 900 °C. The hydrogenation scheme of the poly-Si(n+) contact was performed by the deposition of a sacrificial spatial atomic layer deposited (sALD) AlO_x film. The samples were annealed at 600 °C in an N_2 environment to allow for hydrogen diffusion to the Si interface. Finally, the AlO_x films were etched in a 1% diluted HF bath. For contact resistance measurements (as shown in Figure 6.1(d)), approximately 300 nm thick Ag films were sputtered on both sides.

The surface passivation quality of the cell precursors were measured by using a Sinton WCT-120 tool in the transient mode. Note that 5 measurements were taken per sample of which the average minority carrier lifetime value is reported here. An optical constant of 0.7 was used for the samples without ITO, while an optical

constant of 1.05 was used for the samples with ITO to account for the anti-reflective properties of the ITO. Contact resistivity of the overall c-Si/SiO_x/poly-Si(n+)/ITO/Ag stack was measured by vertical dark IV-measurement across the sample using the formula $R_{Total} = R_{base} + 2 \times R_{contact}$. $R_{contact}$ represents the overall contact resistance between the Si base material and the Ag contact. $R_{contact}$ represents the overall contact resistance between the Si base material and the Ag contact.

6.3. RESULTS

6.3.1. SPUTTERING AND PLD-INDUCED DAMAGE OF ITO DEPOSITION ON ULTRA-THIN POLY-SI CONTACTS

In order to compare the deposition-induced damage caused by sputtering and PLD, the effective lifetime (τ_{eff}) at an injection density of 10^{15} cm^{-3} was measured on samples with 10 and 20 nm thick poly-Si(n+) contacts. Sputtered and PLD ITO samples were fabricated at room temperature (RT) and at a similar operating pressure of 0.01 mbar. In addition, post-annealing treatments were performed in air at 190 °C and subsequently at 350 °C after ITO deposition. Figure 6.2 shows a comparison in τ_{eff} between sputtered and PLD ITO layers deposited on 10 and 20 nm thick poly-Si(n+) contacts and at different processing stages.

The initial τ_{eff} of the sample with 10 nm thick poly-Si contact (after hydrogenation) is lower than the corresponding one with the 20 nm contact and is caused by an unoptimized doping concentration and crystallization step of the poly-Si(n+) layer (this effect can be seen in Figure C1 of the appendices section), thereby resulting in a non-ideal diffusion of dopant into the c-Si substrate. Consequently, the initial τ_{eff} of the sample with the thinner layer is lower than the one with 20 nm poly-Si(n+)

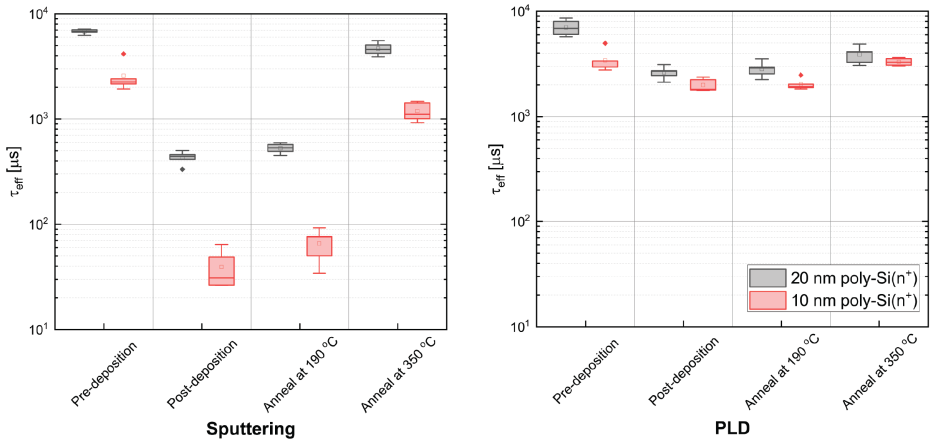

Figure 6.2.: Change in τ_{eff} for 10 and 20 nm poly-Si contacts before and after ITO deposition by (left) sputtering and (right) PLD, and post-annealing treatment at 190 and 350 °C. The PLD ITO layer was deposited at RT with an O_2 pressure of 0.012 mbar, a laser repetition rate of 50 Hz and a fluence of 1.55 J/cm^2.

mainly because of a lack in induced band bending (less so-called field effect passivation). After ITO deposition by sputtering, the surface passivation quality of the sample with the 20 nm thick contact drastically decreases. Further aggravated damage is observed for the sample with the thinner layer as a drop in τ_{eff} to about 30 µs is detected. A post-deposition annealing treatment at 190 °C only slightly improves the τ_{eff} for both samples with the 10 and 20 nm poly-Si thicknesses. Nevertheless, after a subsequent annealing treatment at 350 °C, τ_{eff} of the 10 and 20 nm poly-Si contact samples considerably improves, and this trend was also observed by Tutsch et al.[7]. While a certain level of PLD-induced damage is observed on the poly-Si contact, the decrease in τ_{eff} is significantly reduced in comparison to sputtering as τ_{eff} above 2 ms is achieved for both poly-Si thicknesses. Additionally, the damage caused by PLD is not dependent on the thickness of the poly-Si contact, as a comparable level of surface passivation is achieved directly after deposition. Likewise, an annealing treatment at 190 °C results in minimal surface passivation change while a slight lifetime improvement is perceived at 350 °C thereby resulting in an average τ_{eff} of 4.6 and 3.9 ms for the sputtered and PLD ITO poly-Si contact samples, respectively. Note that full recovery of τ_{eff} is not observed for samples with both poly-Si thicknesses and for both deposition technologies. The following part will explore the influence of laser parameters, substrate temperature (Tsub), and processing pressure on the deposition-induced damage corresponding to the PLD technique.

INFLUENCE OF LASER FLUENCE AND REPETITION RATE

Laser settings can have a considerable influence on the plasma parameters and on the material properties of the layers deposited [15, 16]. The KrF excimer laser creates ultra-short pulses in the order of ns duration where the frequency of these pulses, i.e. repetition rate, can influence the plasma interaction with the gas present in the chamber and subsequently the growth mechanism. Conversely, the laser fluence of the pulses dictates the ablation properties of the target material. For instance, low and high laser fluences can result in an evaporation-like deposition and sputtering-like ablation, respectively [15].

Here, the repetition rate and laser fluence for depositing ITO were varied from 20 to 50 Hz and 0.93 to 1.55 J/cm^2, respectively, as shown in Figure 6.3. The variation in laser fluence and repetition rate shows no significant impact on the PLD-induced damage, as for all process parameters applied τ_{eff} drops from about 5-6 ms to 2 ms after deposition. This indicates that the laser process parameters do not play an important role in minimizing the damage in the range of laser settings investigated here. A sufficient thermal budget at 350 °C is required to partially recover the PLD-induced damage.

EFFECT OF DEPOSITION TEMPERATURE

Next, we investigate the effect of deposition temperature (T_{dep}) on the change in surface passivation quality of our 20 nm poly-Si(n+) contacts, as shown in Figure 6.4. T_{dep} is varied between 20 and 400 °C while $P_{chamber}$ and the $O_2/(O_2+Ar)$ flow ratio are maintained at 0.02 mbar and 0.2, respectively. The change in surface

passivation after subsequent ITO deposition and annealing at 190 and 350 °C shows similar trends as previously observed for T_{dep} between 20 to 200 °C. However, at T_{dep}=400 °C the surface passivation quality after ITO deposition is further reduced and no recovery is observed after subsequent anneals. This could be due to the effusion of hydrogen which occurs during the deposition at higher temperature and at low pressure and thereby already leaving dangling bonds at the Si interface.

EFFECT OF CHAMBER PRESSURE

Lastly, the effect of the chamber pressure ($P_{chamber}$) on the induced deposition damage is investigated. Figure 6.5 shows the change in surface passivation quality with respect to the varying $P_{chamber}$ from 0.02 mbar to 0.2 mbar. Note that the initial surface passivation of the 20 nm poly-Si contact samples for the different process chamber pressures are slightly different. After ITO deposition at a $P_{chamber}$ = 0.1 mbar, a similar relative drop in τ_{eff} is observed to poly-Si contacts with ITO deposited at 0.02 mbar. However, a notable increase in τ_{eff} is observed after annealing at 190 °C and it slightly increases after a subsequent annealing treatment at 350 °C. At $P_{chamber}$ = 0.2 mbar, the drop in τ_{eff} is less and no change in τ_{eff} is perceived after annealing, not even for the samples annealed at 350 °C. This is indicative that the PLD-induced damage is less for ITO layers deposited at higher

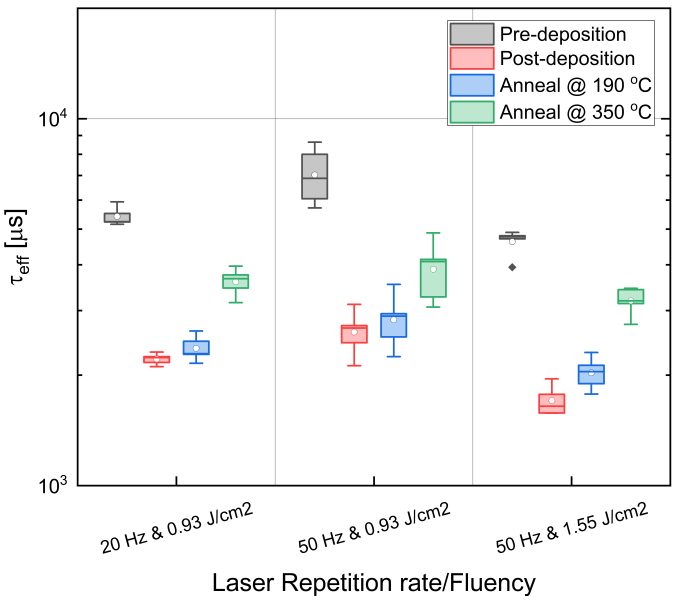

Figure 6.3.: Influence of laser repetition rate and fluence on the τ_{eff} of 20 nm poly-Si contacts. ITO films are deposited at RT, with $P_{chamber}$ = 0.02 mbar, and O_2 to Ar ratio = 0.2.

pressure and corresponding to the level that is observed after recovery anneals.

6.3.2. CONTACT RESISTIVITY

In this section, the influence of PLD parameters on the contact resistivity of overall poly-Si contacts are investigated. Figure 6 shows the overall contact resistivity of c-Si/poly-Si(n+)/ITO/Ag structures, meaning the overall $R_{contact}$ from base to metal, with a reference sputtered and PLD ITO films deposited at varying T_{dep} (20, 200 °C) and $P_{chamber}$ (0.012 - 0.1 mbar) conditions. These contacts were subsequently annealed at temperatures between 190 to 350 °C in air. Note that the PLD ITO film was deposited at 0.1 mbar and 200 °C, since higher deposition pressure and lower deposition temperature resulted in poor layer conductivity. Additionally, an oxygen pressure of 0.012 mbar (no Ar gas) was selected to deposit ITO, because optimal opto-electrical properties were obtained (as observed in Figure 6.7) at this pressure while no difference in surface passivation was observed with ITO deposited at 0.02 mbar.

The main contribution to the contact resistivity in this structure can be attributed to the poly-Si/ITO interface, since our poly-Si contact shows low contact resistance below 20 mΩcm^2. In order to minimize the impact of series resistance on fill factor

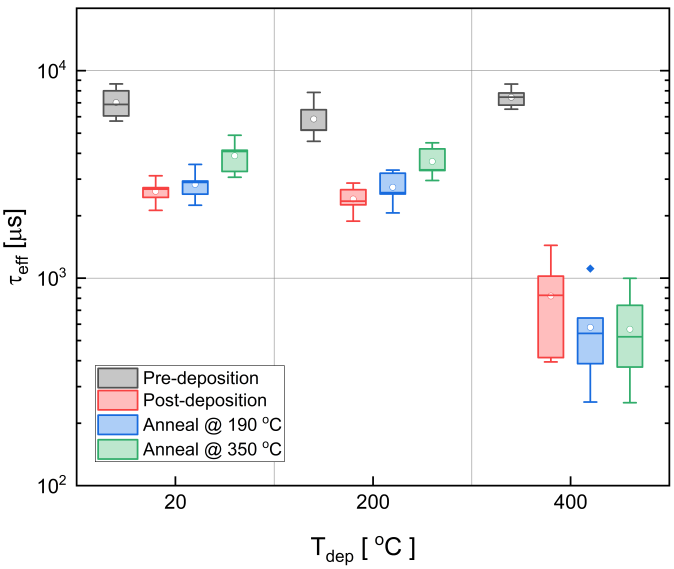

Figure 6.4.: Effect of T_{dep} (20 – 400 °C) on the surface passivation of 20 nm poly-Si contacts. ITO films are deposited at a $P_{chamber}$ = 0.02 mbar, O_2 to O_2+Ar ratio = 0.2, repetition rate = 50 Hz, and laser fluence = 0.93 J/cm^2.

losses, contact resistivity below 100 mΩcm^2 should be achieved [17]. As-deposited poly-Si contacts with PLD ITO layers show contact resistivities below 100 mΩcm^2. In comparison, poly-Si contact with sputtered ITO show a contact resistivity of about 300 mΩcm^2. The higher contact resistivity of our reference sputtered ITO structure could be due to the lower carrier concentration of the sputtered ITO which impedes the transport of majority carriers (reduction in barrier width) [9]. Significant increase in contact resistivity is observed for our sputtering reference for annealing temperature above 250 °C. Similar behavior is observed for a poly-Si contact with a PLD ITO layer deposited at 0.1 mbar where a steep increase in contact resistivity is noticed at annealing temperature of 350 °C. On the other hand, contacts with PLD ITO layers deposited at low pressures are thermally more stable even after a subsequential anneal at 350 °C.

6.3.3. OPTO-ELECTRICAL PROPERTIES OF PLD ITO LAYERS

The effect of PLD parameters on the ITO opto-electrical properties are discussed in this section. 80 nm thick ITO films were deposited at RT with varying partial oxygen pressure between 0.004 to 0.014 mbar. The laser fluence and repetition rate are kept at 0.93 J/cm^2 and 50 Hz, respectively. Figure 6.7 shows the ρ, R_{sheet}, and

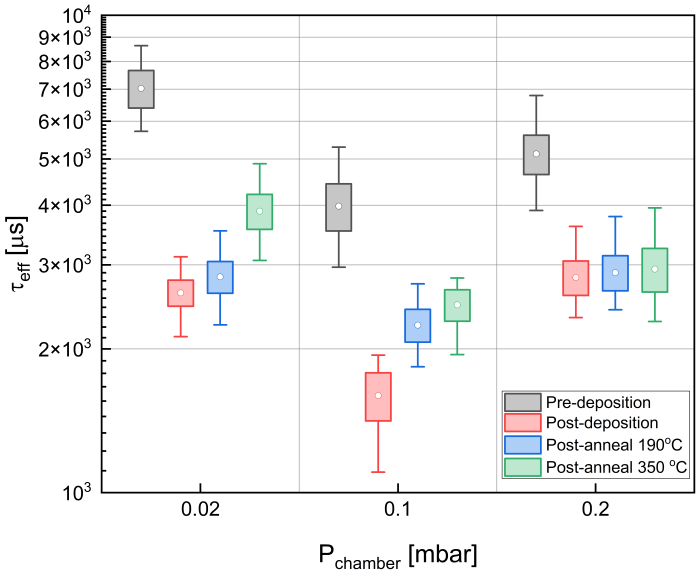

Figure 6.5.: Effect of $P_{chamber}$ (0.02 – 0.2 mbar) on the surface passivation of 20 nm poly-Si contacts. ITO films are deposited at RT with O_2/O_2+Ar ratio = 0.2, repetition rate = 50 Hz, and laser fluence = 0.93 J/cm^2.

the absorption (dependent on the wavelength) of the deposited ITO layers. The sputtering reference results in a ρ of 0.75 mΩcm. For PLD ITO films, a minimum

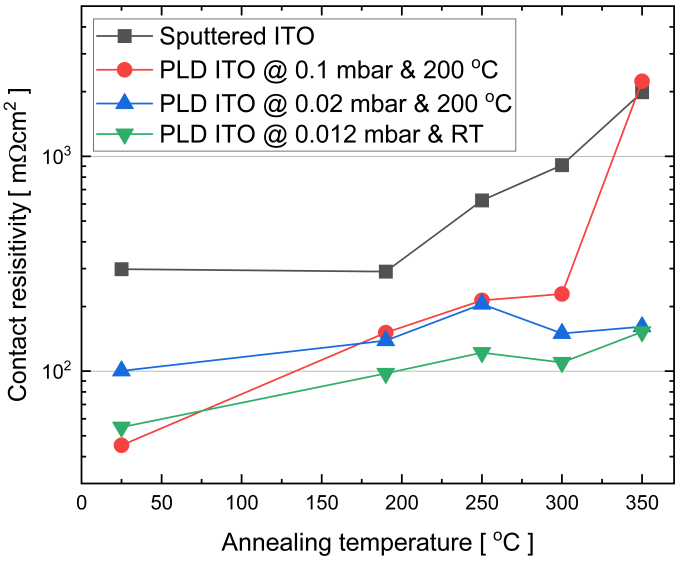

Figure 6.6.: Overall contact resistivity of 20 nm thick poly-Si contacts with sputtered and PLD ITO layers cumulatively annealed from 190 to 350 °C for 5 min at each annealing temperature. PLD ITO deposited at 0.1 mbar has an O_2/Ar+O_2 ratio of 0.1, laser repetition rate of 50 Hz and laser fluence of 1.55 J/cm^2.

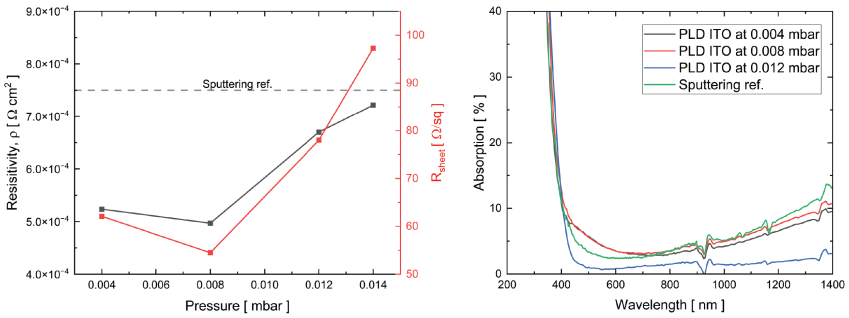

Figure 6.7.: Resistivity and R_{sheet} at varying oxygen pressure (0.004 – 0.014 mbar) (left) and absorption spectrum (right) of PLD ITO films. Opto-electrical properties of sputtered ITO reference are also included.

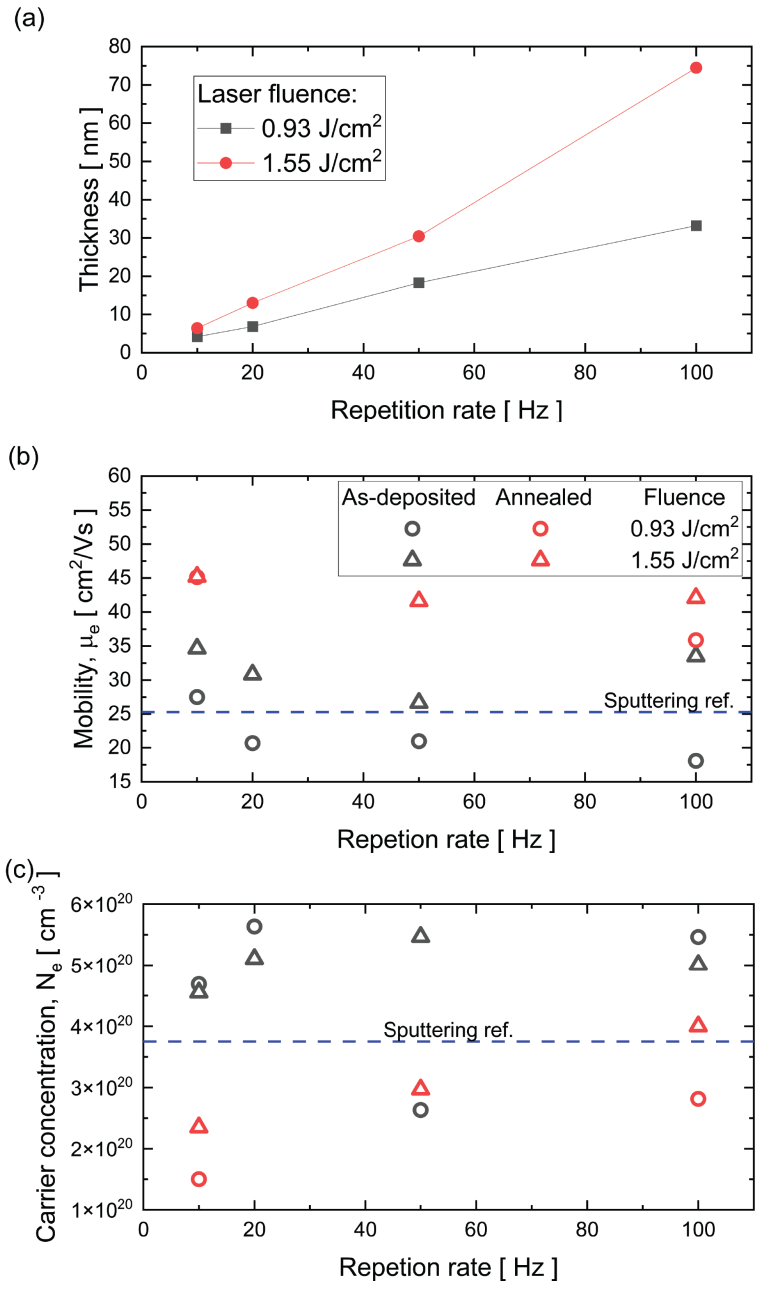

Figure 6.8.: Effect of PLD variations on the electrical properties. Electrical properties of sputtered ITO reference are also included.

resistivity of 0.49 mΩcm^2 is obtained at a chamber pressure of 0.008 mbar and increases at higher pressure. While a minimum resistivity can be obtained at an oxygen pressure of 0.008 mbar, the absorption of the ITO film in the visible and infra-red region is relatively high in comparison to the ITO layer deposited at 0.012 mbar. For a better trade-off between resistivity and absorption, the ITO layer deposited at 0.012 mbar is selected for further development.

Figure 6.8(a) shows the ITO thickness dependence on the repetition rate for laser fluence of 0.93 and 1.55 J/cm^2. An increase in repetition rate and laser fluence results in a thicker layer because more material whill be ablated at higher laser fluence and at higher repetition rates. Figure 6.8(b) and (c) show the μ_e and N_e of the ITO layers with respect to repetition rate, respectively, for laser fluences of 0.93 and 1.55 J/cm^2. The ITO layers are also subjected to an annealing treatment in air at 190 °C for 30 min. Prior to the thermal treatment, for the as-deposited ITO layers, a higher laser fluence results in an increase in μ_e. The μ_e of ITO layers do not show a strong dependence on repetition rate. After annealing, the μ_e of all ITO layers show an increase. For higher repetition rate a slight decrease is observed for the lower fluence, while for the higher fluence no dependence on repetition rate is observed. The increase in μ_e is most likely caused by an increase in grain size in the polycrystalline ITO layers [18]. The μ_e of ITO layers deposited at a fluence of 1.55 J/cm^2 shows minimal dependence on the repetition rate. As-deposited ITO layers show a high N_e independent of the laser fluence. After annealing, the N_e of the ITO layers decreases considerably and depends on the repetition rate; for both laser fluences an increase in N_e is observed for higher with repetition rates.

6.4. DISCUSSION

Significant induced damage resulting from ITO deposition is evident on ultra-thin poly-Si contact structures. Various factors, including work function mismatch between the contact layers, high-energy species, and radiation emitted during deposition, can contribute to the reduction in surface passivation of these contacts. A work function mismatch between the poly-Si(n+) and the ITO layers leads to a reduction in field-effect passivation, particularly noticeable at low injection levels [19]. This phenomenon is particularly observed in a-Si:H(p+) contacts and can be attributed to their comparatively lower doping efficiency when compared to their n-type counterparts[9, 20]. However, it is unlikely that the work function mismatch between the poly-Si(n+) and the ITO layer significantly influences the surface passivation quality of our 20 nm poly-Si(n+) contact. This assertion is supported by the absence of substantial improvement in charge carrier lifetime after etching off the ITO layer (refer to Figure C2 in appendix C).

Conversely, it is difficult to completely disentangle the different effects caused by plasma radiation, electrons, x-rays (arising from ions or electrons), and high energy particles bombardments. Several reports specify that the main cause of the subsequent damage is related to high energetic species that bombard the poly-Si contact [7, 17, 21, 22]. This is because sputtering relies on the ejection of the bulk target material to the substrate by momentum transfer; high energetic ions formed

by the plasma (typically Ar ions) bombard the target which results in the ejection of the target material [23]. Consequently, several high energetic species are formed at the target surface (O- and In- from ITO target) and in the plasma, and are accelerated towards the substrate by a potential difference between the target and the substrate. These high energy ions and species often have sufficient kinetic energy to penetrate through several nanometers of Si thereby rupturing bonds present at and near the Si/SiO_x interface. For plasma radiation induced damage, Tutsch et al.[21] showed that almost no degradation of 10 nm poly-Si based contact stacks was observed for photon with energy below 4 eV. However, the higher energy photons (9 eV), originating from argon and oxygen plasmas could cause significant structural damage to poly-Si contacts. For instance, Profijt et al.[24] showed that high energy ultra-violet photons in vacuum can cause significant loss in surface passivation on Si substrate with deposited Al_2O_3 films. While the thickness of the poly-Si(n+) plays an important role in shielding the damage caused by the ion bombardment, significant interface defects are still created at the Si/SiO_x interface for a 20 nm thick poly-Si layer. Several strategies exist to mitigate the damage caused by sputtering, such as increasing the deposition pressure and lowering the deposition power [25]. However, these processing conditions can result in ignition issues while high pressure can be problematic for obtaining a high quality layer[26].

On the contrary, the induced damage caused by the PLD technique is considerably reduced in comparison to our sputtering reference. This can be ascribed to the physical differences in deposition techniques; for PLD ablation of the target material is prompted by laser light absorption while sputtering relies on Ar ion bombardment. In PLD, a plasma plume is formed during the ablation process and is allowed to expand in the background gas due to the high-pressure gradients in the initial part of the plume [27–29]. The plume is allowed to slow down in the background gas and the atoms eventually diffuse out of the plume and migrate to the substrate [30]. For ultra-thin poly-Si(n+) based contacts the “softer” deposition properties of PLD result in superior surface passivation properties after ITO deposition. Furthermore, this behavior is also apparent on 10 nm poly-Si contacts which shows a minor degradation in surface passivation quality, unlike sputtering-induced damage. Nevertheless, the deposition of ITO on poly-Si(n+) layers by PLD still results in a certain level of damage. This induced damage is not related to the fluence (ranging between 0.93 -1.55 J/cm^2) and the repetition rate of the laser. A high chamber pressure is beneficial to mitigate the damage due to the thermalization of harmful species and hence resulting in a softer deposition on the poly-Si contact. Similar effects were observed on a buffer-free semi-transparent perovskite solar cell where an increase in pressure resulted in a damage-free deposition [13]. While PLD-induced damage caused by the plasma formation is present, the plasma formed by PLD is very complex and requires further investigations to determine the root cause of the PLD-induced damage. Possible causes, such as high energy photons, soft x-rays — arising from ion or electron bombardment — should not be excluded[31].

Although the root causes of the induced-deposition damage are not completely clarified, the surface passivation of the poly-Si contact can be almost completely repaired by a post-deposition annealing treatment at 350 °C. The change in surface

passivation quality after anneal is mainly attributed to a modification of the chemical passivation quality since a change in carrier population in the contact is unlikely due to the relatively low thermal budget; a thermal budget of 700-1050 °C is typically required to cause a change in poly-Si crystallization and dopant activation and diffusion. The surface passivation recovery of poly-Si based contacts is often reported after a post-deposition thermal annealing treatment at temperatures around 350 °C which also corresponds to our findings. This temperature requirement matches with the activation energy required for effective hydrogenation of poly-Si contacts. For instance, hydrogen plasma exposure or hydrogen-rich capping layers often require processing temperature higher than 300 °C to allow for effective diffusion of hydrogen to the SiO_x interface[32].34 It is highly plausible that the H atoms, in the vicinity of the SiO_x/c-Si interface, are allowed to diffuse again to the interface upon post-deposition annealing and thereby passivate the Si dangling bonds present at the surface, thus improving the chemical passivation quality.

The overall contact resistivity of the poly-Si based contact with sputtered ITO layer shows a significant increase at annealing temperatures higher than 250 °C. Various works[9, 19, 21] show similar trends and this is commonly linked to the formation of a parasitic SiO_x interlayer at the poly-Si/ITO interface[33]. This interlayer is allowed to grow rapidly under increasing thermal budget which, in turn, results in an inefficient tunneling transport of majority carriers to the ITO layer. Although annealing at 350 °C is required to recover the sputtering-induced damage of our poly-Si contact, the high contact resistivity results in an inefficient transport of majority carriers. Contacts with PLD ITO deposited at 200 °C show good contact resistivity while a slight increase is observed with annealing temperature. However, the significant increase in contact resistivity for contacts with PLD ITO deposited at high pressure suggests that the high partial O_2 pressure deposition promotes the formation of a parasitic oxide at the ITO/poly-Si(n+) interface. Nevertheless, due to the thermalization of harmful species at high pressure, annealing at 190 °C is sufficient to repair the induced damage at chamber pressures higher than 0.1 mbar. PLD ITO deposited at room temperature and low pressure enables low contact resistivity and does not promote a significant increase in contact resistivity which possibly indicates the absence of a parasitic oxide. However, further and more detailed analysis on the presence and composition of oxide is required for better understanding.

The optoelectrical properties of the PLD deposited ITO layer shows strong dependence on the total oxygen pressure. On the other hand, an increase in ITO deposition rate is observed with increasing repetition rate and laser fluency without majorly affecting the layer mobility after a post-deposition annealing treatment at 190 °C. Specifically, a remarkable ITO layer mobility of 42.1 cm_2/Vs and carrier concentration of 4.0 x 1020 cm^{-3} were attained at repetition rate of 100 Hz and laser fluency of 1.43 J/cm^2. Note that these measurements were carried out on a flat Si substrate which might be slightly different a on textured poly-Si substrate, and that final layer optimization should still be performed on cell level.

Nonetheless, while PLD demonstrates significant advantages for solar cell applications, the constraint imposed by the confined laser spot size presents

a substantial impediment to its implementation in high-throughput solar cell processes. Resolving this limitation requires dedicated efforts aimed at expanding the scalability of PLD techniques to large area substrates. Despite this challenge, PLD has exhibited significant benefits on perovskite solar cells, as significant work has been done on all active layers of the solar cell[13, 34, 35]. This progress is particularly promising for the integration of perovskite solar cells into tandem structures. Such advancements can pave the way for the seamless integration of perovskite solar cells with silicon-based tandem solar cells, offering an attractive avenue for elevating the efficiency and overall performance of the next generation of solar cell technologies.

6.5. CONCLUSIONS

Reducing the thickness of the poly-Si layer is essential to mitigate the parasitic absorption losses caused by the contact. However, this, in case ITO is applied by sputtering, aggravates the sputtering-induced damage on poly-Si layers thinner than 20 nm. Although a post-deposition annealing treatment can be performed to partially recover the damage, the contact resistivity drastically increases. Alternatively, TCO deposition by PLD has shown to be beneficial in minimizing the damage at the Si/SiO_x interface while maintaining low contact resistivity even after post-deposition annealing at 350 °C. Furthermore, the damage originating from PLD is not thickness dependent which allows for the development of thinner poly-Si contacts.

REFERENCES

[1] M. T. S. K. Ah Sen, A. Mewe, J. Melskens, J. Bolding, M. van de Poll, and A. Weeber. “Soft deposition of TCOs by pulsed laser for high-quality ultra-thin poly-Si passivating contacts”. In: *Journal of Applied Physics* 134.15 (2023).

[2] V. Shaw. *Chinese PV Industry Brief: JinkoSolar achieves 26.4% efficiency for n-type TOPCon solar cell*. 2022. URL: https://www.pv-magazine.com/2022/12/09/chinese-pv-industry-brief-jinkosolar-achieves-26-1-efficiency-for-n-type-topcon-solar-cell/ (visited on 12/23/2022).

[3] C. N. Kruse, S. Schäfer, F. Haase, V. Mertens, H. Schulte-Huxel, B. Lim, B. Min, T. Dullweber, R. Peibst, and R. Brendel. “Simulation-based roadmap for the integration of poly-silicon on oxide contacts into screen-printed crystalline silicon solar cells”. In: *Scientific reports* 11.1 (2021), p. 996.

[4] R. Street, D. Biegelsen, and J. Stuke. “Defects in bombarded amorphous silicon”. In: *Philosophical Magazine B* 40.6 (1979), pp. 451–464.

[5] B. Demaurex, S. De Wolf, A. Descoeudres, Z. Charles Holman, and C. Ballif. “Damage at hydrogenated amorphous/crystalline silicon interfaces by indium tin oxide overlayer sputtering”. In: *Applied Physics Letters* 101.17 (2012), p. 171604.

[6] T. F. Wietler, B. Min, S. Reiter, Y. Larionova, R. Reineke-Koch, F. Heinemeyer, R. Brendel, A. Feldhoff, J. Krügener, D. Tetzlaff, *et al.* “High temperature annealing of ZnO: Al on passivating POLO junctions: Impact on transparency, conductivity, junction passivation, and interface stability”. In: *IEEE Journal of Photovoltaics* 9.1 (2018), pp. 89–96.

[7] L. Tutsch, F. Feldmann, M. Bivour, W. Wolke, M. Hermle, and J. Rentsch. “Integrating transparent conductive oxides to improve the infrared response of silicon solar cells with passivating rear contacts”. In: *AIP Conference Proceedings*. Vol. 1999. 1. AIP Publishing LLC. 2018, p. 040023.

[8] M. Wimmer, M. Bär, D. Gerlach, R. Wilks, S. Scherf, C. Lupulescu, F. Ruske, R. Félix, J. Hüpkes, G. Gavrila, *et al.* “Hard x-ray photoelectron spectroscopy study of the buried Si/ZnO thin-film solar cell interface: Direct evidence for the formation of Si–O at the expense of Zn-O bonds”. In: *Applied physics letters* 99.15 (2011), p. 152104.

[9] C. Messmer, M. Bivour, C. Luderer, L. Tutsch, J. Schön, and M. Hermle. “Influence of interfacial oxides at TCO/doped Si thin film contacts on the charge carrier transport of passivating contacts”. In: *IEEE Journal of Photovoltaics* 10.2 (2019), pp. 343–350.

[10] L. Tutsch, F. Feldmann, B. Macco, M. Bivour, E. Kessels, and M. Hermle. “Improved passivation of n-type poly-Si based passivating contacts by the application of hydrogen-rich transparent conductive oxides”. In: *IEEE Journal of Photovoltaics* 10.4 (2020), pp. 986–991.

[11] J. M. Dekkers and J. A. Janssens. *Method for depositing a target material onto a organic electrically functional material*. US Patent 10,128,467. Nov. 2018.

[12] S. Schubert, F. Schmidt, H. von Wenckstern, M. Grundmann, K. Leo, and L. Müller-Meskamp. “Eclipse Pulsed Laser Deposition for Damage-Free Preparation of Transparent ZnO Electrodes on Top of Organic Solar Cells”. In: *Advanced Functional Materials* 25.27 (2015), pp. 4321–4327.

[13] Y. Smirnov, L. Schmengler, R. Kuik, P.-A. Repecaud, M. Najafi, D. Zhang, M. Theelen, E. Aydin, S. Veenstra, S. De Wolf, *et al.* “Scalable pulsed laser deposition of transparent rear electrode for perovskite solar cells”. In: *Advanced Materials Technologies* 6.2 (2021), p. 2000856.

[14] Y. Smirnov, P.-A. Repecaud, L. Tutsch, I. Florea, K. P. Zanoni, A. Paliwal, H. J. Bolink, P. R. i Cabarrocas, M. Bivour, and M. Morales-Masis. “Wafer-scale pulsed laser deposition of ITO for solar cells: Reduced damage vs. interfacial resistance”. In: *Materials Advances* 3.8 (2022), pp. 3469–3478.

[15] J. Schou. “Physical aspects of the pulsed laser deposition technique: The stoichiometric transfer of material from target to film”. In: *Applied Surface Science* 255.10 (2009), pp. 5191–5198.

[16] A. Ojeda-G-P, M. Döbeli, and T. Lippert. “Influence of plume properties on thin film composition in pulsed laser deposition”. In: *Advanced Materials Interfaces* 5.18 (2018), p. 1701062.

[17] J. Melskens, B. W. van de Loo, B. Macco, L. E. Black, S. Smit, and W. Kessels. “Passivating contacts for crystalline silicon solar cells: From concepts and materials to prospects”. In: *IEEE Journal of Photovoltaics* 8.2 (2018), pp. 373–388.

[18] B. Macco, H. C. Knoops, and W. M. Kessels. “Electron scattering and doping mechanisms in solid-phase-crystallized In2O3: H prepared by atomic layer deposition”. In: *ACS applied materials & interfaces* 7.30 (2015), pp. 16723–16729.

[19] R. Rößler, C. Leendertz, L. Korte, N. Mingirulli, and B. Rech. “Impact of the transparent conductive oxide work function on injection-dependent a-Si: H/c-Si band bending and solar cell parameters”. In: *Journal of Applied Physics* 113.14 (2013).

[20] W. Spear and P. Le Comber. “Substitutional doping of amorphous silicon”. In: *Solid state communications* 17.9 (1975), pp. 1193–1196.

[21] L. Tutsch, F. Feldmann, J. Polzin, C. Luderer, M. Bivour, A. Moldovan, J. Rentsch, and M. Hermle. “Implementing transparent conducting oxides by DC sputtering on ultrathin SiOx/poly-Si passivating contacts”. In: *Solar Energy Materials and Solar Cells* 200 (2019), p. 109960.

[22] Y. Larionova, H. Schulte-Huxel, B. Min, S. Schaefer, T. Kluge, H. Mehlich, R. Brendel, and R. Peibst. “Ultra-Thin Poly-Si Layers: Passivation Quality, Utilization of Charge Carriers Generated in the Poly-Si and Application on Screen-Printed Double-Side Contacted Polycrystalline Si on Oxide Cells”. In: *Solar RRL* 4.10 (2020), p. 2000177.

[23] E. Aydin, C. Altinkaya, Y. Smirnov, M. A. Yaqin, K. P. Zanoni, A. Paliwal, Y. Firdaus, T. G. Allen, T. D. Anthopoulos, H. J. Bolink, *et al.* “Sputtered transparent electrodes for optoelectronic devices: Induced damage and mitigation strategies”. In: *Matter* 4.11 (2021), pp. 3549–3584.

[24] H. Profijt, P. Kudlacek, M. Van de Sanden, and W. Kessels. “Ion and photon surface interaction during remote plasma ALD of metal oxides”. In: *Journal of The Electrochemical Society* 158.4 (2011), G88.

[25] M. Köhler, M. Pomaska, P. Procel, R. Santbergen, A. Zamchiy, B. Macco, A. Lambertz, W. Duan, P. Cao, B. Klingebiel, *et al.* “A silicon carbide-based highly transparent passivating contact for crystalline silicon solar cells approaching efficiencies of 24%”. In: *Nature Energy* 6.5 (2021), pp. 529–537.

[26] A. J. Bett, K. M. Winkler, M. Bivour, L. Cojocaru, Ö. Ş. Kabakli, P. S. Schulze, G. Siefer, L. Tutsch, M. Hermle, S. W. Glunz, *et al.* “Semi-transparent perovskite solar cells with ITO directly sputtered on Spiro-OMeTAD for tandem applications”. In: *ACS applied materials & interfaces* 11.49 (2019), pp. 45796–45804.

[27] Y. Pauleau. *Materials surface processing by directed energy techniques*. Elsevier, 2006.

[28] Y. B. Zel’Dovich and Y. P. Raizer. *Physics of shock waves and high-temperature hydrodynamic phenomena*. Courier Corporation, 2002.

[29] S. Anisimov, D. Bäuerle, and B. Luk’Yanchuk. “Gas dynamics and film profiles in pulsed-laser deposition of materials”. In: *Physical Review B* 48.16 (1993), p. 12076.

[30] S. Amoruso, R. Bruzzese, N. Spinelli, R. Velotta, M. Vitiello, and X. Wang. “Dynamics of laser-ablated MgB 2 plasma expanding in argon probed by optical emission spectroscopy”. In: *Physical Review B* 67.22 (2003), p. 224503.

[31] H.-U. Krebs, M. Weisheit, J. Faupel, E. Süske, T. Scharf, C. Fuhse, M. Störmer, K. Sturm, M. Seibt, H. Kijewski, *et al.* “Pulsed laser deposition (PLD)–a versatile thin film technique”. In: *Advances in solid state physics* (2003), pp. 505–518.

[32] B. Van De Loo, B. Macco, J. Melskens, W. Beyer, and W. Kessels. “Silicon surface passivation by transparent conductive zinc oxide”. In: *Journal of Applied Physics* 125.10 (2019), p. 105305.

[33] M. Hermle, F. Feldmann, M. Bivour, J. C. Goldschmidt, and S. W. Glunz. “Passivating contacts and tandem concepts: Approaches for the highest silicon-based solar cell efficiencies”. In: *Applied Physics Reviews* 7.2 (2020), p. 021305.

[34] T. Soto-Montero, S. Kralj, W. Soltanpoor, J. S. Solomon, J. S. Gómez, K. P. Zanoni, A. Paliwal, H. J. Bolink, C. Baeumer, A. P. Kentgens, *et al.* “Single-Source Vapor-Deposition of MA1–xFAxPbI3 Perovskite Absorbers for Solar Cells”. In: *Advanced Functional Materials* (2023), p. 2300588.

[35] Z. Qiu, H. Gong, G. Zheng, S. Yuan, H. Zhang, X. Zhu, H. Zhou, and B. Cao. “Enhanced physical properties of pulsed laser deposited NiO films via annealing and lithium doping for improving perovskite solar cell efficiency”. In: *Journal of Materials Chemistry C* 5.28 (2017), pp. 7084–7094.

7

PULSED LASER DEPOSITION OF MoO_X AND TiO_X SELECTIVE CONTACTS FOR C-SI SOLAR CELLS

In recent years, the promising potential of employing metal oxide contacts in c-Si and perovskite solar cells has become increasingly evident. This stems from their demonstrated attributes of remarkable optical properties, extensive work function ranges, and versatile deposition processes. Nevertheless, these contacts can often exhibit carrier-selectivity issues in c-Si solar cells due to a band gap misalignment of the metal oxide contact with respect to the Si absorber. Further efforts have been dedicated to improve the contact properties of these metal oxide materials. In this chapter, the passivating and carrier-selectivity MoO_x and TiO_x contacts deposited by pulsed laser deposition (PLD) are explored. PLD offers a wide range of tunability of material properties and is often suitable for complex oxide growth. This study shows an improvement in carrier selectivity of the MoO_x contact through an increase in deposition pressure. Nonetheless, despite these improvements, noticeable carrier selectivity losses persist, giving rise to an S-shaped current-voltage (IV) curve. On the other hand, PLD TiO_x contact shows excellent passivation on intrinsic hydrogenated amorphous Si (a-Si:H(i)) and SiO_y passivating interlayers. An excellent implied open circuit voltage (iV_{oc} of 700 mV) was obtained with the TiOx/SiO_y:H contact without a post-hydrogenation step. Finally, a full metal oxide solar cell, consisting of MoO_x and TiO_x contacts, have been fabricated yielding an impressive iV_{oc} of 742 mV.

7.1. INTRODUCTION

PASSIVATING and carrier-selective contacts for crystalline silicon (c-Si) solar cells have shown to enable high conversion efficiencies by reducing carriers recombination losses at the Si interfaces. Silicon heterojunction (SHJ) and doped poly-Si contact structures are prime examples of the passivating and carrier-selective contacts to achieve high efficiencies. Nevertheless, the quality of the doped-Si contacts is mainly limited by parasitic absorption, especially at the front side of the solar cells. Although this limitation can be avoided by placing both contacts at the rear side of the cell, in an interdigitated back contact (IBC) design, this structure also increases the level of manufacturing complexity. Other strategies, such as thinning the Si-based layers [1, 2], band gap widening by carbon or oxygen alloying [3–5], or use of nano-crystalline silicon [6, 7], have been explored to mitigate the short-circuit current density (J_{sc}) losses. In fact, these strategies are not only beneficial to improve J_{sc}; numerical device modelling suggests that further gain in J_{sc}, by band gap widening of contact layers, can be advantageous for improving the open circuit voltage (V_{oc}) and fill factor (FF) of solar cells [8].

Alloying of Si-based contact materials, however, have limited band gaps and work function (WF), and require meticulous optimization in order to prevent detrimental effects on the majority carrier transport through the contact. Alternative materials based on transition metal oxides offer wider WF ranges and superior optical properties. In addition, the processing of these materials often allow for simplistic, low-temperature deposition methods, and are well-aligned with perovskite cell processes which can potentially reduce the fabrication costs. Implementation of the metal oxide contacts in c-Si solar cells have shown to reach high conversion efficiencies in the past decade. In particular, MoO_x, as a hole contact, has been integrated in SHJ solar cells and has shown great promise by achieving efficiency of 23.83% [9]. Conversely, TiO_x has proven to be a suitable electron contact because of its good band alignments with c-Si thereby resulting in efficiency exceeding 22% on a full-area contact [10]. However, several factors have limited the step towards industrial implementation of these contacts. The prominent reasons can be attributed to the lack of chemical tuning of relevant elements [11], instability upon air and thermal exposures, and degradation upon interaction with adjacent layers.

To tackle these issues, metal oxides layers deposited by pulsed laser deposition (PLD) were explored. PLD offers several advantages since various parameters can be tuned to form complex material stoichiometry. This is because the ablation process is decoupled from the other process parameters allowing for a wide range of material tunability. In addition, PLD enables in-situ stack formation which can be useful to prevent degradation of sensitive material upon air exposure. Finally, PLD displays soft deposition properties which can mitigate the interaction to underlying sensitive layers or interfaces. In this chapter, the surface passivation and carrier-selectivity of MoO_x and TiO_x contacts are explored on c-Si solar cells.

7.2. EXPERIMENTAL DETAILS

180 µm thick pseudo squared textured M2 n-type <100> Cz wafers were pre-gettering with $POCl_3$ resulting a bulk resistivity of ~2.6 Ohm/sq. After gettering, the wafers were textured in alkaline and smoothed (batch smoothing), and subsequently received a pre-clean treatment consisting of RCA 1 and 2, and NAOS treatments. Wafers were dipped in a 1% diluted HF bath prior to cell processing.

80 nm MoO_x layers were initially deposited on FZ c-Si planar wafers to determine the optical properties of the layers, as shown by the schematic in Figure 7.1(a). Figure 7.1 (b, c) shows the schematic of half-fabricates and solar cells for MoO_x-based contacts, also denoted as "moly-poly" cells. Moly-poly solar cells consist of a 20 nm rear poly-Si(n+) contact and has been proven to be stable while providing with excellent surface passivation. Processing details of the poly-Si(n+) contact can be found in Chapter 2. The front side of the solar cells consist of a 10 nm thick a-Si:H(i) interlayer deposited by plasma enhanced chemical vapor deposition (PECVD). Subsequently, MoO_x was deposited at room temperature in a PLD chamber whereby the deposition parameters were varied. In-situ PLD ITO deposition was subsequently performed to prevent the exposure of MoO_x layer to air. Finally, moly-poly solar cells were metallized with a rear physical vapor deposition (PVD) Ag blanket and front screen-printed Ag grid, and anneal at 190 °C for 30 min.

The surface passivation properties of TiO_x contacts were assessed on symmetric samples consisting of either an a-Si:H(i) or a SiO_y:H interlayer, as shown in Figure 7.2(a). The latter was formed by etching off an ALD Al_2O_3 for 1 min at 60 °C in a 1% diluted TMAH solution (as presented in Chapter 5). PLD TiO_x films were deposited at room temperature with varying pressure and gas ratio. Finally, solar cells with rear TiO_x contact consists of a front a-Si:H(i/p+) contact (shown in Figure 7.2(b)) were manufactured. At the rear side, an Al blanket was deposited by electron beam (e-beam) deposition.

Optical properties of developed layers were obtained by spectroscopic ellipsometry measurement system (J.A. Woollam Co., Inc.). The model applied to determine the

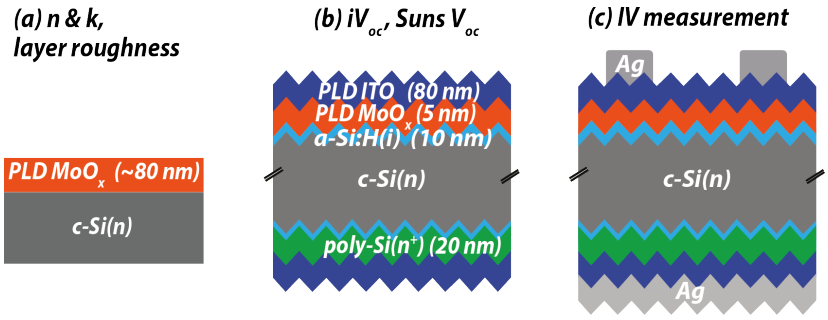

Figure 7.1.: Schematics consisting of (a) ~80 nm PLD MoO_x layer deposited on mechanically polished FZ c-Si, (b) moly-poly cell precursors with rear poly-Si(n+) contact capped with PLD ITO layers, (c) moly-poly cells with rear Ag blanket and front screen-printed Ag grid.

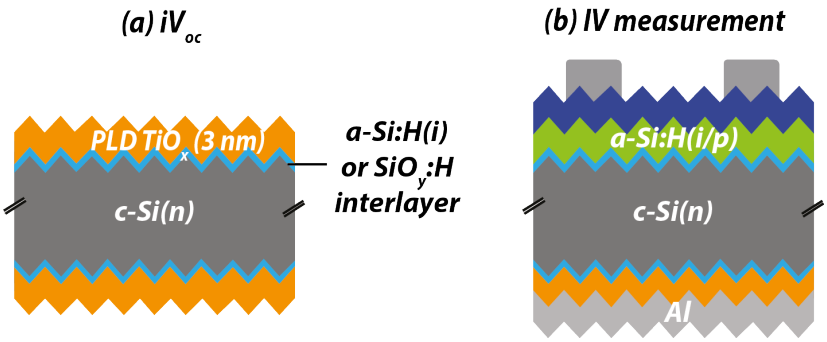

Figure 7.2.: Schematics of TiO_X contacts for (a) surface passivation and (b) *IV* test samples.

optical properties of the MoO_X layer consists of a combination of Tauc-Lorentz and Gaussian oscillators. The passivation properties of the MoO_X and TiO_X contacts were measured by using a Sinton WCT-120 tool with transient mode. $SunsV_{oc}$ by Sinton was utilized to measure the external V_{oc} of cell precursors. The *IV* measurements of the solar cells were performed in a Wacom AAA solar simulator, and were corrected for spectral mismatch.

7.3. RESULTS AND DISCUSSION

7.3.1. PLD MoO_X CONTACT

OPTICAL PROPERTIES OF MoO_X WITH VARYING O_2 PRESSURE

Firstly, the optical properties of PLD MoO_X, as measured by ellipsometry, were determined for varying O_2 total deposition pressure. Figures 7.3(a) and (b) show the refractive index (n) and layer roughness per nm of MoO_X deposited at O_2 total

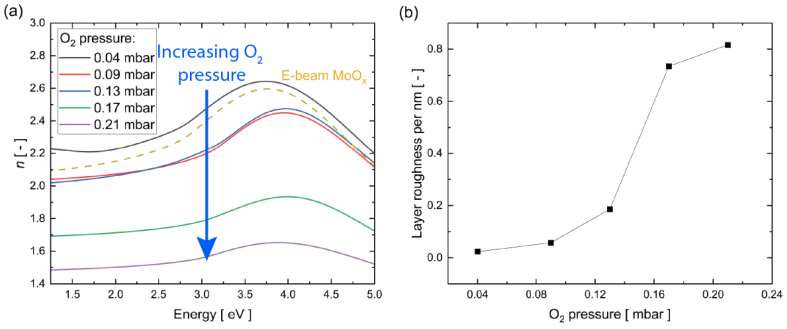

Figure 7.3.: Influence of varying O_2 pressure between 0.04 – 0.21 mbar (a) refractive index (n) and (b) layer roughness on PLD deposited MoO_X films, as determined by ellipsometry.

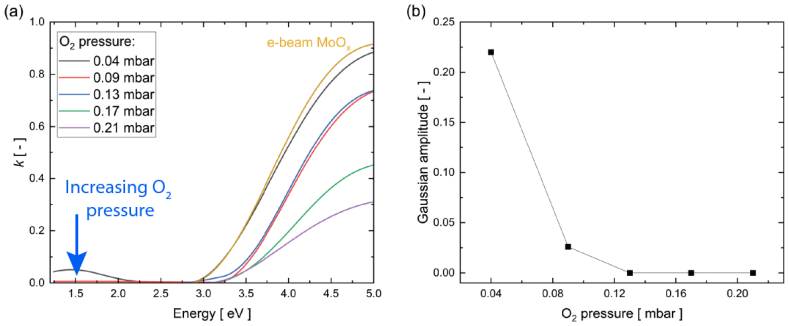

Figure 7.4.: Influence of varying O_2 pressure between 0.04 – 0.21 mbar (a) k and (b) Gaussian amplitude of PLD deposited MoO_x films, as determined by ellipsometry.

pressure between 0.04 to 0.21 mbar, respectively. The n of the MoO_x layers drops gradually as a function of the oxygen total pressure up to 0.13 mbar. For higher oxygen total pressures, the drop in n is suddenly much steeper. This abrupt change in n could explain the reason why PLD layers deposited at higher pressure become more porous, which correlates with the increase in layer roughness. The reference MoO_x film deposited by e-beam shows similar n values compared to PLD layers deposited between O_2 total pressure of 0.04 and 0.09 mbar. The disparities between these two layers can be attributed to differences in the deposition process. The e-beam MoO_x layer is deposited at a rate of 0.1 nm/s, whereas the PLD MoO_x was deposited at a rate of approximately 2 nm/s. Additionally, the deposition pressure varies, with the e-beam MoO_x layer being deposited in high vacuum conditions.

Next, the absorption coefficients (k) of the MoO_x films are depicted in Figure 7.4(a). A sub-bandgap absorption curve is observed for MoO_x deposited at 0.04 mbar but disappears with an increase in O_2 deposition total pressure. Similar trend in optical transmission can be found in appendix D and is also observed by Scirè et al. [12]. This behaviour is often observed for sub-stoichiometry MoO_x films which display distinctive sub-band absorption peaks at ~1.4 eV, and is caused by the presence of Mo^{5+} and Mo^{4+} oxidation states [13, 14]. The presence of these oxidation states implies that the MoO_x WF is too low and could affect for hole carrier selectivity of the MoO_x contact [15]. Figure 7.4(b) shows the amplitude values for the sub-band gap absorption curve (defined by a gaussian oscillator in ellipsometry) for varying O_2 pressure. An increase in O_2 deposition total pressure results in a decrease in amplitude which disappears at O_2 total pressure higher than 0.13 mbar. Note that the as-deposited e-beam MoO_x reference layer shows no sub-band gap absorption. When oxygen total pressure settings exceed 0.13 mbar, the surface of the layers becomes notably rough and tends to flake, which can pose potential safety hazards. The excess incorporation of oxygen in the MoO_x layer likely alters the layer structure resulting a sparse layer. For this reason, the test range for the layers in cells was set from 0.04 to 0.13 mbar, as shown below.

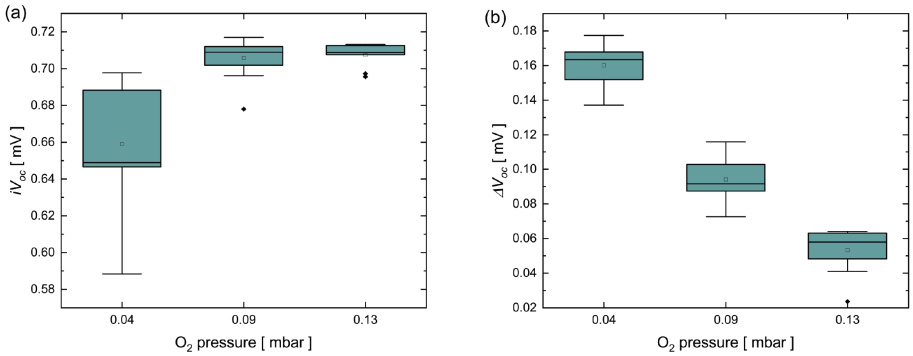

Figure 7.5.: Influence of varying O_2 total pressure between 0.04 – 0.13 mbar (a) iV_{oc} and (b) decreasing ΔV_{oc} with increasing O_2 pressure of cell precursors after PLD depositions. MoO_x layers were deposited at laser fluence and repetition rate of 1.43 J/cm^2 and 50 Hz, respectively.

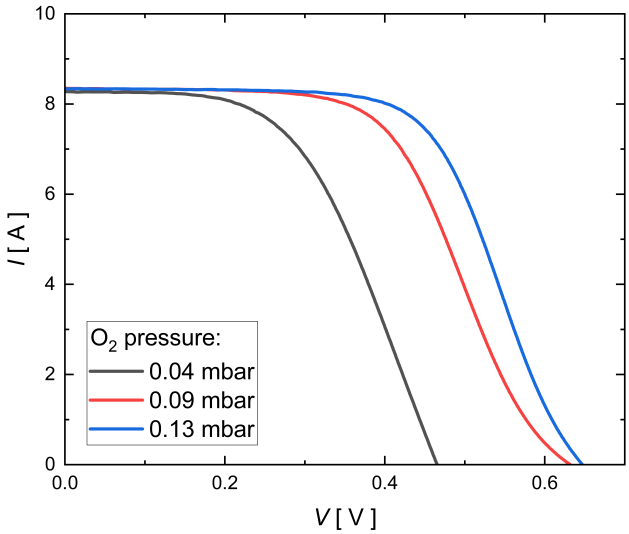

Figure 7.6.: IV curve of moly-poly solar cells with varying O_2 total pressure during MoO_x layer deposition.

SURFACE PASSIVATION AND CARRIER SELECTIVE PROPERTIES OF PLD MoO_X CONTACT

Moly-poly cell precursors with a rear poly-Si(n+) contact were manufactured by depositing PLD MoO_x and ITO layers on a front a-Si:H(i) interlayer, as shown with

the schematic in Figure 7.1(b). The deposited MoO_x layers were capped in-situ with a PLD ITO layer to prevent the degradation of MoO_x properties upon exposure to air. Subsequently, the surface passivation and carrier selectivity properties were analysed for as-deposited PLD MoO_x layers with varying O_2 total pressure between 0.04 and 0.13 mbar. Figure 5 (a) and (b) shows iV_{oc} and ΔV_{oc} (iV_{oc} - $sunsV_{oc}$) of the cell precursors after deposition, respectively. The iV_{oc} values of the precursor solar cells, after PLD depositions, show less degradation in terms of surface passivation with increasing O_2 total pressure; minimal damage is perceived at pressure > 0.09 mbar. Similar passivation behaviour can be observed in chapter 6 after ITO deposition on poly-Si(n+) contacts at similar deposition pressure. As a result, excellent iV_{oc} of about 710 mV is obtained for the moly-poly cell with MoO_x deposited at 0.13 mbar. Besides the surface passivation quality of the contacts, O_2 total pressure has a strong influence on the contact selectivity; a decrease in ΔV_{oc} is observed with increasing pressure. This correlates with the sub-bandgap absorption measured for PLD MoO_x layers with lower O_2 deposition total pressures. Note that iV_{oc} values after a curing anneal is not shown since the precursors were only annealed after metallization to mitigate the thermal degradation on the MoO_x contact.

After front and rear contacts metallization, the IV characteristics were measured for these solar cells, as shown in Figure 7.6. IV curves of the MoO_x contacts show S-shaped behaviours implying a lack of carrier selectivity of the MoO_x contacts. The carrier selectivity loss of the contacts also leads to a reduced FF and V_{oc} for solar cell with MoO_x layer deposited at 0.13 mbar. Although the carrier selectivity improves with increasing pressure, the selective properties of the contact at O_2 total pressure higher than 0.13 mbar shows no further improvement (not shown here). The high ΔV_{oc} caused by PLD MoO_x contact could be prompted by several transport issues, such as lack of upward band bending of the c-Si because of the insufficient WF and/or the formation a tunneling parasitic oxide at the MoO_x/a-Si:H(i) interface, under high O_2 deposition total pressure. It has been reported that high PLD O_2 deposition total pressure can result in the formation of a parasitic oxide on the a-Si:H surface which can be detrimental for effective transport at the MoO_x/a-Si:H(i) interface [16]. To reduce the formation of a parasitic oxide at the MoO_x/a-Si:H(i) interface, the effect of Ar to O_2 gas ratio has also been investigated. A decrease in O_2 partial pressure shows no improvement in carrier selectivity (refer to Figure D2 in Appendix D) which indicates that the parasitic oxide is not the main reason for the apparent hole-carrier selectivity loss of the MoO_x contact.

Conversely, it is highly probable that the observed selectivity loss originates from a too low WF of the deposited PLD MoO_x layers. In contrast, thermally evaporated MoO_x often exhibits sufficiently high WF characteristics. In such instances, MoO_x is typically deposited under vacuum conditions and at a low deposition rate (~0.1 nm/s). This differs significantly from the MoO_x layer deposited by PLD, where a higher deposition rate (~2.5 nm/s) is utilized, along with elevated oxygen deposition total pressure. To emulate the deposition conditions of the evaporated MoO_x contact, it is essential to reduce the deposition rate further by minimizing the laser fluency under vacuum conditions. A comprehensive layer analysis is also required to comprehend the multifaceted influences of these PLD parameters on

material properties, such as layer stoichiometry and WF. These factors are pivotal in determining the carrier selectivity properties of the contact.

7.3.2. PLD TiO_X CONTACT

In this section, the electron-selective and passivating contact properties of TiO_x layers deposited by PLD are explored. Ultra-thin SiO_x and a-Si:H(i) interlayers were chosen since they have shown to provide excellent surface passivation quality on TiO_x contacts, resulting in efficiencies of 22.1 and 20.7%, respectively [17, 18]. SiO_x:H interlayer, developed in chapter 5, is applied to probe the surface passivation properties with TiO_x contact.

SURFACE PASSIVATION WITH VARYING O_2 PRESSURE

The influence of the O_2 deposition total pressure of PLD TiO_x contact is initially explored on the surface passivation properties of the contact. Figure 7.9 shows the iV_{oc} of symmetric textured n-type Si wafers with TiO_x/SiO_y:H stacks for O_2

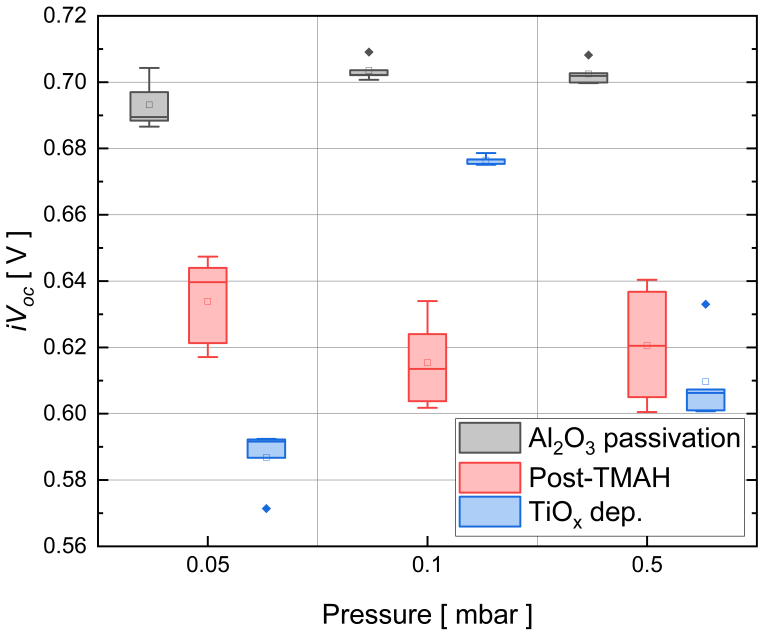

Figure 7.7.: Influence of O_2 total pressure on the iV_{oc} of TiO_x/SiO_y:H stack for pressure between 0.05 to 0.5 mbar. No Ar was added during these depositions. 3 nm thick TiO_x was deposited at laser fluence and repetition rate are set at 1.43 J/cm^2 and 20 Hz, respectively.

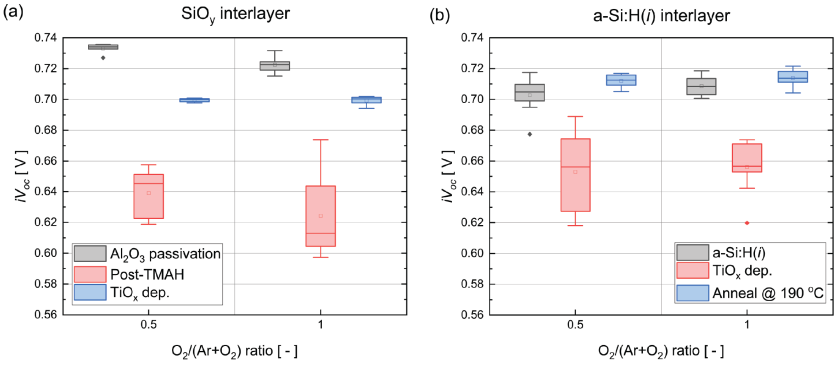

Figure 7.8.: Change in iV_{oc} for (a) TiO_x/SiO_y and (b) TiO_x/a-Si:H(i) stacks, after TiO_x and annealing at 190 °C. 3nm thick TiO_x deposited at RT and at 0.1 mbar, with laser fluence and repetition rate of 1.43 J/cm^2 and 20 Hz, respectively.

deposition pressure varied between 0.05 to 0.5 mbar. Good passivation is initially provided by Al_2O_3 layers. After Al_2O_3 etching, the iV_{oc} decreases partly because of the absence of the field-effect surface passivation provided by the Al_2O_3 layer. After subsequent TiO_x deposition, the iV_{oc} further decreases at low O_2 total pressure (0.05 mbar) which can be assigned to the deposition damage which is prominent at low deposition pressure. Conversely, the iV_{oc} of the stack improves after TiO_x deposition at 0.1 mbar which is owed to the mitigation of deposition damage and the possible presence of field-effect passivation provided by the TiO_x layer. Further increase in total pressure (0.5 mbar) does not result in a major change in iV_{oc}. As a result, total pressure of 0.1 mbar is chosen for further parameter variation experiments.

THE EFFECTS OF O_2 AND AR GAS FLOW RATIO ON TiO_x CONTACTS

The oxygen content in TiO_x layer has a strong influence on the electron affinity (E_A) which plays a key role on the suitable band alignment between the TiO_x contact and c-Si absorber [11]. Zhu et al.[19] shows E_A and contact resistivity can be reduced by creating oxygen vacancies upon annealing in H_2 and Ar gases which enable favourable conduction band alignment. Alternatively, the oxygen content of TiO_x layer can be controlled in-situ by varying the O_2 to Ar gas ratio. As a result, the surface passivation of TiO_x layers, deposited at $O_2/(Ar+O_2)$ ratio of 0.5 and 1, is investigated on SiO_x:H and a-Si:H(i) interlayers, and shown in Figure 7.9 (a) and (b), respectively. The iV_{oc} of TiO_x/SiO_y:H stacks shows excellent iV_{oc} values of about 700 mV for both $O_2/(Ar+O_2)$ ratio of 0.5 and 1. Note that the higher iV_{oc} is obtained, compared to stacks from Figure 7.8, is mainly assigned to the superior wafer quality. To the authors' knowledge, this is the highest iV_{oc} value obtained for a TiO_x contact with an oxide interlayer. In addition, no dedicated hydrogenation step is required to reach this value. For TiO_x/a-Si:H(i) stack, the iV_{oc} decreases to about 670 mV because of the passivation damage caused during PLD deposition. However, the iV_{oc} slightly improves to pre- a-Si:H(i) deposition values, after an anneal at 190 °C.

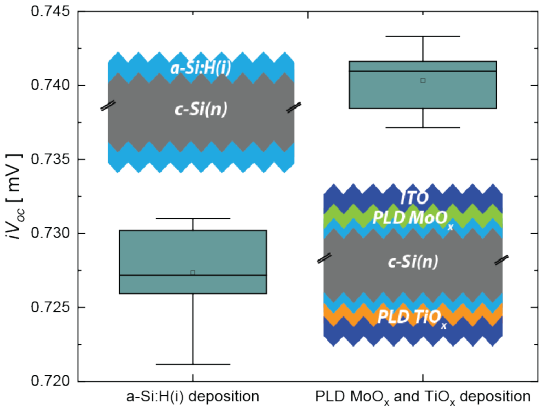

Figure 7.9.: iV_{oc} of solar cell with a PLD front MoO_x contact and a rear PLD TiO_x contact, capped with PLD ITO deposited at 170 °C. PLD MoO_x and TiO_x were deposited at 0.13 and 0.1 mbar, respectively.

7.3.3. PLD MoO_X AND TiO_X CONTACTS SOLAR CELL WITH A-SI:H(i) AS PASSIVATING INTERLAYER.

In this section, PLD MoO_x and TiO_x contacts are evaluated on a half-fabricated solar cell. This solar cell consists of a hole ITO/MoO_x/a-Si:H(i) contact and an electron ITO/TiO_x/a-Si:H(i) contact. Figure 7.9 shows the change in iV_{oc} after the deposition PLD MoO_x and TiO_x layers, as well as ITO films deposition at 170 °C, on an a-Si:H(i) interlayer. An iV_{oc} of approximately 727 mV is achieved following the deposition of a-Si:H(i) on both sides of the Si substrate. Subsequently, the deposited MoO_x and TiO_x layers are capped in-situ with an ITO film. This leads to an excellent achieved average iV_{oc} of 742 mV. The enhanced surface passivation observed after PLD depositions can be attributed to the in-situ annealing treatment at 170°C during ITO deposition and to the soft deposition propreties of PLD which mitigate the induced deposition damage on the surface passivation.

However, it is worth noting that the carrier selectivity of these contacts needs to be optimized, primarily because of the existing carrier-selective losses attributed to the PLD MoO_x. Additionally, the relatively high WF of ITO results in high carrier-selectivity losses when combined with TiO_x contact. Further work is required to improve the carrier-selectivity of the layers. In the case of the MoO_x contact, it is highly likely that the work function (WF) of the layer is too low. Conversely, the e-beam deposited MoO_x demonstrates better WF properties, which could be attributed to the different deposition conditions, such as a lower deposition rate and the absence of background gas. By further reducing the laser fluence, the deposition rate can be reduced which also results in an evaporation-like deposition

[20]. Further work in the low fluency range should be investigated. Additionally, it is essential to comprehensively grasp the effects of various PLD deposition parameters on the structure and WF of the MoO_x layer. To achieve this, characterization tools like ultraviolet photoelectron spectroscopy (UPS) for determining the bulk WF and surface photovoltage (SPV) for assessing induced band bending are essential in understanding the variations caused by different PLD deposition parameters. Conversely, TiO_x contacts, when used in conjunction with both an oxide or an a-Si:H(i) interlayer, need further optimization to achieve a low contact resistance. This optimization involves reducing the thickness of the TiO_x layer, oxygen vacancies formation by further reducing the oxygen partial pressure, and utilizing materials with lower work functions (WF), which can enhance the induced band bending. Additionally, it is necessary to implement a transparent conductive oxide (TCO) with a low work function in combination with TiO_x.

7.4. CONCLUSIONS

In this chapter, the surface passivation and carrier-selectivity properties of MoO_x and TiO_x, as a hole and an electron contact, respectively, are explored by using the PLD technique. The PLD MoO_x contact shows good surface passivation but lacks carrier-selectivity. The hole carrier selectivity of the contact can be improved with increasing O_2 total pressure. However, a noticeable contact selectivity loss and a S-shaped IV curve are observed even for MoO_x deposited at high oxygen deposition total pressure (0.13 mbar). The carrier selectivity loss of the contact is possibly caused by a lack in upward induced band bending. This is caused by a too low WF properties of the deposited MoO_x layer. On the other hand, TiO_x contacts display excellent passivation properties on both a-Si:H(i) and SiO_y:H interlayers at a deposition total pressure of 0.1 mbar. Furthermore, the passivation properties of TiO_x contacts are not affected by varying O_2 to Ar gas ratio which could prove beneficial to improve the transport properties by creation O vacancies in the TiO_x layer. Additionally, a complete metal oxide solar cell, incorporating the MoO_x and TiO_x contacts, has been successfully fabricated, yielding an outstanding iV_{oc} value of 742 mV. However, further improvement in the carrier selectivity of these contacts is needed for high efficiency solar cells.

REFERENCES

[1] M. Taguchi, A. Yano, S. Tohoda, K. Matsuyama, Y. Nakamura, T. Nishiwaki, K. Fujita, and E. Maruyama. “24.7% record efficiency HIT solar cell on thin silicon wafer”. In: *IEEE Journal of photovoltaics* 4.1 (2013), pp. 96–99.

[2] Y. Larionova, H. Schulte-Huxel, B. Min, S. Schaefer, T. Kluge, H. Mehlich, R. Brendel, and R. Peibst. “Ultra-Thin Poly-Si Layers: Passivation Quality, Utilization of Charge Carriers Generated in the Poly-Si and Application on Screen-Printed Double-Side Contacted Polycrystalline Si on Oxide Cells”. In: *Solar RRL* 4.10 (2020), p. 2000177.

[3] M. Köhler, M. Pomaska, P. Procel, R. Santbergen, A. Zamchiy, B. Macco, A. Lambertz, W. Duan, P. Cao, B. Klingebiel, *et al.* “A silicon carbide-based highly transparent passivating contact for crystalline silicon solar cells approaching efficiencies of 24%”. In: *Nature Energy* 6.5 (2021), pp. 529–537.

[4] J. Peter Seif, A. Descoeudres, M. Filipič, F. Smole, M. Topič, Z. Charles Holman, S. De Wolf, and C. Ballif. “Amorphous silicon oxide window layers for high-efficiency silicon heterojunction solar cells”. In: *Journal of Applied Physics* 115.2 (2014), p. 024502.

[5] Y. Zhao, L. Mazzarella, P. Procel, C. Han, G. Yang, A. Weeber, M. Zeman, and O. Isabella. “Doped hydrogenated nanocrystalline silicon oxide layers for high-efficiency c-Si heterojunction solar cells”. In: *Progress in Photovoltaics: research and applications* 28.5 (2020), pp. 425–435.

[6] L. Mazzarella, S. Kirner, B. Stannowski, L. Korte, B. Rech, and R. Schlatmann. “p-type microcrystalline silicon oxide emitter for silicon heterojunction solar cells allowing current densities above 40 mA/cm2”. In: *Applied physics letters* 106.2 (2015), p. 023902.

[7] H. Wernerus, M. Bivour, L. Kroely, M. Hermle, and W. Wolke. “Characterization of ultra-thin μc-Si: H films for silicon heterojunction solar cells”. In: *Energy Procedia* 55 (2014), pp. 310–319.

[8] P. Procel, G. Yang, O. Isabella, and M. Zeman. “Theoretical evaluation of contact stack for high efficiency IBC-SHJ solar cells”. In: *Solar Energy Materials and Solar Cells* 186 (2018), pp. 66–77.

[9] L. Cao, P. Procel, A. Alcañiz, J. Yan, F. Tichelaar, E. Özkol, Y. Zhao, C. Han, G. Yang, Z. Yao, *et al.* “Achieving 23.83% conversion efficiency in silicon heterojunction solar cell with ultra-thin MoOx hole collector layer via tailoring (i) a-Si: H/MoOx interface”. In: *Progress in Photovoltaics: research and applications* (2022).

[10] X. Yang, K. Weber, Z. Hameiri, and S. De Wolf. “Industrially feasible, dopant-free, carrier-selective contacts for high-efficiency silicon solar cells”. In: *Progress in photovoltaics: Research and Applications* 25.11 (2017), pp. 896–904.

[11] Y. Wang, S.-T. Zhang, L. Li, X. Yang, L. Lu, and D. Li. “Dopant-free passivating contacts for crystalline silicon solar cells: Progress and prospects”. In: *EcoMat* (2023), e12292.

[12] D. Scirè, M. Bonadonna, Y. Zhao, P. Procel, O. Isabella, M. Zeman, R. Macaluso, M. Mosca, and I. Crupi. “Analysis of Transition Metal Oxides based Heterojunction Solar Cells with S-shaped JV curves”. In: *2020 AEIT International Annual Conference (AEIT)*. IEEE. 2020, pp. 1–6.

[13] D. Sacchetto, Q. Jeangros, G. Christmann, L. Barraud, A. Descoeudres, J. Geissbühler, M. Despeisse, A. Hessler-Wyser, S. Nicolay, and C. Ballif. “ITO/MoOx/a-Si: H (i) hole-selective contacts for silicon heterojunction solar cells: degradation mechanisms and cell integration”. In: *IEEE Journal of Photovoltaics* 7.6 (2017), pp. 1584–1590.

[14] J. Werner, J. Geissbühler, A. Dabirian, S. Nicolay, M. Morales-Masis, S. D. Wolf, B. Niesen, and C. Ballif. “Parasitic absorption reduction in metal oxide-based transparent electrodes: application in perovskite solar cells”. In: *ACS applied materials & interfaces* 8.27 (2016), pp. 17260–17267.

[15] M. T. Greiner, L. Chai, M. G. Helander, W.-M. Tang, and Z.-H. Lu. “Metal/metal-oxide interfaces: how metal contacts affect the work function and band structure of MoO3”. In: *Advanced Functional Materials* 23.2 (2013), pp. 215–226.

[16] Y. Smirnov, P.-A. Repecaud, L. Tutsch, I. Florea, K. P. Zanoni, A. Paliwal, H. J. Bolink, P. R. i Cabarrocas, M. Bivour, and M. Morales-Masis. “Wafer-scale pulsed laser deposition of ITO for solar cells: Reduced damage vs. interfacial resistance”. In: *Materials Advances* 3.8 (2022), pp. 3469–3478.

[17] X. Yang, Q. Bi, H. Ali, K. Davis, W. V. Schoenfeld, and K. Weber. “High-performance TiO2-based electron-selective contacts for crystalline silicon solar cells”. In: *Advanced Materials* 28.28 (2016), pp. 5891–5897.

[18] J. Bullock, Y. Wan, Z. Xu, S. Essig, M. Hettick, H. Wang, W. Ji, M. Boccard, A. Cuevas, C. Ballif, *et al.* “Stable dopant-free asymmetric heterocontact silicon solar cells with efficiencies above 20%”. In: *ACS Energy Letters* 3.3 (2018), pp. 508–513.

[19] W.-D. Zhu, C.-W. Wang, J.-B. Chen, D.-S. Li, F. Zhou, and H.-L. Zhang. “Enhanced field emission from hydrogenated TiO2 nanotube arrays”. In: *Nanotechnology* 23.45 (2012), p. 455204.

[20] R. Eason. *Pulsed laser deposition of thin films: applications-led growth of functional materials*. John Wiley & Sons, 2007.

8

CONCLUSIONS AND OUTLOOK

8.1. CONCLUSIONS

IN the pursuit of enhancing the conversion efficiency of crystalline silicon (c-Si) solar cells, it has become imperative to mitigate parasitic absorption losses within the contact materials. Simultaneously, it is crucial to uphold the excellent surface passivation and carrier selectivity characteristics commonly observed in, for instance, Silicon Heterojunction (SHJ) cells. This thesis delves into diverse strategies designed to minimize these losses, providing a concise overview outlined as follows:

- Firstly, an ultra-thin Al_2O_3/SiO_y interlayer was developed as a possible replacement for the intrinsic hydrogenated amorphous Si (a-Si:H(i)) interlayer, for a MoO_x contact. Chapter 3 highlights the advantages of this contact, including excellent thermal stability (up to 210 °C) and stack transparency. The $MoO_x/Al_2O_3/SiO_y$ contact exhibits an initial solar cell efficiency of 18.2% and an open circuit voltage (V_{oc}) of 650 mV. The excellent carrier-selectivity of this contact is explained in Chapter 4 and shows that the interlayer allows for efficient transport of hole majority carriers through the interlayer. To further improve the surface passivation of the interlayer, a hydrogenation strategy is developed as described in Chapter 5. This strategy allows for the hydrogenation of the oxide interlayer prior to the MoO_x deposition; a pre-hydrogenation of the interlayer is essential because MoO_x tends to react with hydrogen which results in the layer work function degradation. By etching the Al_2O_3 bulk layer in a diluted TMAH solution, the highly passivated SiO_y interlayer can be utilized to form a passivating MoO_x contact stack. As a result, excellent implied V_{oc} (iV_{oc}) of 710 mV was obtained on symmetric textured n-type Czochralski Si samples.

- Another aspect, focused on reducing parasitic absorption losses, is the development of an ultra-thin poly-Si contact (<20 nm) combined with an indium tin oxide (ITO) layer deposited using pulsed laser deposition (PLD). The PLD technique proves to be advantageous due to its gentle deposition properties, minimizing surface passivation damage that typically occurs when ITO is deposited on ultra-thin poly-Si contacts. Even on a 10 nm thick

poly-Si layer, the post-deposition damage is significantly reduced compared to sputter-deposited ITO layers. By increasing the ITO deposition pressure, further damage reduction is achievable. Remarkably low contact resistivity (~45 mOhm.cm^2) and excellent thermal stability (up to 350 °C) are also achieved. Additionally, the ITO layer exhibits exceptional opto-electrical properties, with a resistivity of 4.9 × 10^{-4} Ohm.cm and a mobility of 42.1 cm^2/Vs, even at higher repetition rates and laser fluency, required for higher deposition rates.

- Finally, this thesis delves into hole-collecting MoO_x and electron-collecting TiO_x contacts deposited by PLD and their application to c-Si solar cells. PLD offers numerous advantages due to its versatility in deposition parameters and its gentle deposition properties, which can be beneficial for sensitive underlying layers. The carrier selectivity of the MoO_x contact can be enhanced by increasing the deposition pressure, resulting in a more stoichiometric layer. Nevertheless, at oxygen total pressures higher than 0.13 mbar, the MoO_x contact does not show any further improvement in terms of carrier selectivity, thereby resulting in a $\Delta V_{oc}(iV_{oc}\text{-}V_{oc})$ of approximately 50 mV and an S-shaped IV curve. While this selectivity loss could be attributed to the formation of a parasitic oxide at the MoO_x/a-Si:H(i) interface, caused by the increasing O_2 deposition pressure, further variations in parameters suggest that the origin of the selectivity loss is mainly due to a deficiency in the layer's work function. On the other hand, the TiO_x contact demonstrates effective surface passivation with iV_{oc} values of about 700 mV and 730 mV on SiO_y:H and a-Si:H(i) interlayers, respectively. However, additional optimization of the contact is required to reduce the series resistance present at the a-Si:H(i) interlayer.

8.2. OUTLOOK

8

Throughout this PhD research, several recommendations have been conceived, as described as follows:

- Improving the tunneling transport of MoO_x/SiO_y:H contact

  To create a high-quality passivating MoO_x based contact stack, a SiO_y:H interlayer was formed after Al_2O_3 etching in a 1% diluted TMAH solution at 60 °C for 1 min. Although excellent surface passivation can be achieved by using this approach, further etching optimization is required to reduce the contact resistivity of the MoO_x contact stack. This can be attained by reducing the thickness of the SiO_y:H interlayer thereby allowing for improved tunneling transport. A SiO_y layer etches slowly in TMAH which allows for effective thickness control. Tetzalaff et al.[1] showed that SiO_2 layer etches at a rate of about 0.1 nm/min in a 5% diluted TMAH solution. Nevertheless, prolonged etching could also impact the surface passivation of the interlayer and is ought to be considered.

- Development of ultra-thin poly-Si contacts

Alternatively, parasitic absorption losses can be mitigated by the utilization of ultra-thin poly-Si contact (<20 nm). Although post-deposition of TCOs can induce surface passivation degradation on poly-Si contacts, PLD presents a soft deposition alternative to mitigate the passivation losses independent from the thickness of the poly-Si layer. However, the doping profile of thinner poly-Si should be optimized to improve the carrier-selectivity of the contact; a shallow doping profile is observed for the thinner layer which has resulted in a higher contact resistivity (298.6 mOhm.cm^2 was obtained for the 10 nm thick poly-Si(n+) in comparison to 54.9 mOhm.cm^2 for the 20 nm layer). Several improvements, such as increase in the doping concentration of the preceding a-Si:H(n+) layer - to enable a deeper phosphorus diffusion inside the c-Si absorber, or higher crystallization temperature can be applied to improve the contact resistivity for thinner layers. Additionally, because of the low abundance and increasing cost of indium material, alternative In-free TCO layers should be developed. Al-doped ZnO (AZO) layer has been prominently developed and has shown to provide good surface passivation on thin poly-Si contacts [2]. However, further development is required to improve the carrier mobility of the layer and the stability issues [3]. AZO layer mobility of about 13.8 cm^2/Vs was initially obtained after PLD deposition while being thermally stable to temperatures up to 350 °C.

- Optimization of metal oxide materials properties

  For dopant-free passivating contacts, several efforts are still required to accurately tune their electrical properties. Despite the wide range of dopant-free materials that have been explored, this technology still lacks maturity. Further computational simulation efforts are essential to gain a comprehensive understanding of the intricate interaction between metal oxide layers and surface passivating interlayers, as this interplay can significantly influence the charge carrier transport of the contact. Moreover, experimental works are required to actively tune the WF and electronic bands of these layers. Several strategies such as, doping, chemical potential tuning (oxygen tuning in the case of MoO_x and TiO_x), or combining different materials properties could be promising solutions to tackle these issues. The latter has shown great promises. For instance, Li et al.[4] showed the benefits of combining the high WF properties of MoO_x and the large conduction band properties of NiO_x layer, to improve to hole-carrier selectivity of the contact.

  PLD presents various merits to further tune the electrical and chemical properties of these dopant-free materials. However, an extensive analysis is required to understand the effects of these deposition parameters on the electronic properties of the MoO_x and TiO_x layers. PLD MoO_x contacts show limited carrier selectivity properties and require further deposition parameter tuning to improve the WF of the contact. A wider deposition parameter space should be explored and additional understanding of the influences of these parameters on the MoO_x electronic properties is needed. For TiO_x contact, it has to be ensured that the layer consist of sufficient O vacancies

thereby decreasing the layer WF and enhancing the electron transport[5]. PLD TiO_x/a-Si:H(i) contact shows excellent surface passivation properties. However, this structure results in a high contact resistance and requires further tuning. Possible strategies such as, a thinner a-Si:H(i), and insertion of a low WF material, such as LiF, Ca, or Mg can be beneficial to improve the contact properties [6–8]. On the other hand, replacing the a-Si:H(i) by a SiO_y:H interlayer should be beneficial because of a favorable band alignment with the Si absorber [9].

- Application of PLD in thin film solar cells

  Significant efforts have been initiated to explore the benefits of PLD technique in thin film photovoltaic technologies, such as perovskite solar cells [8, 10–14]. As mentioned above, the main advantages of PLD are represented by its soft deposition properties to adjacent layers, excellent stoichiometry transfer from material target to layer formation, and the ability to deposit a wide range of materials. The latter is very promising since all active layers i.e. transparent electrodes [10], carrier transport layers [15], and perovskite layers [14] can be deposited – which has the potential to reduce the fabrication costs. This is because the fabrication of perovskite solar cells commonly require multiple deposition techniques for the various active layers. Nonetheless, a considerable obstacle to achieving high deposition throughput lies in the limited angular distribution of the PLD plume, acting as a bottleneck for the efficient line-to-line production of solar cells; the size of the laser ablation constrains the spot size on the target, consequently restricting the plume area to a few square centimeters. This is further exacerbated by the continuous increase in wafer size. Currently, substantial advancements are underway to enhance the throughput capabilities of PLD through techniques such as optically combining multiple lasers or expanding the laser beam in a single direction [16].

  While the integration of PLD into solar cell manufacturing is still in the nascent stages, it stands out as an excellent deposition tool for delving into material properties. Insights gained from such exploration can eventually be translated to high-throughput technologies like ALD and sputtering.

REFERENCES

[1] D. Tetzlaff, M. Dzinnik, J. Krügener, Y. Larionova, S. Reiter, M. Turcu, R. Peibst, U. Höhne, J.-D. Kähler, and T. F. Wietler. "Introducing pinhole magnification by selective etching: application to poly-Si on ultra-thin silicon oxide films". In: *Energy Procedia* 124 (2017), pp. 435–440.

[2] E. Bruhat, T. Desrues, D. Blanc-Pélissier, B. Martel, R. Cabal, and S. Dubois. "Contacting n+ poly-Si junctions with fired AZO layers: a promising approach for high temperature passivated contact solar cells". In: *2019 IEEE 46th Photovoltaic Specialists Conference (PVSC)*. IEEE. 2019, pp. 2319–2324.

[3] A. B. Morales-Vilches, A. Cruz, S. Pingel, S. Neubert, L. Mazzarella, D. Meza, L. Korte, R. Schlatmann, and B. Stannowski. "ITO-free silicon heterojunction solar cells with ZnO: Al/SiO 2 front electrodes reaching a conversion efficiency of 23%". In: *IEEE Journal of Photovoltaics* 9.1 (2018), pp. 34–39.

[4] L. Li, G. Du, Y. Lin, X. Zhou, Z. Gu, L. Lu, W. Liu, J. Huang, J. Wang, L. Yang, *et al.* "NiOx/MoOx bilayer as an efficient hole-selective contact in crystalline silicon solar cells". In: *Cell Reports Physical Science* 2.12 (2021), p. 100684.

[5] M. T. Greiner, L. Chai, M. G. Helander, W.-M. Tang, and Z.-H. Lu. "Metal/metal-oxide interfaces: how metal contacts affect the work function and band structure of MoO3". In: *Advanced Functional Materials* 23.2 (2013), pp. 215–226.

[6] Y. Nakagawa, K. Gotoh, T. Inoue, Y. Kurokawa, and N. Usami. "Improved Performance of Titanium Oxide/Silicon Oxide Electron-Selective Contacts by Implementation of Magnesium Interlayers". In: *physica status solidi (a)* 218.19 (2021), p. 2100296.

[7] T. G. Allen, J. Bullock, Q. Jeangros, C. Samundsett, Y. Wan, J. Cui, A. Hessler-Wyser, S. De Wolf, A. Javey, and A. Cuevas. "A low resistance calcium/reduced titania passivated contact for high efficiency crystalline silicon solar cells". In: *Advanced Energy Materials* 7.12 (2017), p. 1602606.

[8] W. Wang, J. He, D. Yan, C. Samundsett, S. P. Phang, Z. Huang, W. Shen, J. Bullock, and Y. Wan. "21.3%-efficient n-type silicon solar cell with a full area rear TiOx/LiF/Al electron-selective contact". In: *Solar Energy Materials and Solar Cells* 206 (2020), p. 110291.

[9] Y. Wang, S.-T. Zhang, L. Li, X. Yang, L. Lu, and D. Li. "Dopant-free passivating contacts for crystalline silicon solar cells: Progress and prospects". In: *EcoMat* (2023), e12292.

[10] Y. Smirnov, L. Schmengler, R. Kuik, P.-A. Repecaud, M. Najafi, D. Zhang, M. Theelen, E. Aydin, S. Veenstra, S. De Wolf, *et al.* “Scalable pulsed laser deposition of transparent rear electrode for perovskite solar cells”. In: *Advanced Materials Technologies* 6.2 (2021), p. 2000856.

[11] H. Wang, Y. Wu, M. Ma, S. Dong, Q. Li, J. Du, H. Zhang, and Q. Xu. “Pulsed laser deposition of CsPbBr3 films for application in perovskite solar cells”. In: *ACS Applied Energy Materials* 2.3 (2019), pp. 2305–2312.

[12] M. Feng, M. Wang, H. Zhou, W. Li, S. Wang, Z. Zang, and S. Chen. “High-efficiency and stable inverted planar perovskite solar cells with pulsed laser deposited Cu-doped NiO x hole-transport layers”. In: *ACS Applied Materials & Interfaces* 12.45 (2020), pp. 50684–50691.

[13] H. Zhang, H. Wang, M. Ma, Y. Wu, S. Dong, and Q. Xu. “Application of compact TiO2 layer fabricated by pulsed laser deposition in organometal trihalide perovskite solar cells”. In: *Solar RRL* 2.8 (2018), p. 1800097.

[14] T. Soto-Montero, S. Kralj, W. Soltanpoor, J. S. Solomon, J. S. Gómez, K. P. Zanoni, A. Paliwal, H. J. Bolink, C. Baeumer, A. P. Kentgens, *et al.* “Single-Source Vapor-Deposition of MA1–xFAxPbI3 Perovskite Absorbers for Solar Cells”. In: *Advanced Functional Materials* (2023), p. 2300588.

[15] Z. Qiu, H. Gong, G. Zheng, S. Yuan, H. Zhang, X. Zhu, H. Zhou, and B. Cao. “Enhanced physical properties of pulsed laser deposited NiO films via annealing and lithium doping for improving perovskite solar cell efficiency”. In: *Journal of Materials Chemistry C* 5.28 (2017), pp. 7084–7094.

[16] N. A. Shepelin, Z. P. Tehrani, N. Ohannessian, C. W. Schneider, D. Pergolesi, and T. Lippert. “A practical guide to pulsed laser deposition”. In: *Chemical Society Reviews* (2023).

A

APPENDIX

This appendix provides additional information based on Chapter 3. It can also be found in the publication of Solar Energy Materials & solar cells.

A.1. PASSIVATION OF ALO_X/MOO_X STACK

Here, we show the effect of annealing temperature on the passivation properties of the interlayer. The AlOx layers were deposited on textured Cz Si(n) wafers and annealed at different temperatures. Subsequently, a thin layer of MoO_x was evaporated on both sides of the samples. In Figure A.1, the effective lifetime (τ_{eff}) was measured for the thermally treated AlO_x layers before and after MoO_x deposition. The passivation level of the AlO_x interfacial layers are rather low after a thermal treatment although a general increase in passivation is observed with increasing annealing temperature. The lack of passivation of tunneling layers are not uncommon and has been previously reported by Young et al. [1]. However, after the deposition of the MoO_x films, a general improvement in τ_{eff} is measured for the samples and is mostly due to an inversion layer created near the Si interface [2, 3]. Here, we can fairly assume that the deposited MoO_x film solely contributes to a field effect passivation since evaporated MoO_x has poor chemical passivation properties [4]. A clear increase in τ_{eff} is observed with T_{PDA} which implies that the thermal treatment on the AlO_x interfacial layer is beneficial to passivates the dangling bonds present at the Si interface.

A

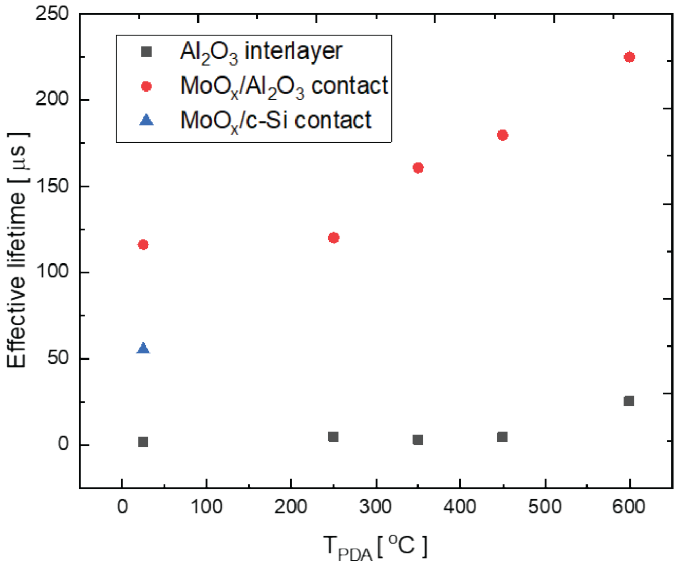

Figure A.1.: Effective lifetime of symmetric textured Cz *n*-type wafers at different deposition and treatment stages i.e. post AlO_x PDA, MoO_x deposition, and post anneal at 190 °C in ambient conditions.

REFERENCES

[1] D. L. Young, W. Nemeth, S. Grover, A. Norman, B. G. Lee, and P. Stradins. “Carrier-selective, passivated contacts for high efficiency silicon solar cells based on transparent conducting oxides”. In: *2014 IEEE 40th photovoltaic specialist conference (PVSC)*. IEEE. 2014, pp. 1–5.

[2] T. Sun, R. Wang, R. Liu, C. Wu, Y. Zhong, Y. Liu, Y. Wang, Y. Han, Z. Xia, Y. Zou, *et al.* “Investigation of MoOx/n-Si strong inversion layer interfaces via dopant-free heterocontact”. In: *physica status solidi (RRL)–Rapid Research Letters* 11.7 (2017), p. 1700107.

[3] L. G. Gerling, S. Mahato, A. Morales-Vilches, G. Masmitja, P. Ortega, C. Voz, R. Alcubilla, and J. Puigdollers. “Transition metal oxides as hole-selective contacts in silicon heterojunctions solar cells”. In: *Solar Energy Materials and Solar Cells* 145 (2016), pp. 109–115.

[4] L. G. Gerling, C. Voz, R. Alcubilla, and J. Puigdollers. “Origin of passivation in hole-selective transition metal oxides for crystalline silicon heterojunction solar cells”. In: *Journal of Materials Research* 32 (2017), pp. 260–268.

B

APPENDIX

This appendix is based on Chapter 4. To determine to effect of band bending caused by the passivating interlayer, we use a corona charging setup by Delft spectral technologies for samples shown in Figure B.1. Further details about the corona charging tool can be found in [1–4]. The samples with AlO_x, SiO_2, and a-Si:H(i) interlayers were capped with MoO_x, a thin layer of ITO, and 6 nm of AlO_x to reduce the dissipation of charges.

Note here that $S_{\text{eff,max}}$ was calculated from the wafer thickness W and the effective minority carrier lifetime τ_{eff} ($S_{\text{eff,max}} = W/2\tau_{\text{eff}}$) after conducting quasi-steady state photoconductance (QSSPC) measurements using a Sinton WCT-120TS setup in the generalized (1/64) mode. For the QSSPC measurements we assumed n-type substrates, a wafer thickness of 200 µm, an optical constant of 0.55 (for chemically polished substrates) and the τ_{eff} values at an injection level of $1{\cdot}10^{15}$ cm^{-3} were used for the calculation of $S_{\text{eff,max}}$.

We have conducted positive charging on both sides of all samples in an attempt to derive the fixed charge density (Q_f). Figure B.2 shows the effect of the cumulative induced positive charges on the S_{eff} of the samples. However, the fixed charge density could not be reliably determined for these samples due to a minimal change in passivation quality after charge deposition combined with leaky behavior. As a result, no increase in $S_{\text{eff,max}}$ is observed with increasing cumulative corona charging time. For samples without ITO, a better degradation of S_{eff} can be observed by which the $S_{\text{eff,max}}$ is determined after 600s. Nevertheless, the amplitude of the curve is rather small resulting in a high uncertainty.

To estimate the amount of deposited corona charge up until the maximum in $S_{\text{eff,max}}$ is reached, the increase in the Kelvin probe voltage V_{KP} over time is linearly fitted, as is shown in Figure B.3. Although the resulting fit does not clearly follow a linear trend, this kind of approximation is anyway used to estimate the change in V_{KP} that is required for the evaluation of fixed charged density (Q_f). The poor quality of the linear fit further illustrates that the error on the Q_f value that will be calculated below should only be taken as a lower limit. Furthermore, it is interesting how the slope of the fitted line corresponds to the approximate slope corresponding to the samples with ITO/AlO_x capping, while beyond 600 s the uncapped MoO_x layer is not able to retain any additional charge due to leaky behavior. Following the

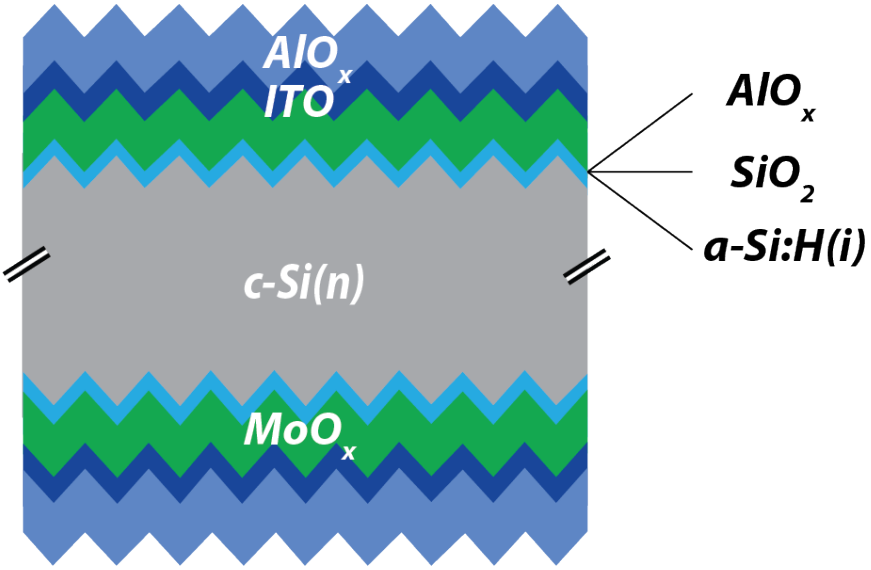

Figure B.1.: Symmetric samples consisting of AlO_x, SiO_2, and a-Si:H(i) interlayers, capped with MoO_x, ITO, and AlO_x.

plotted fitting approach, the total amount of deposited corona charge is estimated from the difference in V_{KP} between the value at the start of the experiment and the value after 600 s of charging using the slope of the fitted line: ΔV_{KP} = 7.075 · 10^{-4} x 600 = 0.424 V. Note here that 600 s is the point in the experiment where the maximum in $S_{eff,max}$ is reached that can in turn be used to calculate Q_f, as follows:

$$Q_{corona} = \frac{\varepsilon_r \varepsilon_0}{d} . \frac{V_{VP}}{e} \tag{B.1}$$

Where ε_0 is the vacuum permittivity (8.854x10^{-12} Fm^{-1}), ε_r is the relative permittivity of MoO_x (18), d is the thickness of the layer stack (5 nm), and e is the elementary charge. Since the deposited corona charge counteracts the fixed charge that is initially present in the layer stack, it holds that Q_f = -2.0 ± 1.0 x 10^{12} cm^{-2}. This moderately negative fixed charge could be associated with traps in the MoO_x layer that are being filled in the corona charging experiment. If this is correct, other variations in the MoO_x layer properties, such as what is induced by different growth temperatures, and their possible impact on Q_f could become detectable by further corona charging experiments.

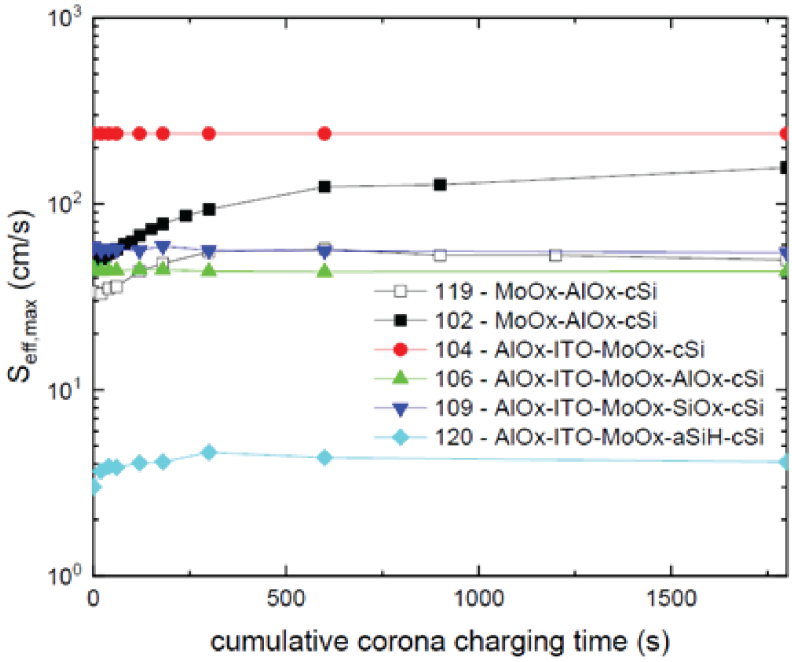

Figure B.2.: S_{eff} against cumulative charge deposition time for MoO_x samples.

B

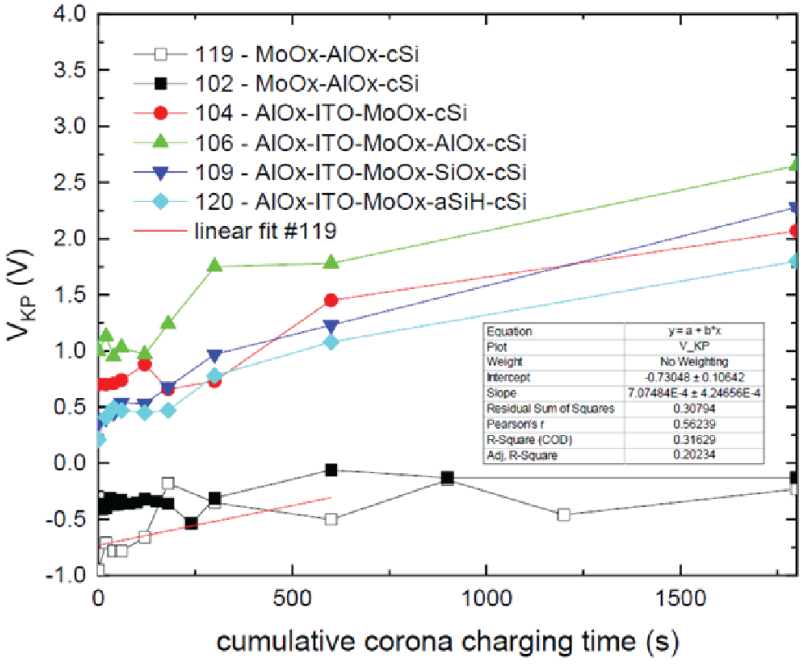

Figure B.3.: V_{KP} as a function of cumulative corona charging time for MoO_x contacts with different interlayers.

REFERENCES

[1] W. J. Berghuis, J. Melskens, B. Macco, R. J. Theeuwes, M. A. Verheijen, and W. M. Kessels. “Surface passivation of germanium by atomic layer deposited Al 2 O 3 nanolayers”. In: *Journal of Materials Research* 36 (2021), pp. 571–581.

[2] W. J. Berghuis, M. Helmes, J. Melskens, R. J. Theeuwes, W. M. Kessels, and B. Macco. “Extracting surface recombination parameters of germanium–dielectric interfaces by corona-lifetime experiments”. In: *Journal of Applied Physics* 131.19 (2022), p. 195301.

[3] W. J. Berghuis, J. Melskens, B. Macco, R. J. Theeuwes, L. E. Black, M. A. Verheijen, and W. M. Kessels. “Excellent surface passivation of germanium by a-Si: H/Al2O3 stacks”. In: *Journal of Applied Physics* 130.13 (2021), p. 135303.

[4] J. Melskens, R. J. Theeuwes, L. E. Black, W.-J. H. Berghuis, B. Macco, P. C. Bronsveld, and W. Kessels. “Excellent Passivation of n-Type Silicon Surfaces Enabled by Pulsed-Flow Plasma-Enhanced Chemical Vapor Deposition of Phosphorus Oxide Capped by Aluminum Oxide”. In: *physica status solidi (RRL)–Rapid Research Letters* 15.1 (2021), p. 2000399.

C

APPENDIX

This appendix is based on chapter 6. The doping profile of thinner poly-Si should be optimized to improve the carrier-selectivity of the contact. Figure C.1 shows the doping profile for our 10 and 20 nm thick poly-Si(n+) contacts. A shallow profile is observed for the thinner layer which has resulted in a higher contact resistivity; 298.6 mOhm.cm^2 was obtained for the 10 nm thick poly-Si(n+) in comparison to 54.9 mOhm.cm^2 for the 20 nm layer. However, the doping profiles of the 10 nm

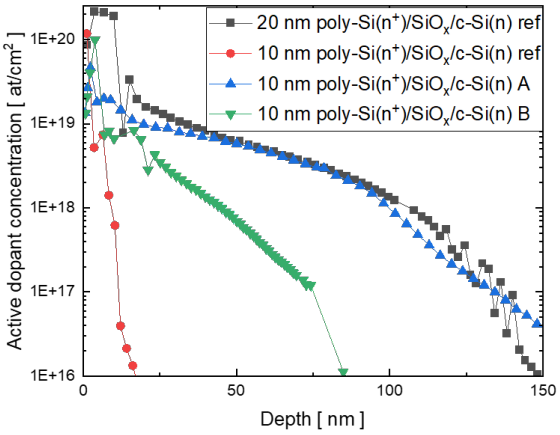

Figure C.1.: Doping profiles of 10 and 20 nm thick poly-Si(n+) standard (Oxide formation and crystallization temperatures are 610 °C and 900 °C, respectively) layers, 10 nm poly-Si(n+) A (Oxide formation and crystallization temperatures are 610 °C and 950 °C, respectively)) and B (Oxide formation and crystallization temperatures are 550 °C and 950 °C, respectively)) measured by Electrochemical Capacitance-Voltage.10 nm poly-Si(n+) B contact was formed with a high doped a-Si:H(n+) layer.

thick poly-Si contacts can be improved by increasing the poly-Si(n+) crystallization temperature from 900 to 950 °C, resulting in similar profile to the 20 nm poly-Si(n+) layer.

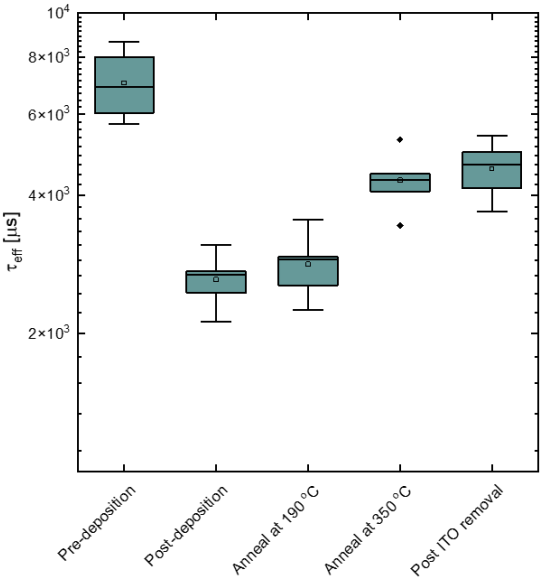

Figure C.2.: Effective lifetime (τ_{eff}) of 20 nm poly-Si contacts after annealing treatments and post-ITO removal.

The effect of work function mismatch can result in a reduction in charge carrier lifetime of the poly-Si contact. Consequently, the deposited ITO layer was etched off to determine if the reduced lifetime of the poly-Si contact could caused by a work function mismatch between the poly-Si(n+) and ITO layer. Figure C.2 shows the effective lifetime (τ_{eff}) of the poly-Si(n+) contact after the ITO layer was etched off. No major improvement in τ_{eff} is observed which indicates that minimal influence of the work function mismatch.

D

APPENDIX

As shown in Figure D.1, the transmittance of the layers depends strongly on the oxygen pressure in the chamber. A less strong, but for the best layers still relevant effect of the substrate temperature can also be observed. The best samples are made at high O_2 pressure and room temperature.

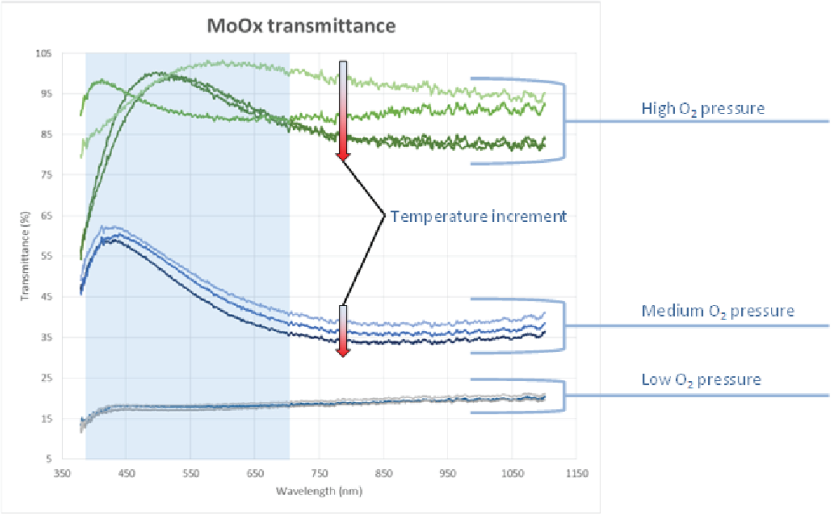

Figure D.1.: Transmittance measurements for MoO_x layers deposited on glass in the small PLD reactor at MESA+. A clear trend can be observed as a function of O_2 pressure and temperature indicating better stoichiometry at lower temperature and higher O_2 pressure.

D.1. PLD MoO_X PARAMETERS VARIATION

The repetition rate, laser fluence and O_2 to Ar gas ratio (defined as O_2/(Ar+O_2) ratio) is explored in the intent to further improve the carrier selectivity of PLD MoO_x contact. Figure D.2 shows the iV_{oc}, $sunsV_{oc}$, and the ΔV_{oc} of the solar cells for different repetition rates before (Figure 7.7 a, c, e) and after annealing at 190 °C(Figure 7.7 b, d, f). After MoO_x and ITO depositions on the front side, the iV_{oc} decreases without showing distinct dependence on laser repetition rate and gas ratio. iV_{oc} can be recovered to about 720 mV after anneal for all samples. In terms of $sunsV_{oc}$, samples with MoO_x deposited at 50 Hz initially exhibit lower values in comparison to samples with lower repetition rate. However, no difference is observed after a post-anneal, as cell precursors achieved an average $sunsV_{oc}$ of about 650 mV and ΔV_{oc} above 50 mV.

Smirnov et al. [1] showed that high O_2 deposition pressure (0.1 mbar) can result in the formation of a parasitic oxide at the a-Si:H interface thereby limiting the transport of majority carriers to the electrode. Here, no change in carrier selectivity is observed with changing O_2/(Ar+O_2) ratio. This is likely indicates that the formation of an oxide at the MoO_x/a-Si:H(i) interface is likely not the limiting factor.

D.2. E-BEAM DAMAGE AL DEPOSITION

Figure D.3 shows the iV_{oc} of at different stages of cell manufacturing. Because of the lack of accessibility to a thermal evaporator, Al was deposited with our e-beam evaporator, Al was deposited with our e-beam evaporator which can result in x-ray induced damage. Consequently, the damage caused by the e-beam deposition is accounted. 10 nm Al blanket was initially deposited which is suitable to measure the photoconductance of the sample. Prior to Al deposition, excellent iV_{oc} of about 730 mV is obtained. However, after e-beam Al deposition, the iV_{oc} drastically decreases because of the significant x-ray passivation damage generated during the evaporation of Al. In comparison, MoO_x has a low sublimation temperature, and therefore, requires low e-beam deposition power (3 magnitude lower than Al) to result in evaporation. As a result, minimal evaporation damage is observed with e-beam MoO_x deposition (as shown in Chapter 5) in comparison to Al deposition. A post-anneal treatment at 190 °C is only able to partially recover the induced passivation damage.

D.3. TiO_X-BASED SOLAR CELLS WITH A-SI:H(i) INTERLAYER

To explore the electron-selectivity and surface passivation properties of the Al/TiO_x/a-Si:H(i) contact, an a-Si:H(i/p)/ITO stack was deposited on the front side of the solar cell. Note that Al, deposited by e-beam, is used as a back electrode because of its low WF properties (~4.1 eV). However, significant surface passivation damage is observed because of the x-ray emission during the Al deposition, as shown in Appendix D. Figure D.4 depict the IV characteristics of the solar cells with 1.5 and 3 nm thick TiO_x layers after a post-annealing treatment at 190 °C. Solar cells with a 3 nm thick TiO_x layer shows minimum difference in ΔV_{oc} but a low FF

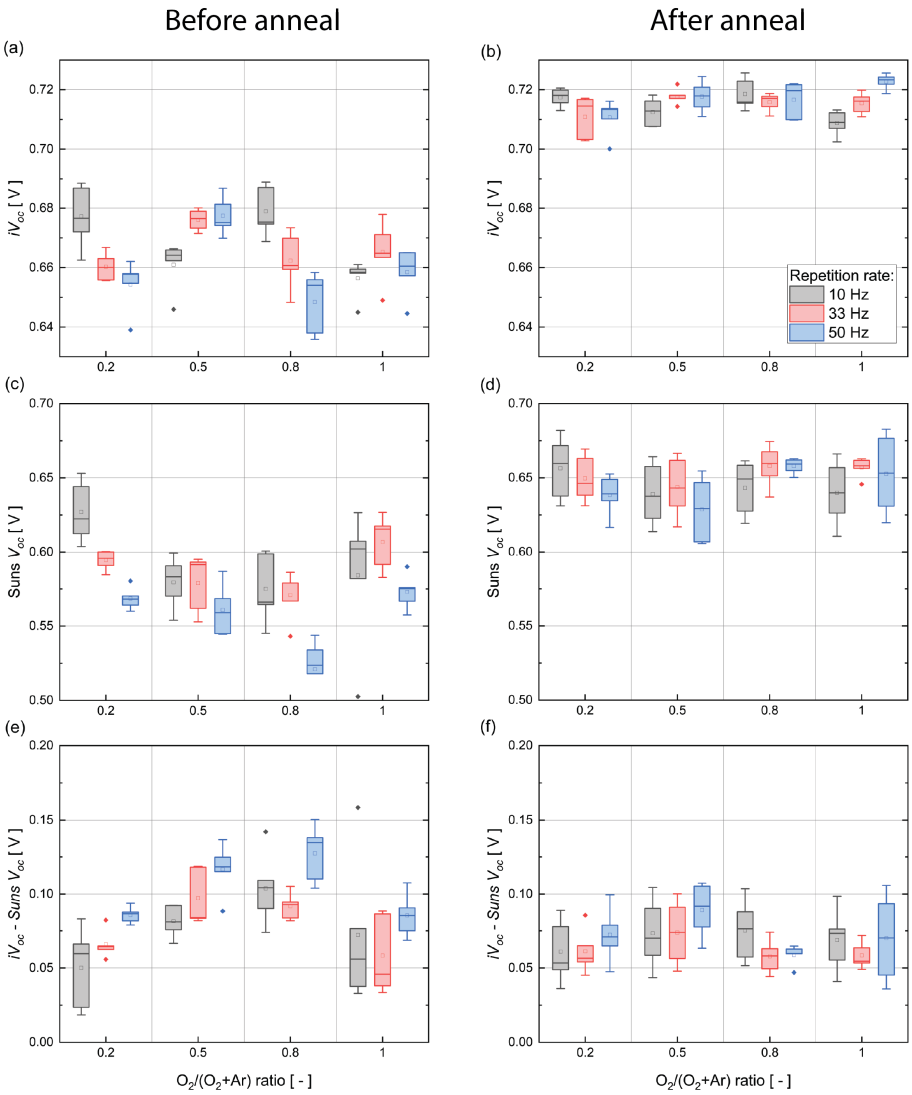

Figure D.2.: Cell precursors with MoO_x layer deposited with varying repetition rate (10 – 50 Hz) and $O_2/(O_2+Ar)$ ratio (0.2 – 1) parameters showing iV_{oc} (a,b), $sunsV_{oc}$ (c,d), and ΔV_{oc} (e,f) values, before and after anneal at 190 °C. Laser fluence and pressure were set at 1.43 mJ/cm^2 and 0.1 mbar, respectively.

which is caused by a high series resistance. The efficiency of the solar cell improves by reducing the thickness of the TiO_x to 1.5 nm, as FF increases from 31.8 to 44.6 %. The high contact resistance of the Al/TiO_x/a-Si:H(i) can also be ascribed to the unoptimized a-Si:H(i) interlayer. Boccard et al.[2] showed that the cell performance of a Al/TiO_x/a-Si:H(i) contact can be improved by reducing the a-Si:H(i) interlayer to

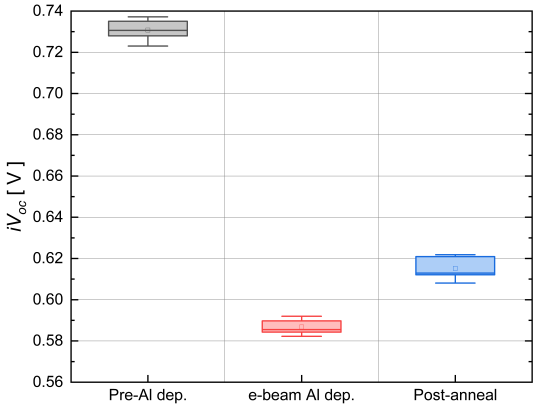

Figure D.3.: iV_{oc} of solar cell with TiO_x contact at different manufacturing stages. TiO_x was deposited at RT, pressure of 0.1 mbar, $O_2/(Ar+O_2)$ ratio = 1, and with laser fluence and repetition rate of 1.43 J/cm^2 and 20 Hz, respectively.

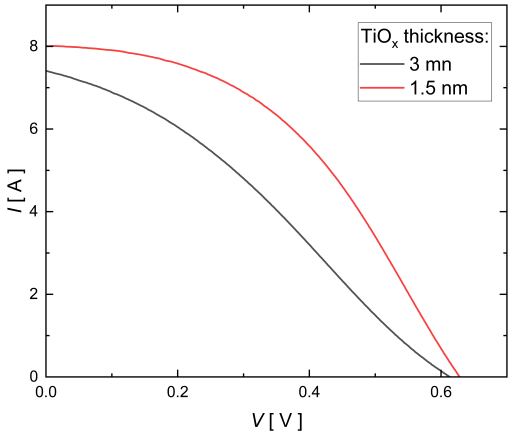

Figure D.4.: IV curve of solar cells with 1.5 and 3 nm TiO_x contact after a post-anneal at 190 °C.

3 nm thick (in comparison 10 nm thick a-Si:H(i) was used in this work). Additionally, further improvement in carrier-selectivity can be achieved by utilizing ultra-thin low WF layers such as, Calcium or LiF when deposited between the TiO_x and Al layers – enabling favourable downward band bending.

ACKNOWLEDGEMENTS

After many years of hard work and dedication, I am finally able to express my heartfelt gratitude to those who have been instrumental in the completion of my doctoral thesis. Without their unwavering support and encouragement, this achievement would not have been possible.

First and foremost, I extend my deepest thanks to my promotors. **Arthur**, your personal mentorship and professional guidance have been invaluable throughout this challenging journey. Your profound knowledge and calm demeanor have consistently provided me with direction and clarity. **Miro**, your insightful wisdom and encouragement have been a true source of inspiration, motivating me to see this endeavor through to its completion.

Furthermore, I would like to extend my sincere thanks to **Paula** for introducing me to the fascinating world of solar cells. I truly enjoyed exploring different hypotheses with you, especially during our bus rides to Petten. Your enthusiasm and motivation were pivotal in my decision to pursue this path. I am particularly grateful for your initiative in writing the COMPASS, RADAR, and MOMENTUM proposals—this dissertation would not have been possible without your belief in me.

I would also like to acknowledge the full support of the team at ECN, which played a significant role in my decision to pursue a PhD. **Eelko**, your kindness and willingness to assist me whenever possible made a tremendous difference. I am especially grateful for the beach volleyball matches you organized and the dinners by the beach afterward—they were a great way to stay in shape and unwind. I also extend my heartfelt thanks to **Astrid**, **Benjamin**, **Maarten**, and **Bas**, who were essential to the fabrication of our solar cells and made me feel truly at home.

After the transition to TNO, I had the privilege of working with **Jimmy** and **Agnes**, both of whom played vital roles in my journey. **Jimmy**, your knowledge and pragmatism were crucial in advancing our research, ultimately leading to important publications. I am also grateful for the car rides from Haarlem and the engaging conversations, especially during the pandemic. I also thoroughly enjoyed our occasional glasses of whiskey. **Agnes**, you took over the research on metal oxide contacts and kept me motivated throughout. I deeply appreciate your support.

I'm also grateful to have worked with the consortium team, whose collective efforts and insights have been a source of inspiration throughout this journey. I would like to extend special thanks to **Bart**, **Olindo**, **Guangtao**, **Paul**, and **Thomas**, whose contributions were pivotal to this work. Their expertise in carrying out deposition processes and measurements significantly deepened my knowledge and understanding, for which I am truly appreciative.

I also owe a great deal to my students, some of whom have contributed as co-authors. **Jons**, you were my first student, and while I was teaching you the physics

of solar cells, you taught me how to become a better teacher. Your contributions to developing a damage-free TCO deposition were immense, and your meticulous yet nonchalant character will undoubtedly serve you well in your future endeavors. **Ruben**, though different from **Jons**, you made significant strides in the development of PLD metal oxide layers, providing us with valuable insights into their behavior. Finally, **Farah**, your excellent work ethic and determination were instrumental in improving the PLD tool. Your contributions were truly invaluable.

I would also like to thank my friends for their constant support throughout this journey. While separated by lands and seas, we managed to form a family. **Elias**, you are a brother to me. While I didn't think we would get along from the day I met you, you have proven me wrong through all the shared moments and adventures. You and **Dani** are a match made in Catalunya, and **Dani**, your kind-hearted nature is something I deeply admire—never change that. And thank you both for allowing me to stay in your home.

A big thanks to **Elisa** for your companionship and for helping me grow as a person. You are a unique individual, and I can only wish you nothing but the best in Spain. **Andres**, your "crazy" energy and boundless determination are your strengths, and I have no doubt you're on the right path. I eagerly look forward to our future trips together.

While I could write an entire book about the adventures with my friends in Haarlem, including **Rebeca**, **Cagri**, **Giselle**,**Michael**, **Flo**, **Jose**, **Luis**, **Prisila**, **Ruben**, **Mark**, **Laura**, and many more, I must say that words cannot fully capture my gratitude for how you all made me feel at home in this land so far away from home.

I would also like to mention the other special people I met along the way who are now close to my heart and whom I proudly call friends. **Kishore** and **Ben**, you made my stay in Alkmaar special. The three of us lived under the same roof, and I thoroughly cherish our rotational cooking and the good times we had. To the friends I made at ECN during my internship—**Sandeep**, **Ebra**, **Anne**, **Marion**, **Olaf**, **Tessa**, **Hande**, **Cansu**, **Joep**, and many more—I truly enjoyed our lunch break talks and nights out in Alkmaar. To my friends at TU Delft—**Ibra**, **Giovanni**, and **Alice**—thank you for your friendship and support.

Last but certainly not least, I want to thank my family, who sacrificed so much for me. Words don't suffice to describe how lucky I am to have you and to be able to call you my family. To my brother, sister, and brother-in-law, thank you for your support, even from Australia. To my mom and dad, I love you so much that even these words themselves sound unspeakably lame.

Mike Tang Soo Kiong Ah Sen
NS train, August 2024

CURRICULUM VITÆ

Mike Tang Soo Kiong Ah Sen was born on November 12, 1992, in Réduit, Mauritius. He began his academic journey in 2011, enrolling in a Bachelor of Science (BSc) in Mechanical Engineering at Brunel University, London. During his undergraduate studies, Mike developed a strong foundation in engineering principles, which laid the groundwork for his future endeavors in sustainable energy.

After completing his bachelor's degree in 2014, Mike pursued a Master of Science (MSc) in Sustainable Energy Technology at Delft University of Technology (TU Delft), The Netherlands. His master's thesis, titled "Si-based and Metal Oxide Passivating Contacts for Crystalline Silicon (c-Si) Solar Cells," involved an internship at Energieonderzoek Centrum Nederland (ECN) in Petten. Here, he focused on innovative passivating contact technologies, which significantly contributed to the advancement of solar cell efficiency.

In 2017, Mike embarked on a PhD at TU Delft, working in collaboration with TNO. His doctoral research centered on the development of novel passivating contact structures, utilizing highly transparent metal oxides and ultra-thin polycrystalline silicon (poly-Si) layers. These efforts were aimed at improving the conversion efficiency of c-Si solar cells. His work also involved the commissioning of a high-throughput pulsed laser deposition (PLD) tool, which enabled the fabrication of high-quality nanoscale layer stacks on an industrial scale.

Throughout his PhD, Mike not only contributed to significant research advancements but also played a key role in mentoring MSc students and managing laboratory operations. His work led to multiple publications in prestigious journals and presentations at international conferences.

Mike is currently working at Leyden Jar Technologies as a material scientist, where he continues to apply his expertise in silicon manufacturing. His current role focuses on the development of silicon-based anodes for lithium-ion batteries, aligning with the company's mission to drive innovation in sustainable energy technologies.

LIST OF PUBLICATIONS

Peer review publications related to this thesis:

- **M. T. S. K. Ah Sen**, G. Janssen, A. Mewe, P. Bronsveld, J. Melskens, F. Hashemi, P. Procel, and A. Weeber, "Influence of Passivating Interlayers on the Carrier Selectivity of MoO_x Contacts for c-Si Solar Cells", Submitted to *EPJ Photovoltaics* April 2024.

- **M. T. S. K. Ah Sen**, A. Mewe, J. Melskens, J. Bolding, M. van de Poll, and A. Weeber, "Soft deposition of TCOs by pulsed laser for high-quality ultra-thin poly-Si passivating contacts," *Journal of Applied Physics*, vol. 134, no. 15, 2023, doi: 10.1063/5.0112345.

- **M. T. S. K. Ah Sen**, P. Bronsveld, and A. Weeber, "Thermally stable MoOx hole selective contact with Al2O3 interlayer for industrial size silicon solar cells," *Solar Energy Materials and Solar Cells*, vol. 230, pp. 111139, 2021, doi: 10.1016/j.solmat.2021.111139.

Conference contributions related to this thesis:

- **M. T. S. K. Ah Sen**, A. Mewe, J. Melskens, J. Bolding, M. van de Poll, F. Hashemi, and A. Weeber, "Soft deposition of TCO by PLD on ultra-thin poly-Si passivating contacts," in: *8th World Conference on Photovoltaic Energy Conversion*, Milan, Italy, Oct. 2022, oral presentation.

- **M. T. S. K. Ah Sen**, A. Mewe, J. Melskens, F. Hashemi, and A. Weeber, "Hydrogenated SiO_y interlayer formed by etching ALD Al_2O_3 for MoO_x hole-selective contact", in: *8th World Conference on Photovoltaic Energy Conversion*, Milan, Italy (October 2022), poster presentation.

- **M. T. S. K. Ah Sen**, P. Bronsveld, and A. Weeber, "Effects of Post Deposition Anneal on a Tunnelling AlO_y Interlayer for Thermally Stable MoO_x Hole Selective Contacts," in: *SiliconPV Conference(virtual)*, Mar. 2021, visual presentation.

- **M. T. S. K. Ah Sen**, P. Bronsveld, G. Coletti, and A. Weeber "Thermally Stable MoO_x Contact with an AlO_x Interlayer for Industrial Size c-Si Solar Cells," in: *China SoG Silicon and PV Power Conference*, Shanghai, China, Nov. 2020, oral presentation.

- **M. T. S. K. Ah Sen**, P. Bronsveld, G. Janssen, and A. Weeber "Effects of interlayer on the carrier selectivity of passivating contacts," in: *37th European*

Photovoltaic Solar Energy Conference and Exhibition, September 2020, oral presentation.

- G. Janssen, **M. T. S. K. Ah Sen**, and P. Bronsveld,, "A simplified model to simulate passivating & selective hole-collecting contacts," in: *36th European Photovoltaic Solar Energy Conference and Exhibition*, September 2019, oral presentation.

- **M. T. S. K. Ah Sen**, P. Bronsveld, G. Janssen, P. Spinelli, and A. Weeber "Ultra-thin SiO_x and AlO_x passivating layers for MoO_x based selective hole contacts," in: 35th *European Photovoltaic Solar Energy Conference and Exhibition*, Brussels, Belgium, September 2019, visual presentation.

- P. Spinelli, **M. T. S.K. Ah Sen**, E.G. Hoek, B.W.J. Kikkert, G. Yang, O. Isabella, A.W. Weeber, and P.C.P. Bronsveld, "Moly-poly solar cell: Industrial application of metal-oxide passivating contacts with a starting efficiency of 18.1%," in: *SiliconPV Conference*, Lausanne, Switzerland, March 2018, oral presentation.

- **M. T. S. K. Ah Sen**, P. Bronsveld, G. Janssen, P. Spinelli, and A. Weeber "Electron beam deposited molybdenum oxide thin films for c-Si heterojunction solar cells," in: *SiliconPV Conference*, Lausanne, Switzerland, March 2018, visual presentation.